Planetary Giant Impacts: Simulating Moon-Forming Collisions

SERGIO RUIZ-BONILLA

Planetary Giant Impacts

Simulating Moon-Forming Collisions

Sergio Ruiz-Bonilla

A thesis presented for the degree of
Doctor of Philosophy

Institute for Computational Cosmology
Department of Physics
Durham University
United Kingdom

August 2022

Planetary Giant Impacts

Simulating Moon-Forming Collisions

Sergio Ruiz-Bonilla

Abstract:

Giant impacts between proto-planets were a common event in our solar system 4.5 billion years ago. However, understanding their details and consequences is still an open problem. In this thesis I use smoothed particle hydrodynamics to study how pre-impact spin of the proto-planets could affect the hypothesised giant impact that formed the Earth–Moon system, as well as developing tools to improve the numerical methods applied to these studies. To this end I developed an open-source python library to handle automatically the creation of the initial conditions necessary for these simulations.

The first chapter is an introduction to the topics of giant impacts, the Moon-forming problem, and a brief overview of smoothed particle hydrodynamics.

In the second chapter a suite of simulations of giant impacts between the early proto-Earth and the impactor Theia reveals the importance of pre-impact spin in Theia, which yields different types of impacts for different spinning rates. For some simulations we discovered the immediate creation of a proto-Moon after impact. This proto-Moon has similar mass and iron content to the present-day Moon, as well as a stable orbit around the Earth.

In the third chapter I focus on the smoothed particle hydrodynamics (SPH) method. This method is built on the idea of how to reconstruct a density field from a discrete set of particles. By definition, this sets the density as a smooth quantity over the simulation box. In planetary giant impact simulations, density discontinuities are a desirable feature. They are present for instance in the core–mantle boundary of the planets, due to the different equations of state for each material, to ensure pressure continuity. I developed a method to solve this issue, which also shows improvements with respect to traditional SPH in standard tests.

In the fourth chapter I use giant impacts and pre-impact spin of the proto-Earth to explore an explanation for the primordial misalignment problem of the Moon's orbit evolution. Long-term evolution models for the orbit of the Moon suggest a primordial angle between the Earth's spin and the normal of the lunar orbital plane. I show how this problem could be solved relying solely on the Moon-forming giant impact itself.

Contents

List of Figures

List of Tables

Declaration

The work described in this thesis was undertaken between October 2018 and March 2022 while the author was a research student under the supervision of Dr Vincent Eke and Prof Richard Massey in the Department of Physics at Durham University. No part of this thesis has been submitted elsewhere for any other degree or qualification.

Chapters 2 and 3 have been published in the following papers:

- *The effect of pre-impact spin on the Moon-forming collision*
  Sergio Ruiz-Bonilla, Vincent Eke, Jacob Kegerreis, Richard Massey, Luís Teodoro.
  Mon. Not. R. Astron. Soc. 500:3, 2021. doi: 10.1093/mnras/staa3385
- *Dealing with density discontinuities in planetary SPH simulations*
  Sergio Ruiz-Bonilla, Josh Borrow, Vincent Eke, Jacob Kegerreis, Richard Massey, Tom Sandnes, Luís Teodoro.
  Mon. Not. R. Astron. Soc. 512:3, 2022. doi: 10.1093/mnras/stac857

All figures in this thesis were produced by the author, or have been properly attributed in the figure caption. My role in these projects was both developing code and testing the different ideas with help and guidance from my supervisors.

Acknowledgements

I am extremely thankful to Vince Eke and Richard Massey for guiding me throughout this adventure. I would like to emphasize the importance of Vince's full availability and priority towards me to discuss, help, and give advice whenever needed.

Huge thanks as well to my unofficial supervisor, Jacob Kegerreis. His advice on coding, writing, and other technical aspects made a huge difference in the quality of not only my code and scientific papers, but also critical thinking and understanding of the subject.

Thanks to my colleagues Josh Borrow, Tom Sandnes, and Luís Teodoro for their ideas and improvements on my work. Thanks to the COSMA and SWIFT teams for helping out whenever I found myself surrounded by bugs.

And finally, thanks to my family for their unconditional love and support. The only kind that keeps you away from mental health issues during a PhD with a 2 year lockdown.

This thesis was supported by a PhD Studentship from the Durham Centre for Doctoral Training in Data Intensive Science, funded by the UK Science and Technology Facilities Council (STFC, ST/P006744/1) and Durham University.

If we knew what it is we were doing, it would not be called research. Would it?

—*Albert Einstein*

Dedicado a mi abuela

Esto es lo que puede llegar a pasar
cuando a un niño le enseñas a
sumar.

Chapter 1

Introduction

The birth of a planet is a long and complex process involving many steps. But if there is one spectacular moment in particular that would be the giant impact phase between proto-planets. In this phase, Mars–sized objects collided dozens of times in our solar system, determining many characteristics of the planets we see today.

Despite being crucial for explaining many features of our solar system, the specific details of giant impacts are still poorly understood and debated. In this thesis I aim to improve a bit of our understanding in this topic by looking at pre-impact spin of proto-planets, the methods generally used to study these events, and in particular, the giant impact hypothesis for the formation of the Moon, which I will use as sandbox in this thesis. However, before getting into the details of a particular giant impact, a planetary system must go through many steps before smashing planets into each other.

Planetary systems like our solar system begin their history when a giant cloud of gas and dust is perturbed. This cloud then starts collapsing, and a circumstellar disk forms almost immediately after, surrounding the young star (Williams & Cieza, 2011). Circumstellar disks are highly unstable at early times and accrete in bursts onto the central protostar. By the time the young star becomes optically visible, the mass of the now protoplanetary disk averages 1% that of the central star. This protoplanetary disk becomes stable and rotates with a Keplerian velocity profile. It is within this protoplanetary disk, with a very young star in its centre, where planets are born.

There are several theories explaining the formation of planetesimals. The classical "planetesimal hypothesis" states that planets form in the protoplanetary disk via accretion of small solid bodies called planetesimals (Safronov & Zvjagina, 1969; Hayashi et al., 1977). Pebble accretion suggests that pebbles drifting through the protoplanetary disk are accreted rapidly by the growing protoplanets (Ormel & Klahr, 2010; Lambrechts & Johansen, 2012). Nevertheless, this is one of the main differences with stellar formation, which starts from collapsing material. When the

collapsing of material into the young star ceases, the disk is able to cool down and various compounds condense into microscopic grains, adding to the preexisting ones from the interstellar medium.

The growth of planetesimals is from now on dominated by collisions. The mechanical and chemical processes related to grain agglomeration are still debated, but chondrules (small glassy inclusions of $\sim$ mm size) do provide some clues, since they appear to be heated and cooled rapidly before being accreted into larger bodies (Grossman et al., 1988). Grains and dust motion are strongly coupled (Adachi et al., 1976), and the vertical component of the star's gravity causes dust to sediment in the midplane of the disk. This sedimentation occurs for timescales of thousands of years for centimetre-sized grains, when considering collisional growth of grains (Nakagawa et al., 1981).

At this point gas is still abundant in the disk, which is partially supported by a pressure gradient, hence gas circles the star less rapidly (0.5% slower) than grains that orbit at a Keplerian rate (Adachi et al., 1976). Therefore, grains moving at Keplerian speed encountered a headwind that removes angular momentum and causes them to spiral inwards (Weidenschilling, 1977). The rate at which metre-sized bodies drift inwards is $\sim 10^6$ km/year (Lissauer, 1993), hence the transition to kilometre-size bodies must have been quick (Safronov, 1960; Goldreich & Ward, 1973). This growth phase to kilometre-size bodies is dominated by coagulation of grain aggregates that collided due to differential settling, turbulence, drag-induced orbital decay, and aided by concentration of larger bodies towards the central plane of the disk (Weidenschilling & Cuzzi, 1993).

Growth continues via two-body collisions. The distributions of planetesimal masses and velocities evolve thanks to collisions and gravitational scattering (Greenberg et al., 1978). Collisions can be modelled analytically using hard spheres and inelastic collisions (Hornung et al., 1985), and gravitational scattering can be modelled in the same way as in stellar dynamics (Binney & Tremaine, 1987). Using this approach, one finds that larger planetesimals grow faster than smaller ones, resulting in the runaway growth of the largest planetesimal (Greenberg et al., 1978; Wetherill & Stewart, 1989). The main inconvenience of this analytical/statistical approach is the assumption of a uniform spatial distribution, therefore the later stages of this phase are difficult to investigate. More recently this phase of planet formation has been modelled numerically via N-body simulation codes (Kokubo et al., 2000; Ida & Makino, 1993; Kokubo & Ida, 1998). Results from numerical simulations agree with analytical ones.

The larger a planetesimal becomes, the larger its growth rate becomes by gravitational focusing (which is the probability of two bodies colliding) and dynamical

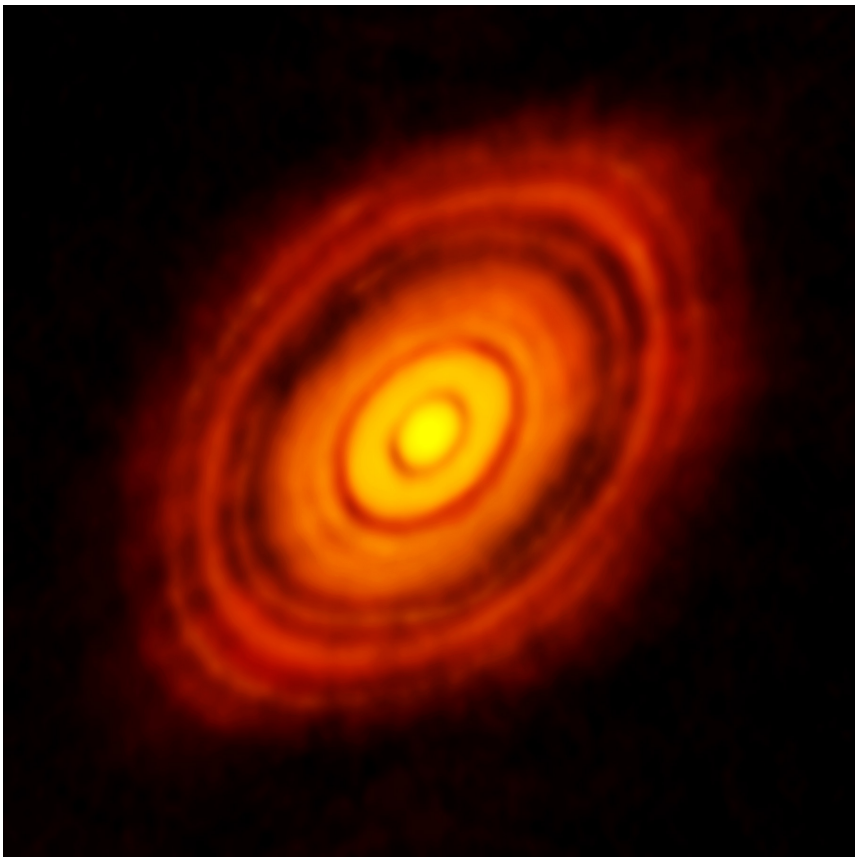

Figure 1.1: Protoplanetary disk surrounding the young star HL Tauri, at 450 light years away from Earth. Luminosity and effective temperature suggest its age is less than 100,000 years (Boss et al., 1989). Substructures within the disk show the possible positions of planets forming in the dark patches within the system. This star appears to be surrounded by forming planets despite its young age, which has prompted new proposals for faster mechanisms of planet formation (Stephens et al., 2014). Credit: ALMA (ESO/NAOJ/NRAO).

friction from smaller planetesimals. Then, at different radii, the largest planetesimal becomes isolated from the continuous mass distribution. These planetesimals, which have undergone a runaway growth and are now isolated, are called proto-planets, and this event has been observed for the first time very recently as shown in Figure 1.1 (ALMA Partnership et al., 2015). At the end of this phase, the mass distribution is divided into a small number of large proto-planets and a large number of small planetesimals (Kokubo et al., 2000). Once proto-planets are formed, the age of giant impacts begins.

The frequency of giant impacts, as well as their resulting angular momentum and other statistics can be studied using N-body simulations (Agnor et al., 1999; Chambers, 2001; Kokubo & Genda, 2010; Miguel & Brunini, 2010). We expect dozens of

giant impacts events took place in our solar system, half of them being accretion events and the other half hit-and-runs on average (Kokubo & Genda, 2010), where the typical impact velocity was between 1 and 2, in units of the mutual escape velocity of the bodies.

The number of resulting planets expected from simulations in the inner region of the solar system is between 2 and 5, with the more massive ones being similar to Earth's mass (Kokubo & Genda, 2010). The spin rates of the resulting planets depend mainly on the last one or two giant impacts, and its value is on average 30% smaller than the critical angular velocity of the planet for realistic (where hit-and-run impact are considered) models (Kokubo & Genda, 2010), or as high as the critical angular velocity for perfect accretion models (Agnor et al., 1999; Kokubo & Ida, 2007). Obliquity ranges from 0° to 180° following an isotropic distribution (Miguel & Brunini, 2010). This is a natural consequence of giant impacts being 3-dimensional and adding equally random contributions to each spin angular momentum component (Kokubo & Ida, 2007).

But most importantly, giant impacts played a crucial role in planet formation, since they shaped how planets look today (Chambers, 2001). Many examples can be found in our solar system: the tilted axis of Uranus (Slattery et al., 1992; Kegerreis et al., 2018; Reinhardt et al., 2020), the formation of Mars' moons (Craddock, 2011; Citron et al., 2015), Mars' hemisphere dichotomy (Andrews-Hanna et al., 2008), or Mercury's thin mantle (Benz et al., 1988) are some of the features of our solar system that have been explained through giant impacts.

The holy grail of giant impacts, the main focus of this thesis, is the formation of the Moon. There's strong evidence that the Earth and Moon share a common origin through a giant impact (Cameron & Ward, 1976; Hartmann et al., 1975). However the details are still unclear and many different impact configurations have been proposed (Benz et al., 1986; Melosh, 1989; Cameron, 1997; Ćuk & Stewart, 2012; Lock et al., 2018; Canup & Asphaug, 2001). The fact that the Moon is the closest celestial object to Earth makes this one a particularly interesting problem, as well as challenging, due to all the observational constraints available.

1.1 The Formation of the Moon

The Earth–Moon system is quite exceptional and many reviews about its formation are available to expand on this section (Asphaug, 2014; Barr, 2016; Lock et al., 2020; Canup et al., 2021). The Moon's mass is large compared with its host as well as its orbital angular momentum, implying a rapidly spinning Earth when the Moon

was formed. In addition, its core is small ($\sim 1\%$ of its mass, Wieczorek (2006)) and the early Moon's surface was covered by a deep magma ocean (Warren, 1985). A successful theory for the formation of the Moon should be able to explain all these features and more that we will mention later in §1.1.1.

Original theories for the formation of the Moon include capture, fission, co–accretion, and collisional ejection (Wood, 1986; Hartmann et al., 1975; Cameron & Ward, 1976). However, once the *Apollo* missions allowed the direct study of samples from the Moon, the similar oxygen isotopic compositions (^{17}O and ^{18}O) of the Earth and Moon was discovered, and the giant impact hypothesis seemed to be a good candidate to explain all features mentioned above as well as the isotopic similarity between Earth and Moon (Wood, 1986). A giant impact could produce an iron–poor debris disk surrounding the Earth with the right angular momentum and physical properties (Benz et al., 1986, 1987; Canup & Asphaug, 2001). This so–called "canonical impact" predicts a Moon made primarily from impactor material, but the isotopic similarities between the Earth and Moon (Wiechert et al., 2001; Zhang et al., 2012) could be explained only if the Moon formed mainly from the Earth's material, or if the impactor's original isotopic composition was similar to the Earth's. This problem has been characterized as the "isotopic crisis" (Melosh, 2014). This hypothesized impactor that collided with the Earth to later form the Moon is usually called Theia.

1.1.1 The importance of the Moon's composition

The bulk silicate Earth (BSE) refers to the chemical composition of the Earth's primitive mantle. This is usually computed by imposing cosmochemical constraints on compositional trends exhibited by upper-mantle rocks (Lyubetskaya & Korenaga, 2007). Measurements of the Moon's composition and its comparison with the BSE provides constraints on the thermodynamic history of the Moon, and therefore constraints for the giant impact hypothesis.

Lunar glasses and other minerals can be used to estimate the composition of the lunar mantle and bulk silicate Moon (BSM), that is the Moon's silicate composition after accretion and before its differentiation into mantle and crust. Data show that the BSM was depleted compared with the BSE in volatile elements by different amounts (McCubbin et al., 2015; Hauri et al., 2015; Chen et al., 2015). H_2O is depleted by a factor of 5, although some portions of the Moon had H_2O abundances comparable with the BSE (Greenwood et al., 2011; Hauri et al., 2011). Volatile alkali elements K, Na, Rb and Cs are depleted by a factor of 5–6; S is depleted by a factor of 2–3; and C and other highly volatile siderophile elements are depleted by factors of 5–200 in the BSM relative to the BSE.

The mechanism responsible for the Moon's volatile depletion is still debated (Day & Moynier, 2014). An initially volatile-poor composition for the protolunar material due to a volatile-depleted impactor could account for a factor of 5–6 depletion (Newsom & Taylor, 1989), but it would not explain higher values like the one for Zn and other elements. Another idea is depletion associated with escape from the hot protolunar disk material (Genda & Abe, 2003; Desch & Taylor, 2011). A disk made of melt and vapour material would preferentially incorporate the melt into the Moon (Canup et al., 2015; Pahlevan et al., 2016; Lock et al., 2018), and/or later degassing and loss from the lunar magma ocean (Elkins-Tanton & Grove, 2011; Barnes et al., 2016; Dhaliwal et al., 2018). If so, the amount of volatile loss in a planet could be associated with basic parameters like the mass of the planet, surface gravity and escape velocity. Variations in the amount of depletion may help distinguish between different volatile depletion hypotheses.

Planetary processes like the ones mentioned above can alter the absolute concentration of an element but they cannot affect their relative isotopic concentrations. Observed isotopic variations are then ideal to trace the origin of the material of the Moon. These variations with respect to the values at Earth are called isotopic anomalies and they provide the strongest constraints on the fraction of Moon that originated from Earth.

We will use oxygen as an example of how isotopic anomalies are reported. Oxygen has three stable isotopes, ^{16}O, ^{17}O, and ^{18}O, so two isotope ratios can be defined: ^{17}O/^{16}O and ^{18}O/^{16}O. Using a reference value, e.g. SMOW (Standard Mean Ocean Water for oxygen), we can express the ratios defined above as

$$\delta^{17,18}\mathrm{O}(‰) \equiv \left[\left(^{17,18}\mathrm{O}/^{16}\mathrm{O}\right)_{\mathrm{sample}} / \left(^{17,18}\mathrm{O}/^{16}\mathrm{O}\right)_{\mathrm{SMOW}} - 1\right] \times 1000. \qquad (1.1.1)$$

Since the difference in mass between ^{17}O and ^{16}O is half of the difference between ^{18}O and ^{16}O, most terrestrial samples fall on a line with slope 1/2 that passes though the origin in a δ^{17}O *v* δ^{18}O diagram, whose origin corresponds to values identical to the SMOW. Isotopic anomalies are defined as the vertical offset from this line, expressed in parts per thousand or parts per million as Δ^{17}O values. When discussing isotopic anomalies, context from observed variations on meteorites or other planets must be provided. If all meteorites have the same isotopic composition as Earth, no isotopic differences between Earth and the Moon are expected to be found, and no constraint on the formation of the Moon is obtained.

A value of $\Delta^{17}\mathrm{O} = +0.321 \pm 0.013$ ‰ was obtained for Mars (Franchi et al., 1999), suggesting isotopic variation amongst planetary bodies in our solar system. Therefore, if the Moon-forming impactor had different isotopic composition than the proto-Earth, one would expect to see it reflected in the Earth–Moon differences today.

However, the first measurement for the oxygen isotopic anomaly of the Moon was done by Clayton & Mayeda (1975), with a value of $\Delta^{17}O = -0.075 \pm 0.049$ ‰, making them statistically indistinguishable. Ever since that first measurement, multiple and more precise studies have been performed motivated by the idea to determine if a difference exists. Many authors found $\Delta^{17}O$ values within a few parts per million (ppm) with error bars large enough to make the measurement indistinguishable from Earth's (Wiechert et al., 2001; Spicuzza et al., 2007; Hallis et al., 2010; Young et al., 2016). Others found very small significant differences of a few ppm (Herwartz et al., 2014; Greenwood et al., 2018), and Cano et al. (2020) proposed that oxygen isotopic composition varies with lithology, and found differences on VLT (very low-Ti) green glasses of 20 ppm or more, which are representative of the deeper interior of the Moon. In contrast, common meteorites have $\Delta^{17}O$ values within -4.7 ‰(-4700 ppm) and 2.6 ‰(-2600 ppm) (Dauphas & Schauble, 2016).

The similarity in oxygen isotopes could be a consequence of a process of equilibration between the terrestrial magma ocean and protolunar disk via the vapour phase (Pahlevan & Stevenson, 2007). This process may affect primarily elements in the vapour phase and be less effective for highly refractory elements like titanium. However, measurements of the Ti isotopic anomaly, once the effects of exposure to cosmic rays were deducted, show that there was no ^{50}Ti anomaly present in lunar rocks (Zhang et al., 2012). Apart from oxygen, other non–volatile elements like Ca and Cr have been measured in lunar rocks showing that they are indistinguishable from Earth (Dauphas et al., 2015; Schiller et al., 2018; Mougel et al., 2018).

1.1.2 Giant Impact Models

Many authors have developed models to attempt to identify a collisional scenario that can explain all properties of the Earth–Moon system. These models typically use the smoothed particle hydrodynamics method that we will discuss in Section 1.2. First we will briefly summarize the constraints available, then we will proceed to explain the most popular ideas.

Obtaining the right total angular momentum is the first constraint ($L_{EM} = 3.5 \times 10^{41}$ g cm^2 s^{-1}). A new Moon orbiting at the Roche radius implies a terrestrial day of 5 hours if the primordial system angular momentum is equal to L_{EM}. There are dynamical mechanisms that could reduce the angular momentum of the system by a factor of 2–3, hence the primordial angular momentum could have been much larger than the value at present day (Ćuk & Stewart, 2012; Wisdom & Tian, 2015; Rufu & Canup, 2020).

The mass of the protolunar disk must be sufficiently large to later accrete a lunar–mass Moon. An initial disk with mass between 1.3 and 3 lunar masses is sufficient for that purpose (Salmon & Canup, 2012; Kokubo et al., 2000). Moreover, the disk should be iron–poor to account for the small lunar core.

As mentioned in Subsection 1.1.1, the Earth and Moon share almost identical isotopic compositions across many elements, while meteorites from Mars differ substantially. The compositional difference in a protolunar disk can be quantified as

$$\delta f_T \equiv \frac{F_{\mathrm{D,pE}}}{F_{\mathrm{P,pE}}} - 1, \tag{1.1.2}$$

where $F_{\mathrm{D,pE}}$ and $F_{\mathrm{P,pE}}$ are the mass fractions of the silicate portions of the disk and the post–impact Earth derived from the proto-Earth's mantle. A value of $|\delta f_T| < 5\%$ is required for an impactor that was Mars–like in composition (Canup, 2012). Note that it is unknown what was Theia's composition. However, the less similar to the proto-Earth, the more restricted and close to zero $|\delta f_T|$ needs to be, and vice-versa.

Now we will introduce the main hypotheses describing the giant impact that formed the Earth–Moon system.

1.1.2.1 Canonical Impact

A Mars–sized impactor that collides with the proto-Earth at a low velocity (comparable with the common escape velocity) can produce a sufficiently massive protolunar disk with poor iron content and the appropriate total angular momentum (Benz et al., 1986; Canup & Asphaug, 2001). The masses of the proto-planets are common in models of planet accretion (Kokubo & Genda, 2010), and the angle of impact is between the 40–50° range, where 0° is a head-on collision. The main problem with this scenario is the isotopic crisis. Most of the material of the protolunar disk comes from the impactor instead of the proto-Earth ($\delta f_T \sim -80\%$) contradicting observational data (unless Theia was very Earth-like).

As we mentioned before, the process of equilibration could solve this issue (Pahlevan & Stevenson, 2007; Nakajima & Stevenson, 2015), as well as having an impactor whose isotopic composition is very similar to that of the Earth. However this later solution seems unlikely (Pahlevan & Stevenson, 2007; Dauphas, 2017; Mastrobuono-Battisti & Perets, 2017; Schiller et al., 2018). Hosono et al. (2019) found a canonical impact could form a proto-Earth-rich protolunar disk if the Earth had a surface magma ocean at the time the impactor collided and a modified version of smoothed particle hydrodynamics was used. Wissing & Hobbs (2020) performed a similar study and found no significant differences between having or not a proto-Earth

with a surface magma ocean. Similarly, Stewart et al. (private communication) performed a study with improved equations of state for a primitive magma ocean on the proto-Earth and found contrary results to Hosono et al. (2019).

1.1.2.2 Hit–and–run Impact

Low angle (30–40°), high–speed ($v \sim 1.3 v_{\rm esc}$) impacts can create disks richer in proto-Earth material than canonical impacts ($\delta f_T \sim -40\%$) (Reufer et al., 2012). In addition, high velocities favour loss of material and angular momentum from the system allowing for larger impactors and higher angular momentum before impact. Successful impacts produce disks massive enough to form a Moon from them but also a final angular momentum higher ($\sim 1.3 L_{\rm EM}$) than the present value (Reufer et al., 2012). Hence, a mechanism to remove angular momentum after the impact is needed.

1.1.2.3 Fast–spinning Earth Impact

The isotopic similarities between Earth and Moon have prompted the study of much higher angular momentum impacts, which could more naturally explain the data. Several authors (Canup, 2008; Ćuk & Stewart, 2012; Lock et al., 2018) proposed a fast–spinning proto-Earth, whose angular momentum is higher than $L_{\rm EM}$ (≥ 2) and parallel to the orbital angular momentum of the impactor (prograde and retrograde motions). As a result they found a protolunar disk made mainly from the proto-Earth ($|\delta f_T| \sim 1\%$), consistent with observational data. The protolunar disks produced from these simulations are pure vapour, as opposed to canonical–like disk that are dominated by melt. Similar to the previous case (but with greater angular momentum that needs to be removed), these models require a mechanism to reduce the total angular momentum of the Earth–Moon system to the present-day value.

1.1.2.4 Half–Earth Impact

Forming a protolunar disk from similar composition of the main planet is achieved if the disk is made of proto-Earth material given that the impactor's mass is small compared with the proto-Earth. Another alternative would be a completely symmetric collision between two proto-planets, each having half the mass of the Earth. In this situation the post–impact Earth would be made of 50% target and 50% impactor, as well as the protolunar disk.

Canup (2012) showed that slightly asymmetric collisions, where the mass of the impactor is $> 40\%$ can produce a protolunar disk with $|\delta f_T| \sim 1$–10%. This scenario

produces high mass disks (up to 5 lunar masses), which could help forming the Moon if accretion is inefficient (Lock et al., 2018). Similar to the previous cases, the total angular momentum of the system after impact exceeds the present day value, and mechanisms to remove the excess are required.

1.1.2.5 Synestia

Lock & Stewart (2017) proposed a high–energy, high–angular momentum impact could produce a synestia. Synestias are characterized by having an angular velocity at the equator equal to the Keplerian orbital velocity. At this point the planet has reached its corotation limit, and a single corotating body is not possible. Hence, a synestia is a hot planetary body structure, with a corotating inner region connected to a disk-like outer region.

Satellite formation from a synestia can produce the main features of the Moon and equilibration within a synestia may be achieved by turbulent mixing in high–entropy regions (Lock et al., 2018). Cooling drives mixing of the structure, and condensation generates moonlets that orbit within the synestia, surrounded by high–pressure bulk silicate Earth vapour. Moonlets equilibrate with bulk silicate Earth vapour at the temperature of silicate vapourization and the pressure of the structure, establishing the lunar isotopic composition and pattern of moderately volatile elements. Eventually, the cooling synestia recedes within the lunar orbit, terminating the main stage of lunar accretion.

High angular momentum impacts ($> 1.7\ L_{\mathrm{EM}}$) are likely to form synestias. Most Earth-like planets may have experienced a synestia–like structure after an impact during their late accretion process (Lock & Stewart, 2017). Removal of angular momentum from the system is also a requirement for this model of the formation of the Moon.

1.1.2.6 Multiple impacts

Giant impacts were common, and a planet like Earth is expected to experience multiple impacts in its late accretion stage (Kokubo & Genda, 2010; Agnor et al., 1999). The idea of the Earth experiencing multiple impacts that lead to the formation of the Moon is not new (Ringwood, 1989), however it has been explored recently with modern tools (Rufu et al., 2017). The Moon could have formed from a sequence of small impactors ($< 1\%\ M_{\oplus}$), where each impact generates a small satellite that migrates outwards due to tidal interactions. Subsequent impacts produce similar moons, which end up merging with the previous one. Impacts can occur with random

orientations, making it difficult to reach the desired high angular momentum of the Earth–Moon system today. However, multiple small impacts could explain an unmixed Earth mantle reservoir (Touboul et al., 2012; Mukhopadhyay, 2012). Rufu et al. (2017) concluded that $N \sim 20$ small impacts can produce a lunar–sized satellite and that the standard deviation of the Δ^{17}O difference between the growing moon and target decreases with $\sqrt{N}$.

1.1.3 Post–Impact Evolution

Solving the isotopic crisis has prompted new models that rely on high angular momentum giant impacts as seen in Subsection 1.1.2. These models obtain better values consistent with the isotopic similarities between Earth and Moon, however they require mechanisms to remove the excess of angular momentum from the system by a factor of 2–3 to match the present-day value.

The main driver in the Earth–Moon system dynamical evolution are tides raised on the Earth by the Moon. Tidal bulges raised when the Earth's spin is faster than the Moon's orbital velocity, cause a torque between the Moon and the tides, which transfers angular momentum from the Earth's spin to the orbit of the Moon. This process does not change the total angular momentum of the system, but others might. Late accretion onto the Earth after the formation of the Moon may have altered, either increasing or decreasing, the total angular momentum of the system. This change is only of the order of a few percent via direct impacts (Bottke et al., 2010), and a few tens of percent via collisionless encounters (Pahlevan & Morbidelli, 2015). Still not sufficient to explain a decrease by a factor of 2.

When the Moon's semimajor axis was around 4.6 $R_\oplus$, it would have encountered a resonance when the lunar perigee precession period was equal to one year. This is called the evection resonance (Kaula & Yoder, 1976). If the Moon was captured into evection, the outwards tidal migration is accompanied by an increase in eccentricity. When high eccentricities are reached, tidal dissipation in the Moon becomes relevant, stopping the eccentricity growth and locking the Moon at a constant distance from Earth. This equilibrium will be broken since tidal forces are still transferring angular momentum from the spin of the Earth to the Moon's orbit. During this exit from the evection resonance, solar perturbations on the Moon remove angular momentum from the Moon's orbit into the Earth's heliocentric orbit.

Touma & Wisdom (1998) considered an initial Earth–Moon system with angular momentum similar to the present-day value, and found that exit from evection resonance removes $\sim$ 10% of the angular momentum (Touma & Wisdom, 1998).

Later, Ćuk & Stewart (2012) considered an initial high angular momentum Earth–Moon system ($\sim$ 2–3 $L_{\rm EM}$), and found that capture in the resonance occurred for longer times, allowing a decrease in angular momentum by a factor of 2 or more. Other studies suggest that removing such large quantities of angular momentum required low–eccentricity evolution and a dissipative Moon (Wisdom & Tian, 2015; Tian et al., 2017). A wider range of final angular momenta could be possible, depending when escape from evection happens (Rufu & Canup, 2020).

1.2 SPH Simulations

As briefly mentioned in Subsection 1.1.2, the most common tool to study giant impacts is smoothed particle hydrodynamics (SPH). In this section we will discuss the fundamental idea behind this method and how to apply it to our particular field of interest, giant impacts.

SPH was originally formulated by Lucy (1977) and Gingold & Monaghan (1977) to simulate asymmetric phenomena in astrophysics. The original authors found that SPH gave sensible answers in difficult situations, and the method could incorporate new physics in a fairly easy way. Today SPH is still widely used in astrophysics, as well as geophysics, engineering and in the film and computer games industry. Traditional reviews of SPH (Monaghan, 1992; Price, 2005) introduce the method with a formal discussion of kernel interpolation theory, however in the following section we will briefly review SPH derived from the discrete Lagrangian, as done by Price (2012).

1.2.1 The Basics

It all starts with the following question: how can you compute a density field from an arbitrary distribution of point mass particles?

The most straightforward answer is perhaps to construct a mesh in the simulation box you are working on, compute the total mass in each cell, and divide by its volume. This approach is used in hybrid particle mesh methods like Marker-In-Cell (Harlow & Welch, 1965) or Particle-In-Cell (Hockney & Eastwood, 1981). A fixed mesh will have many cells in empty regions and very few where all the mass is concentrated, i.e. it oversamples low density regions and undersamples high density regions given that the mass distribution in the simulation box is highly clustered. For that and other reasons, it is more convenient to remove the mesh completely and compute the density based on the local distribution of particles, for instance using a sphere

centered on the location of the desired point where we want to compute the density. We could compute the total mass inside this sphere and divide by its volume. This estimate is noisy because a particle sitting close to the edge of the sphere could slip in and out making significant changes in the density ($\delta\rho \propto 1/N_{\rm ngb}$ for equal mass particles). This leads to the idea of down-weighting contributions from particles as the relative distance increases.

Density is therefore computed using neighbouring particles and some sort of weighting function W,

$$\rho(\vec{r}) = \sum_{i=0}^{N_{\rm ngb}} m_i W(\vec{r} - \vec{r}_i, h), \tag{1.2.1}$$

where $N_{\rm ngb}$ is the number of neighbours, m_i is the mass of particle i, and h is a length-scale that determines the rate of fall-off of W. W is referred to as the smoothing kernel, and h is the smoothing length. A good candidate for the smoothing kernel function should have certain properties. It should be positive, monotonically decreasing with the relative distance and have smooth derivatives; it should be symmetric under rotations, that is dependent only on the relative distances of particles (i.e. $W(\vec{x}-\vec{y}, h) \equiv W(|\vec{x}-\vec{y}|, h)$); and it should have a flat central portion so the density is not strongly affected by small changes in the position of near neighbours (Price, 2012). Finally, note that conservation of mass, $\int \rho dV = \sum_{i=1}^{N_{\rm tot}} m_i$, will imply a normalisation factor. With all these constraints a Gaussian function seems a good candidate, however it has the computational disadvantage of having an infinite support, meaning that all particles have a contribution to the density at any point no matter how far away they are. Hence, the best solution is to use a kernel that is Gaussian-like but truncated at a finite radius. The most used options are the B-spline functions (Shoenberg & Wilson, 1946; Monaghan & Lattanzio, 1985), followed by others like the Wendland (1995) kernels (Dehnen & Aly, 2012).

Early SPH simulations used constant smoothing length, h, however it is desirable to adapt it such that it resolves equally sparse and high density regions. A natural choice is to make the cube of the smoothing length of a particle proportional to its volume, $V_i = m_i/\rho_i$, where m_i and $\rho_i \equiv \rho(\vec{r}_i)$ are the mass of the particle, and the density field evaluated at the position of particle i, $\vec{r}_i$. Overall we have to solve simultaneously for every particle the equations for the density and smoothing length,

$$\rho_i \equiv \rho(\vec{r}_i) = \sum_{j=1}^{N_{\rm ngb}} m_j W(\vec{r}_i - \vec{r}_j, h_i), \qquad h_i \equiv h(\vec{r}_i) = \eta \left(\frac{m_i}{\rho_i}\right)^{1/d}, \tag{1.2.2}$$

where d is the number of dimensions, and η is a dimensionless parameter. Note that η carries the same value for any number of dimensions whereas the number of

neighbours, $N_{\rm ngb}$, which could be used to define h_i does not. This becomes useful when comparing results from different test problems in different dimensions. The definition above is approximately equivalent to keeping the mass inside the kernel constant, since for example in three dimensions

$$M_i = \int_{V_i} \rho dV \approx \frac{4}{3}\pi R^3_{\rm kernel}\rho_i, \tag{1.2.3}$$

where $R_{\rm kernel} = \zeta h$ is the kernel radius ($\zeta = 2$ for the cubic spline kernel), so a constant M_i implies constant $h^3\rho$. On the other hand, $M_i = N_{\rm ngb}m$ assuming all particles have the same mass. Solving for $N_{\rm ngb}$ we obtain

$$N_{\rm ngb} \approx \frac{4}{3}\pi(\zeta\eta)^3 \tag{1.2.4}$$

for the $3D$ case, and similarly can be done for one and two dimensions.

We have answered our initial question with a solution that is independent of time and now we proceed to briefly describe the equations that govern the evolution of particle positions and velocities. This part of the method is completely derived from the definition of the density estimate. The Lagrangian of our system can be written as

$$L \equiv T - V = \sum_i m_i \left[\frac{1}{2}v_i^2 - u_i(\rho_i, s_i)\right], \tag{1.2.5}$$

where T and V are the total kinetic and potential energy respectively; v_i, u_i, ρ_i, and s_i are the velocity, specific internal energy, density, and specific entropy of particle i respectively. Using the least action principle we get the Euler-Lagrange equations:

$$\frac{d}{dt}\left(\frac{\partial L}{\partial v_i^k}\right) - \frac{\partial L}{\partial r_i^k} = 0, \tag{1.2.6}$$

where i goes from 1 to N, the total number of particles, and k goes from 1 to d, the number of dimensions. Assuming a constant smoothing length, these equations simplify to the standard SPH formula (Monaghan, 1992):

$$\vec{a}_i = -\sum_j m_j \left(\frac{P_i}{\rho_i^2} + \frac{P_j}{\rho_j^2}\right)\nabla_i W_{ij}, \tag{1.2.7}$$

where $W_{ij} = W(\vec{r}_i - \vec{r}_j, h_i)$, P_i is the pressure of particle i, and P_j is the pressure of neighbouring particle j. The evolution of the internal energy of every particle, u_i is governed by the equation

$$\frac{du_i}{dt} = \left.\frac{\partial u_i}{\partial \rho_i}\right|_s \frac{d\rho_i}{dt}, \tag{1.2.8}$$

assuming an adiabatic evolution (i.e. $\dfrac{ds_i}{dt} = 0$). From the first law of thermodynamics

$du = Tds - PdV$, and $V = m/\rho$, hence $dV = -m/\rho^2 d\rho$. Finally we can derive

$$\frac{du_i}{dt} = \frac{P_i}{\rho_i^2} \sum_j m_j (\vec{v}_i - \vec{v}_j) \cdot \nabla_i W_{ij}. \tag{1.2.9}$$

These previous formulae imply exact conservation of total linear momentum, total angular momentum, and total energy (Price, 2012). The above derivation assumes constant smoothing length h. A similar reasoning can be done for an adaptive smoothing length, which is what is implemented in SWIFT (Schaller et al., 2016).

SPH simulations use an artificial viscosity term (Monaghan, 1992; Cullen & Dehnen, 2010) to create shock waves, which are crucial for modelling giant impacts. This viscosity converts kinetic energy to internal energy only when $(\vec{v}_i - \vec{v}_j) \cdot (\vec{x}_i - \vec{x}_j) < 0$. A particular refinement of interest is the Balsara (1995) formulation, which is implemented in SWIFT, because it additionally turns off the artificial viscosity in pure shear flows. The artificial viscosity conserves energy and provides linear and quadratic terms in both the acceleration equation (Equation 1.2.7) and the time-evolution of the internal energy equation (Equation 1.2.9).

The hydrodynamic equations described above, together with the gravitational forces, are integrated forward in time using a kick-drift-kick algorithm (Verlet, 1967; Swope et al., 1982). "Kick" means updating the velocity from the acceleration and "drift" means updating the positions from the velocities. In its basic form, without variable time-steps, the equations are:

$$\begin{aligned} v_{i+1/2} &= v_i + a_i \frac{\Delta t}{2}, \\ x_{i+1} &= x_i + v_{i+1/2} \Delta t, \\ v_{i+1} &= v_{i+1/2} + a_{i+1} \frac{\Delta t}{2}. \end{aligned} \tag{1.2.10}$$

There are multiple criteria for the choice of an appropriate time-step. One criterion is the Courant-Friedrichs-Lewy (CFL) condition (Courant et al., 1967):

$$\Delta t_i = C \frac{h_i}{\max_j \left(c_i + c_j + \max\{0, -3\vec{r}_{ij} \cdot \vec{v}_{ij} / r_{ij}\} \right)}, \tag{1.2.11}$$

where C is the CFL constant, usually set to ~ 0.2 (Borrow et al., 2018), c_i and c_j are the sound speeds of particles i and j respectively, $\vec{r}_{ij} \equiv \vec{r}_i - \vec{r}_j$, $\vec{v}_{ij} \equiv \vec{v}_i - \vec{v}_j$, and $r_{ij} \equiv |\vec{r}_{ij}|$. In practice the sound speeds are replaced with a signal velocity that depends on the artificial viscosity parameters. The CFL condition ensures the stability of the integration scheme, which is a necessary (but not sufficient) condition for accurate results with numerical schemes. Another important time-step criterion

related to the gravitational forces between particles is adopted:

$$\Delta t_i = \left(\frac{2\eta\epsilon}{|\vec{a}_i|} \right)^{1/2}, \tag{1.2.12}$$

where η is an accuracy parameter set to 0.025 (J. Kegerreis, private communication), ϵ is the gravitational softening parameter (which will depend on the total number of particles in the simulation), and $\vec{a}_i$ is the acceleration of particle i. This criterion is not only implemented in SWIFT, but in other popular SPH codes like Gadget-2 (Springel, 2005). There is one last time-step criterion related to the change of smoothing length over time, which is relevant for giant impact simulations:

$$\Delta t_i = \left| \log(V_c^{1/d}) h_i \left(\frac{dh_i}{dt} \right)^{-1} \right|, \tag{1.2.13}$$

where V_c is a volume change parameter set to 1.4 (J. Kegerreis, private communication), and d is the number of dimensions in the problem. In practice in SWIFT, all particle time-steps are related by factors of two. For an individual particle, the actual value chosen within this hierarchy is the largest available time-step that lies below the three different time-step criteria just described (Borrow et al., 2018).

The fact that SWIFT uses a hierarchy of time-steps with individual particle time-steps allowed to change with time means that, even though a leapfrog integrator is used, the method is not time-reversible. Hence total energy is not conserved. For the runs in this thesis, total energy is typically conserved to 1%.

In this thesis in particular, we are interested in iron and granite-like material, which we will use to model the core and mantle of rocky planets. The most widely used option for giant impacts is the Tillotson (1962) analytical equation of state (EoS). In brief, it is based on a compressed or cold state, an expanded or hot state, and a transition region between those two. It is described by 10 parameters and it does not include an expression for the sound speed, c, however it can be derived from the following:

$$c^2 = \left. \frac{\partial P}{\partial \rho} \right|_S . \tag{1.2.14}$$

The Tillotson EoS does not capture phase transitions, which could be important in giant impact simulations where vapourization plays a role (Stewart et al., 2020). A more modern approach is to use the ANEOS EoS (Thompson, 1970; Melosh, 2007; Stewart et al., 2020), which is capable of covering a large range of densities and temperatures, as well as being able to capture multiple phase transitions.

While SPH is most popular, some other methods have been used to simulate impacts, such as Eulerian codes (Melosh, 1989). In SPH, particles represent a mesh which

moves with the material, but no mass flows between cells. In Eulerian codes, the mesh is fixed (or adaptive) and the material flows between the different cells (McGlaun, 1991). One benefit of SPH that is of particular relevance for giant impacts is that the provenance of material is naturally tracked by the SPH particles, whereas mesh codes need to have tracer particles added for this purpose.

1.2.2 Giant Impacts in SPH and SWIFT

The first giant impact SPH simulations were performed by Benz et al. (1986) focusing on the formation of the Moon, using roughly 2000 particles. Technology and improvements in the method has allowed a significant increase in number of particles over the last decades. As of today, it is common to see 10^5 or 10^6 particle simulations labeled as 'high resolution' (Genda et al., 2015; Gabriel et al., 2020), but SWIFT is changing this expectation (Kegerreis et al., 2019).

SWIFT (SPH With Inter-dependent Fine-grained Tasking) is a hydrodynamics and gravity code for astrophysics and cosmology in open development (swift.dur.ac.uk), designed with the idea to run fast and scale well on shared/distributed-memory architectures (Schaller et al., 2016). Physical limitations have kept the speed of individual processor cores constrained for the last decade, hence supercomputers are getting more parallel. It is crucial in this computing paradigm to share the work evenly between every part of the computer so that no processors are sitting idle and wasting time.

SWIFT can work as a replacement for the Gadget-2 code, which has been widely used for cosmological and planetary impact simulations (e.g. Springel, 2005; Ćuk & Stewart, 2012), with a >30× faster runtime on one representative cosmological problem (Borrow et al., 2018). Although its scaling is not ideal, as shown in Figure 1.2 (V. R. Eke, private communication), SWIFT has a considerably faster time-to-solution than Gadget-2 due to three strategies: an adaptative mesh used to ensure that only the relevant particles are interacted in a given time-step; the task-based parallelism used to ensure efficient load-balancing within a single node; and a domain composition strategy that splits the work that must be performed by the simulation between nodes using MPI (Borrow et al., 2018).

SWIFT has a modular structure that allows clean modifications to, for example, the hydrodynamics scheme without affecting the parallelisation or any other component. Every module can be switched in or out with configuration flags, meaning that SWIFT can run cosmological, planetary, or any other simulation. In particular, giant impact simulations are a challenge for balancing the tasks between different nodes or cores. SWIFT was initially designed for cosmological simulations, where

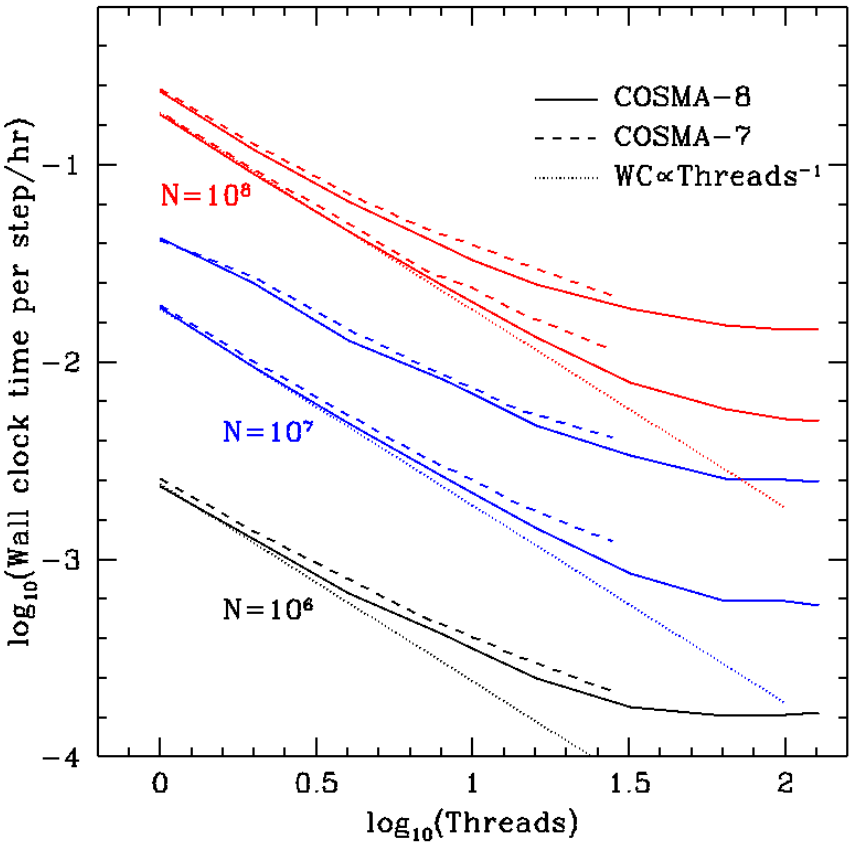

Figure 1.2: Wall clock time per step as a function of the number of threads for the SWIFT code in the COSMA 7 and 8 supercomputers (dashed and solid lines respectively) compared to ideal scaling (dotted line) (V. Eke, private communication). Different colors represent different number of particles, from bottom to top: 10^6, 10^7, $10^{7.5}$, 10^8, and $10^{8.5}$.

the average density is roughly constant across the simulation box. However for a giant impact, almost all the mass is in the planet at the centre.

When we use a large simulation box in order to follow the ejected debris, the vast majority of particles can easily occupy less than 0.01% of the volume. This makes it harder to divide up particles between computing nodes, and requires much more frequent communication. Overall it is much less efficient to use a large number of cores, and difficult to fully utilise a large supercomputer to run a single planetary simulation very quickly. Fortunately, giant impact studies do not usually rely on a single high-resolution simulation, but instead on several simulations representing different scenarios, where parameters such as the velocity of impact and speed are changed. For this reason perfect scaling over multiple nodes is not essential, since many impacts can be simultaneously run at the same time over one or a few nodes.

1.3 Thesis Motivation and Outline

Giant impact simulations studies have barely considered spin in either the target or impactor, with a few exceptions of a proto-Earth spinning in a direction parallel to the orbital angular momentum, and recent attempts to model the outcome of simulations using machine learning (Timpe et al., 2020). However, it is very common to obtain from giant impacts a rapidly spinning planet, which could affect the outcome of a subsequent giant impact millions of years later. It was my goal, not only to study the effects of pre–impact spin in the case of the Moon forming impact, but also provide the community with a tool to set up giant impact simulations with spinning proto-planets.

With that tool in hand I was able to test if spin really had a minor role in giant impacts, as it was previously thought. A good test would be a spinning impactor, which effectively changes the total angular momentum of a canonical-like impact by only $\sim 5\%$. No significant differences should be found if it had no major importance. All these ideas are explained in Chapter 2.

After this first study and consequently understanding a bit better the tools I was using, I found SPH had a major problem when dealing with planetary simulations. The basic definition of the density field is smooth, but planets have density discontinuities. This problem translates to artificial forces in the core–mantle boundary, effectively repelling one material from another in these particular regions. The extent of this problem was poorly understood since only one method has been previously developed to tackle it. In Chapter 3 we propose a novel solution to this problem to finally get rid of this systematic uncertainty.

Finally I went back to the canonical scenario, this time to perform for the very first time simulations with a spinning proto-Earth whose angular momentum is misaligned with the orbital angular momentum of the impactor. The goal of Chapter 4 is to explore a mechanism to explain the Moon's orbit inclination today, which, according to some studies, should have been $\sim 10^\circ$ or higher at the moment of the formation of the Moon.

Chapter 2

Pre-impact spin in Moon-forming collisions

We simulate the hypothesised collision between the proto-Earth and a Mars-sized impactor that created the Moon. Amongst the resulting debris disk in some impacts, we find a self-gravitating clump of material. It is roughly the mass of the Moon, contains $\sim 1\%$ iron like the Moon, and has its internal composition resolved for the first time. The satellite contains mainly impactor material near its core but becomes increasingly enriched in proto-Earth material near its surface. The formation of this Moon-sized clump depends sensitively on the spin of the impactor. To explore this, we develop a fast method to construct models of multi-layered, rotating bodies and their conversion into initial conditions for smoothed particle hydrodynamical (SPH) simulations. We use our publicly available code to calculate density and pressure profiles in hydrostatic equilibrium, then generate configurations of over a billion particles with SPH densities within 1% of the desired values. This algorithm runs in a few minutes on a desktop computer, for 10^7 particles, and allows direct control over the properties of the spinning body. In comparison, alternative relaxation or spin-up techniques take hours on a supercomputer and the structure of the rotating body cannot be known beforehand. Collisions that differ only in the impactor's initial spin reveal a wide variety of outcomes: a merger, a grazing hit-and-run, or the creation of an orbiting proto-Moon.

2.1 Introduction

From planets and stars to dark matter haloes, self-gravitating spinning objects are common in astronomy. Their spin reflects the particular history of gravitational torques experienced by the material that they contain. By studying the angular momenta of astronomical systems, we can learn about the processes through which these objects formed.

As self-gravitating objects can only spin so fast without breaking apart, the orbital angular momentum of accreting material typically dominates over that present due to

spin. For instance, the final stage of planet formation involves giant impacts between planet-sized bodies (Chambers & Wetherill, 1998; Clement et al., 2019), and the pre-impact spins are usually ignored despite the fact that rapidly rotating bodies are a common outcome of such collisions (Kokubo & Genda, 2010; Li et al., 2020). Examples of this include attempts to explain Uranus' rotation axis using orbital angular momentum brought by a 2–3 $M_\oplus$ object (Slattery et al., 1992; Kegerreis et al., 2018), and models in which the angular momentum of the Earth–Moon system results from the impact of a non-rotating Mars-sized body, Theia, and a non-rotating proto-Earth (Canup & Asphaug, 2001).

The Moon-forming impact is one planetary example for which pre-impact spin has received consideration. Canup (2008) showed how pre-impact rotation changed the collision outcome relative to the canonical impact studied by Canup & Asphaug (2001). The isotopic similarity of the Earth's mantle and lunar samples (Wiechert et al., 2001) provoked attempts to place a higher fraction of proto-Earth material into the protolunar disk by starting with a spinning target (Ćuk & Stewart, 2012; Lock & Stewart, 2017; Wyatt et al., 2018). Initial conditions for these numerical simulation studies were created by first making a spherical planet, providing it with a small angular velocity, letting it relax in a smoothed particle hydrodynamical (SPH) simulation, then repeating this process until the desired angular velocity was reached (Ćuk & Stewart, 2012, supplementary materials). This method is slow and leads to pre-impact planets with structures that cannot be known until the end of this process.

Interest in the canonical impact model has been revived by the recent detection of oxygen isotope heterogeneity in returned lunar samples, where the signature of Theia becomes increasingly apparent in samples derived from deeper in the lunar mantle (Cano et al., 2020). Of particular relevance for our study are the frequently sighted clumps of SPH particles amongst the post-impact debris (e.g. Benz et al., 1987). These clumps form in the tidal arm of debris coming from the part of Theia that does not directly strike the proto-Earth (Canup, 2004). However, concerns over artificial clumping of SPH particles in shear flows (Imaeda & Inutsuka, 2002) and numerical convergence of results during the chaotic post-impact evolution (Canup et al., 2013; Asphaug, 2014) have left uncertain whether or not this clump could be the proto-Moon. Even when clumps were present in high resolution SPH simulations, they were most notable for their effect on the material in the smoother debris disk because their orbits led them to collide with the Earth in a matter of hours (Hosono et al., 2017).

Investigating the effect of spin on planetary collisions requires many simulations in which both the initial spin and internal composition are reliably generated. The

challenge of finding an elegant and efficient way to construct initial conditions has significant overlap with attempts to model the internal structures of gas giant planets using their measured gravitational moments. Much of this work has made use of the concentric Maclaurin spheroid (CMS) method introduced by Hubbard (2013), where a uniformly spinning planet is described as a superposition of constant-density spheroids – for which closed analytical solutions exist for the moments of the gravitational potential (Hubbard, 2012). This method has been developed to improve precision at high spin rates (Kong et al., 2013; Lock & Stewart, 2017), include differential rotation on cylinders (Wisdom & Hubbard, 2016) and increase the number of spheroids that can be included for a given computing time (Militzer et al., 2019). For example, measurements of the gravitational moments from the Juno mission (Iess et al., 2018) have been used in conjunction with CMS models to infer the extent of the differential rotation of Jupiter's atmosphere (Guillot et al., 2018). The situation for Saturn is complicated by the presence of extensive rings, but the CMS method has also been used to analyse recent Cassini measurements and study the planet's more extensive differential rotation (Iess et al., 2019).

In this chapter, we present a fast algorithm that calculates the internal density profile of a rotating object composed of any prescribed materials in hydrostatic equilibrium, and places particles into the body such that very little, if any, relaxation is required for numerical simulations. The method is based on the CMS technique without differential rotation, but it allows arbitrary equations of state to be used for multiple material layers and exploits an analytical expression for the gravitational potential rather than using a slower and less accurate truncated expansion of Legendre polynomials. Our open-source code is a flexible tool that has been written in python under the project name WoMa (World Maker). It is described in §2.2, tested in §2.3 and publicly available at `https://github.com/srbonilla/WoMa`. In §2.4 we use WoMa to construct initial conditions for a set of giant impacts between the proto-Earth and Mars-sized impactors with a variety of rotation rates. Conclusions are presented in §2.5.

2.2 Initial conditions generation

In this section, we describe our method for creating particulate realisations of uniformly spinning spheroids. It entails: (1) iteratively solving the equation of hydrostatic equilibrium to create an interior model of the spinning object, and (2) sampling the three-dimensional solution with particles, arranged such that their SPH densities match the desired values.

2.2.1 Interior model

Within the reference frame of a body spinning about its z-axis with constant angular velocity Ω, the equation of hydrostatic equilibrium can be written using cylindrical coordinates, $\vec{r} = (r_{xy}, \alpha, z)$, as

$$\frac{1}{\rho}\nabla P = -\nabla\phi - \Omega^2 r_{xy}\,\hat{r}_{xy}\ , \tag{2.2.1}$$

where $P(r_{xy}, z)$, $\rho(r_{xy}, z)$, and $\phi(r_{xy}, z)$ represent the azimuthally symmetric pressure, density, and gravitational potential solution to the Poisson's equation $\nabla^2\phi = 4\pi G\rho$ (where G is the universal gravitational constant). The third term represents the centrifugal force and is directed away from the rotation axis. The right hand side of equation Equation 2.2.1 can be viewed as the negative gradient of an effective potential, Ψ, that includes the gravity and angular momentum barrier terms:

$$\Psi = \phi + \frac{1}{2}\Omega^2 r_{xy}^2\ . \tag{2.2.2}$$

To solve equation Equation 2.2.1 we also need a sufficient selection of the following quantities to make the problem well-defined: an equation of state (EoS), $P(\rho, T)$, and a temperature–density relation, $T(\rho)$, for each material; the pressure, $P_{\rm s}$, density, $\rho_{\rm s}$, and temperature, $T_{\rm s}$, at the surface of the object; the total mass, M, radius of the non-rotating solution, $R_{\Omega=0}$, and locations of any boundaries between distinct material layers in the non-rotating body, $R_{B,\Omega=0}$. Note that not all of these variables need to be specified as inputs for WoMa. The EoS, the temperature-density relation, and two of the three boundary conditions ($P_{\rm s}$, $\rho_{\rm s}$, and $T_{\rm s}$) must always be specified. However, various combinations of the other quantities can be used as inputs; For a one-layer planet, WoMa can determine the total mass given the radius and vice versa. For a two-layer planet, there are three quantities of interest: total mass, radius, and boundary between materials. WoMa can determine one given the other two as inputs. In addition it can determine boundary and radius given the masses of the two layers. For a three-layer planet, the quantities of interest are boundary core-mantle, boundary mantle-atmosphere, total mass, and radius. WoMa can determine one given the other three as inputs. It can also determine the two boundaries given the total mass, radius and moment of inertia of the planet. All options are described and documented at `https://github.com/srbonilla/WoMa`.

The solution to equation Equation 2.2.1 for a constant density object is the Maclaurin (oblate) spheroid (Tassoul, 1978), and more general solutions can be described as systems of overlapping concentric Maclaurin spheroids (Hubbard, 2013). Then, the density at any point inside the planet is the sum of the densities of all of the

spheroids containing that point. As the isodensity surfaces are all spheroids, we can describe the full three-dimensional solution to equation Equation 2.2.1 using just the equatorial and polar density profiles.

Our approach to solving equation Equation 2.2.1 begins by finding the density profile for the spherically symmetric, non-rotating ($\Omega = 0$) case. This solution, $\rho_{\Omega=0}(r)$, is evaluated in two one-dimensional arrays, one in each of the equatorial and polar directions. These arrays both contain N_g elements and span out to $r_{xy} = 1.5R_{\Omega=0}$ and $z = 1.2R_{\Omega=0}$. These maxima can be increased, if needed, for very rapidly rotating objects. $\rho_{i=0}(r_{xy}, z)$ is used to compute the first value of the effective potential, Ψ_1, via

$$\Psi_i(r_{xy}, z) = G \iiint \frac{\rho_{i-1}(r_{xy}, z)}{|\vec{r} - \vec{r'}|} d^3r' + \frac{1}{2}\Omega^2 r_{xy}^2 \ . \tag{2.2.3}$$

The iteration loop is closed by updating the density, $\rho_i(r_{xy}, z)$, as the solution to

$$\frac{1}{\rho_i(r_{xy}, z)} \nabla P_i(r_{xy}, z) = -\nabla \Psi_i(r_{xy}, z) \ , \tag{2.2.4}$$

where $P_i(r_{xy}, z) = P(\rho_i, T_i)$ is determined by the EoS. These iterations do not conserve the total mass of the object. However, WoMa will loop over different $M_{\Omega=0}$ values, or whichever variable is relevant, until a solution is found with the desired mass.

The iterative process is continued until the mean fractional difference between the two last equatorial density profiles falls below a specified threshold. This corresponds to $c < 10^{-3}$, where the convergence statistic is defined as

$$c \equiv \frac{1}{N_g} \sum_{j=1}^{N_g} \frac{|\rho_i(r_{xy,j}) - \rho_{i-1}(r_{xy,j})|}{\rho_{i-1}(r_{xy,j})}, \tag{2.2.5}$$

and the average is determined using only elements j for which $\rho_i(r_{xy,j})$ and $\rho_{i-1}(r_{xy,j})$ are both non-zero.

For uniform-density oblate spheroids, the three-dimensional integral to find the gravitational potential in equation Equation 2.2.3 can be recast as a one-dimensional integration. Defining the semi-major and semi-minor axes as R and Z respectively, the gravitational potential due to an oblate spheroid of constant density ρ, can be written as (Kellogg, 1929)

$$\phi(r_{xy}, z) = -G\rho\pi R^2 Z \int_\lambda^\infty \left(1 - \frac{r_{xy}^2}{R^2 + s} - \frac{z^2}{Z^2 + s}\right) \frac{ds}{\sqrt{\varphi(s)}} \ , \tag{2.2.6}$$

where $\varphi(s) \equiv (R^2 + s)^2(Z^2 + s)$, and $\lambda = 0$ if (r_{xy}, z) lies within the spheroid, or the biggest root of the equation $f(s) = 0$ otherwise, where

$$f(s) \equiv \frac{r_{xy}^2}{R^2+s} + \frac{z^2}{Z^2+s} - 1 \,. \tag{2.2.7}$$

Equation Equation 2.2.6 can be solved analytically along the axis $r_{xy} = 0$ and in the plane $z = 0$, both inside and outside the spheroid, to give

$$\frac{\phi(z)}{A} = \left[\frac{2z^2}{(R^2-Z^2)\sqrt{Z^2+t}} + 2\left(\frac{R^2+z^2-Z^2}{(R^2-Z^2)^{3/2}}\right)\tan^{-1}\gamma \right]_{t=\lambda}^{t\to\infty} \tag{2.2.8}$$

for $r_{xy} = 0$, and

$$\frac{\phi(r_{xy})}{A} = \left[\frac{-r_{xy}^2\sqrt{t+Z^2}}{(R^2+t)(R^2-Z^2)} + \frac{2R^2+2Z^2-r_{xy}^2}{(R^2-Z^2)^{3/2}}\tan^{-1}\gamma \right]_{t=\lambda}^{t\to\infty} \tag{2.2.9}$$

for $z = 0$, where $A \equiv -G\rho\pi R^2 Z$ and $\gamma^2 \equiv (t+Z^2)(R^2-Z^2)$. We use this analytical solution to calculate the gravitational potential rapidly at any point in space, rather than the usual truncated expansion in Legendre polynomials.

2.2.2 Particle placement for SPH simulations

In order to simulate a spinning body using a particle-based method like SPH, the solution for the density, $\rho(r_{xy}, z)$, found in §2.2.1 must be converted into an appropriate set of particles. Desirable features of such a partitioning of the volume are that the particles should have very similar masses, no large-scale symmetries should be introduced that are not present in the body itself, and the particle distribution should be locally homogeneous to avoid introducing scatter in the densities of the particles. For spherically symmetric objects, these aims have led to approaches that place particles in nested spherical shells (Saff & Kuijlaars, 1997; Raskin & Owen, 2016; Reinhardt & Stadel, 2017; Kegerreis et al., 2019). In this subsection we build on the work of Kegerreis et al. (2019), generalising their stretched equal-area (SEA) algorithm to the case where particles are placed into spheroidal isodensity shells.

We start by using SEAGen (Kegerreis et al., 2019) to create a spherical object with a radial density profile matching the equatorial profile of our desired spheroid and containing the desired number of particles, N. SEAGen arranges I spherical shells of particles such that the final one lines up with the edge of the body and any interior boundaries between different material layers are similarly accommodated. The midpoints of these shells have radii R_i representing the semi-major axes of the shells of particles in our desired spheroidal object. The semi-major and semi-minor

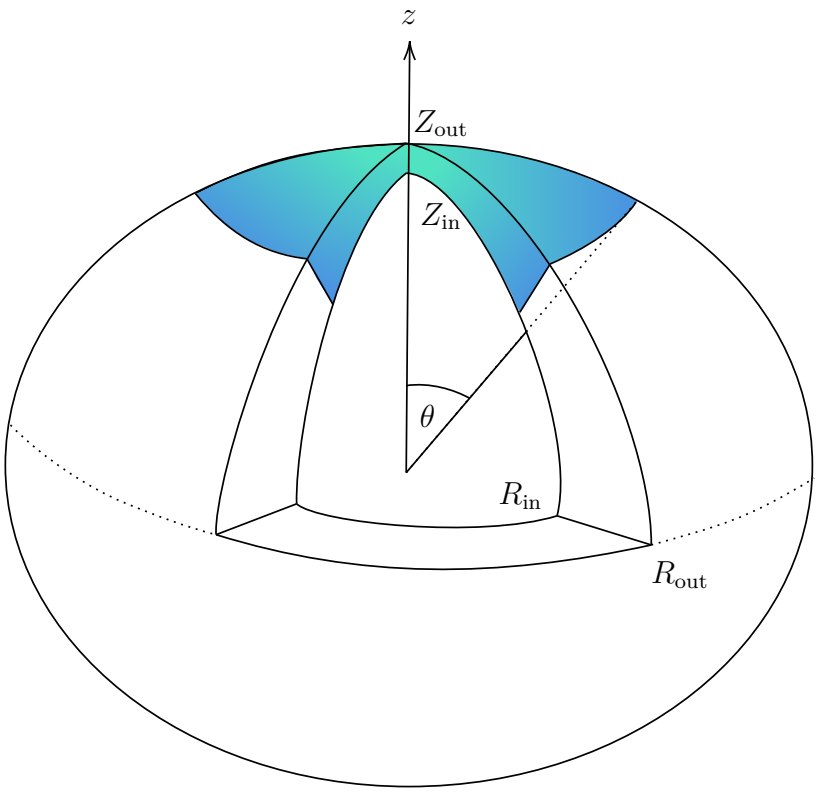

Figure 2.1: Illustration of the fractional volume enclosed within a polar angle θ, $V(<\theta)$, for a spheroidal shell, which dictates the latitudinal arrangement of particles required to represent a constant-density spheroidal shell.

axis boundaries of the spheroidal shells are given by

$$\begin{aligned} R_{i,\rm out} &= \frac{R_i + R_{i+1}}{2}, \quad Z_{i,\rm out} = \frac{Z_i + Z_{i+1}}{2}, \\ R_{i,\rm in} &= \frac{R_i + R_{i-1}}{2}, \quad Z_{i,\rm in} = \frac{Z_i + Z_{i-1}}{2}, \end{aligned} \tag{2.2.10}$$

where, by definition, $R_{i,\rm out} = R_{i+1,\rm in}$ and $Z_{i,\rm out} = Z_{i+1,\rm in}$. Using the solution to equation Equation 2.2.1 calculated in §2.2.1, the total mass in each spheroidal shell, M_i can be computed. The number of particles in each spheroidal shell, N_i, is then set as the nearest integer to $(M_i/M)N$, to ensure that the total number of particles in the spheroid is as close as possible to the desired value N.

The SEAGen algorithm is employed again to create I spherical shells that are randomly rotated with respect to one another, placing N_i particles with mass M_i/N_i into the $i^{\rm th}$ shell. To transform from spherical to spheroidal shells, each particle is: (1) shifted in polar angle, θ, to reproduce the cumulative mass (or equivalently, volume or particle number) fraction distribution of the spheroidal shell, $f_i(<\theta)$, then (2) mapped at fixed polar and azimuthal angle to place it onto the required

spheroidal shell.

SEAGen provides us with spherical isodensity shells of particles, which have a cumulative fractional number that satisfies

$$f_{\rm sphere}(<\theta) = (1-\cos\theta)/2. \tag{2.2.11}$$

The corresponding function for the $i^{\rm th}$ isodensity spheroidal shell, $f_i(<\theta)$, is more complicated because the shell has a θ-dependent radius and thickness. For the $i^{\rm th}$ spheroidal shell, bounded by the spheroids with semi-major and semi-minor axis pairs ($R_{i,\rm in}$, $Z_{i,\rm in}$) and ($R_{i,\rm out}$, $Z_{i,\rm out}$), the cumulative enclosed volume, as illustrated in Figure 2.1, can be written as

$$\begin{aligned} V_i(<\theta) &= \int_0^{2\pi} d\phi' \int_0^{\theta} \sin\theta' \int_{r_{i,\rm in}(\theta')}^{r_{i,\rm out}(\theta')} r'^2 dr' d\theta' \\ &= \frac{2\pi}{3}\int_0^{\theta} \left(r_{i,\rm out}(\theta')^3 - r_{i,\rm in}(\theta')^3\right)\sin\theta' d\theta' \,, \end{aligned} \tag{2.2.12}$$

where $r_{i,j}(\theta') = \left(\dfrac{\sin^2(\theta')}{R_{i,j}^2} + \dfrac{\cos^2(\theta')}{Z_{i,j}^2}\right)^{-1/2}$, with $j = \{\rm in\,, out\}$, is the distance from the centre of the coordinate system to the inner or outer spheroid surface, at a given polar angle. The solution of Equation 2.2.12 is

$$\begin{aligned} V_i(<\theta) = \frac{2\pi}{3}\Bigg[\sqrt{2}\left(-\frac{R_{i,\rm out}^2}{F_{i,\rm out}(\theta)} + \frac{R_{i,\rm in}^2}{F_{i,\rm in}(\theta)}\right)\cos\theta \\ + R_{i,\rm out}^2 Z_{i,\rm out} - R_{i,\rm in}^2 Z_{i,\rm in}\Bigg] \,, \end{aligned} \tag{2.2.13}$$

where

$$F_{i,j}(\theta) = \sqrt{R_{i,j}^{-2} + Z_{i,j}^{-2} + \left(-R_{i,j}^{-2} + Z_{i,j}^{-2}\right)\cos 2\theta}\,.$$

As the shell is assumed to have a uniform density, we can infer that the cumulative fractional number of particles in the spheroidal shell should satisfy $f_i(<\theta) = V_i(<\theta)/V_i(<\pi)$.

Having determined $f_i(<\theta)$ for each shell and $f_{\rm sphere}(<\theta)$, we can now define the polar angle mapping of the particles on a SEAGen-generated spherical shell to the corresponding spheroidal shell via

$$\theta \rightarrow f_i^{-1}\left(f_{\rm sphere}(<\theta)\right) = f_i^{-1}\left(\frac{1-\cos\theta}{2}\right). \tag{2.2.14}$$

With the particles now distributed in a uniform and unbiased way with respect to the polar angle, the final step is to map their radial positions from the spherical shell that SEAGen placed them on to the desired spheroidal one, using

$$r \rightarrow \left(\frac{\sin^2(\theta)}{R_i^2} + \frac{\cos^2(\theta)}{Z_i^2}\right)^{-1/2} r. \tag{2.2.15}$$

Table 2.1: Properties of the planets used as input to WoMa's iterative solution of Equation 2.2.1 for the one- and two-layer test cases.

Property		One-layer	Two-layer
Mass	M [$M_\oplus$]	0.640	1
Radius	$R_{\Omega=0}$ [$R_\oplus$]	1	1
Boundary	$R_{B,\Omega=0}$ [$R_\oplus$]	-	0.481
Period	T_Ω [hours]	3.25	2.60
Surface density	ρ_s [kg m^{-3}]	2450.1	2511.8
Surface pressure	P_s [Pa]	10^5	10^5
Surface temperature	T_s [K]	3000	300

2.3 Tests of the initial conditions generation

In this section we test the WoMa algorithm described in §2.2, in particular the iterative method to solve the equation of hydrostatic equilibrium for a uniformly rotating spheroid, and the technique to distribute particles to produce a low-noise representation of the solution. To demonstrate the capabilities of WoMa, we construct one- and two-layer planets using from 10^5 particles – as are commonly used in SPH simulations of planetary giant impacts – up to 10^9 particles, an order of magnitude more than the highest numbers to date (Hosono et al., 2017; Kegerreis et al., 2019, 2020), and evolve them to check how relaxed these initial conditions actually are.

2.3.1 Finding the dynamical equilibrium configuration

WoMa has been written in a modular way such that different EoS and temperature-density relations can be readily included. For our test planets we use publicly available EoS: SESAME basalt (Lyon & Johnson, 1992) to describe the material comprising the one-layer planet, and Tillotson iron and granite (Tillotson, 1962; Melosh, 1989) for the two-layer planet core and mantle respectively. The one-layer planet is assumed to be isothermal, whereas $T = k\rho^{2.5}$ is chosen for illustrative purposes for both materials of the two-layer test case. The other parameters and boundary conditions describing the non-spinning objects, from which WoMa iterates to find the rotating bodies, are given in Table 2.1. Figure 2.2 shows, with solid lines, the radial density profiles for the resulting spherically symmetric solutions.

We define the maximally-spinning body to be the most rapidly uniformly rotating one for which the centrifugal force does not overcome gravity at any point within the object. If this requirement is violated within our uniformly rotating body, then the

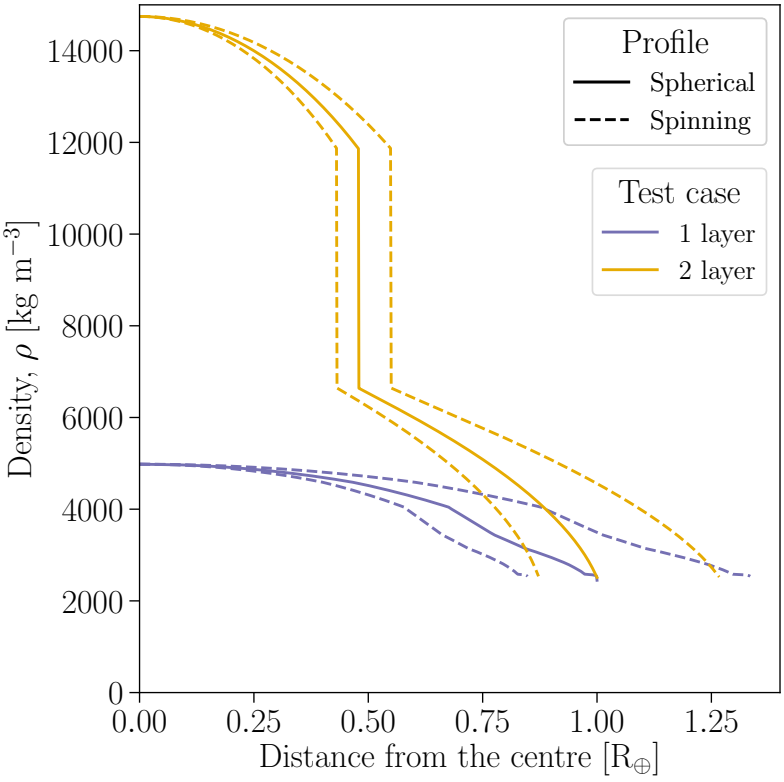

Figure 2.2: Analytically–solved density profiles for the spherical and spinning planets. Solid lines represent the initial spherical models, and dashed lines represent the polar and equatorial density profiles, left and right respectively, of the corresponding uniformly rotating fluid planets that solve equation Equation 2.2.1. Note that the kinks in the profile of the one-layer planet reflect phase changes in the SESAME basalt EoS.

force resulting from the pressure gradient would need to act inwards, leading to an unphysical situation. For our solid body rotating one- and two-layer planets, these maximum spins correspond to periods of $T_{\Omega,\text{min}} = 3.03$ and 2.27 hours respectively. We choose very short periods of $T_\Omega = 3.25$ hours for the one-layer test, and $T_\Omega = 2.60$ hours for the two-layer case, in order to yield significantly flattened objects. Using grids with $N_g = 10^5$ elements, the iterative procedure within WoMa finds the equilibrium configurations for our test planets with their respective rotation periods. The polar and equatorial density profiles are shown, for both cases, using dashed lines in Figure 2.2.

It is important to demonstrate the convergence of this iterative scheme. To this end, we use the convergence statistic defined in equation Equation 2.2.5, applied to the N_g-sized equatorial density array. This is simply computing the mean fractional

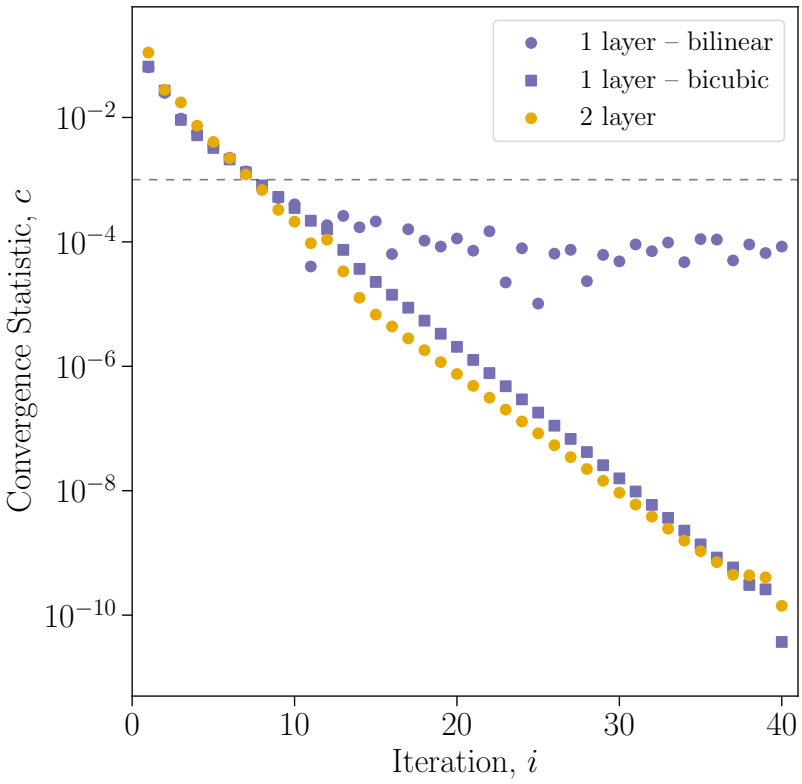

Figure 2.3: Convergence of the equatorial density profile, measured by the statistic c defined in equation Equation 2.2.5, as a function of iteration number. For the one-layer test we use two versions of the basalt EoS with either bilinear or bicubic interpolation of the SESAME tables. Bicubic interpolation ensures that the derivatives of $P(\rho, T)$ are continuous at every given ρ and T and produces better convergence. $c < 10^{-3}$, beneath the dotted line, is more than sufficient for making SPH initial conditions such as those we use here, and is rapidly achieved by WoMa.

change in the equatorial density profile over the previous iteration. The evolution with iteration number of the convergence statistic is shown in Figure 2.3. For the purposes of typical numerical simulations, the precision necessary is reached in only a few iterations, with both the one-and two-layer cases able to converge to much higher precision provided that a differentiable EoS is employed. For a bilinear interpolation of the SESAME basalt EoS table, Figure 2.3 shows that the convergence reaches a floor, albeit one in this instance that is still sufficiently low for our purposes. The height of this floor depends somewhat on the coarseness of the computational grid, and can be reduced significantly using a smoother interpolation, such as the bicubic one shown in Figure 2.3 or the often-used rational function interpolation. For the results shown here, $N_g = 10^5$, and 15 iterations take under 5 minutes to compute

on a common desktop computer. This resolution will suffice for the mass of the innermost spheroid to be smaller than the mass of one particle when placing up to $\sim 10^{11}$ particles.

2.3.2 Particle placement for SPH simulations

To test that the particle placement algorithm leads to low-noise representations of the test planets we use WoMa to create particle representations of both cases using 10^5, 10^7, and 10^9 particles. We test the accuracy of these representations by computing the particles' smoothed densities using the SPH code SWIFT (www.swiftsim.com, Schaller et al., 2016) and 45 nearest neighbours. The distributions of fractional density errors are shown in Figure 2.4. These distributions are all sharply peaked around zero, with full-widths at half-maximum of the peaks of 0.015, 0.012, and 0.005 for the 10^5, 10^7, and 10^9 particle realisations respectively. Better numerical resolution means decreased SPH smoothing lengths that sample a smaller range of densities, and lower stochastic errors in the sampled densities.

In addition to the bulk of the particles that lie in the central peak of the density error distribution, Figure 2.4 shows some particles whose densities differ by up to 40%. These outliers arise at the density discontinuities of the outer surface and inner boundary between materials, and are an unavoidable consequence of how the standard SPH formulation computes densities by averaging over a number of nearby neighbours – a well-known issue when performing SPH computations of a density profile with discontinuities (Woolfson, 2007; Reinhardt & Stadel, 2017). Our choice of SPH formulation with smoothed densities is entirely responsible for this part of the error distribution, not the particle placement being performed by WoMa. Figure 2.4 shows that using more particles decreases the fraction of density outliers, because in these cases a smaller fraction of the particles lie near to boundaries.

We now test how close to equilibrium our test planets are by using the SWIFT code to evolve them both, for the three resolution levels, in a non-rotating reference frame. Each isolated rotating body is evolved to a simulation time of 20,000 s, i.e. just over 5.5 hours. This is close to 2 full rotations for both planets, and is several times the time taken for a sound wave to traverse the planet, so will be long enough to detect signs of disequilibrium. We measure a rotation period and a residual velocity for each particle, i. These are calculated as

$$T_{\Omega,i} = \frac{2\pi}{\Omega_i} \ , \quad \text{where} \quad \Omega_i = \frac{v_{\alpha,i}}{\sqrt{x_i^2 + y_i^2}} \ , \quad \text{and}$$
$$\vec{v}_{\text{res},i} = \vec{v}_i - \vec{\Omega} \times \vec{r}_i \ , \tag{2.3.1}$$

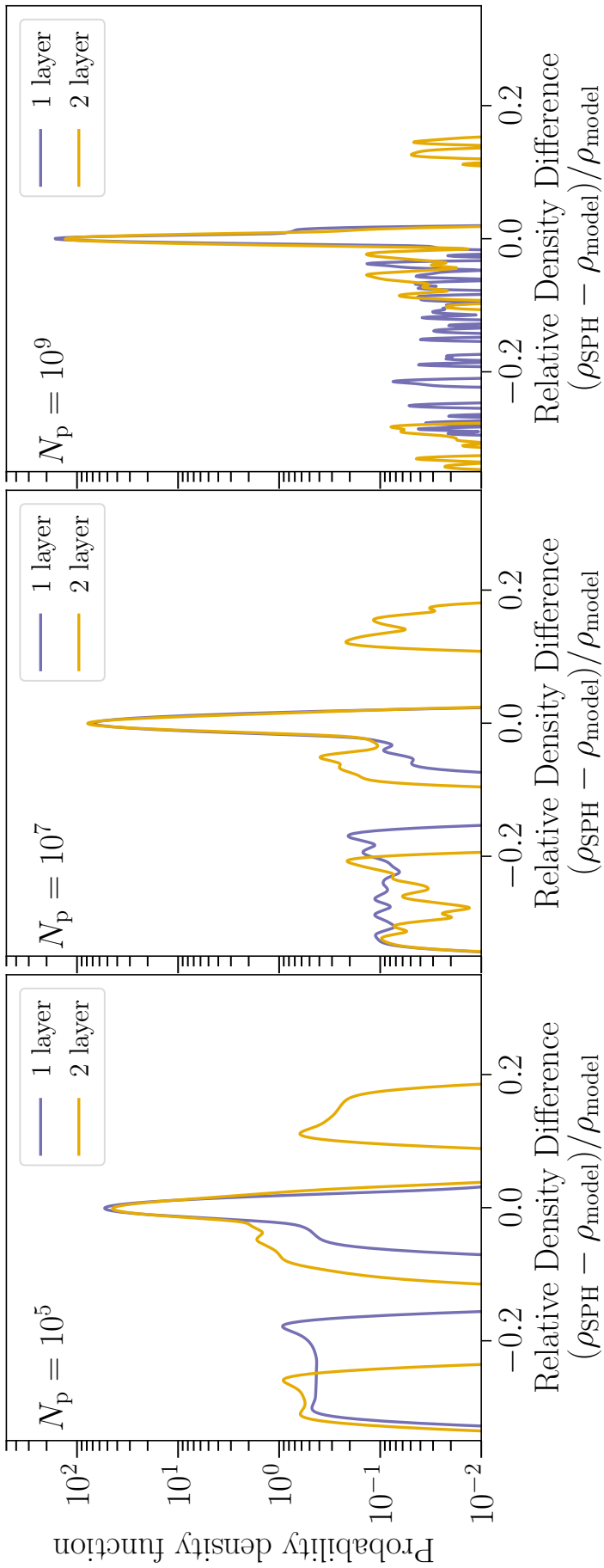

Figure 2.4: Comparison of our model solution for hydrostatic equilibrium with the SPH density computed at each particle's location in the initial conditions. The first, second, and third columns contain the initial conditions with 10^5, 10^7, and 10^9 particles respectively, and the different colours reflect the results for the one- and two-layer planets.

i.e. the SPH velocity minus the velocity each particle should have according to its position and the chosen angular velocity. The evolution of the median of the particle rotation periods, normalised by the desired period, and the median residual speed relative to the escape speed are shown in Figure 2.5, along with the 1^{st} and 99^{th} percentiles. The distribution of particle periods has a median that matches the desired value to within 1% at all times, and very low scatter by the end of the simulations in all cases. Median residual speeds never reach 2% of the escape speed, and barely exceed the 1% level for the two higher resolutions. We define a set of initial conditions as “relaxed" when the median particle speed is below 1% of the escape speed. In both the one- and two-layer cases, higher resolutions lead to shorter relaxation times.

We also compute the fractional density error distribution at the end of the simulation. Full-widths at half-maximum of the peaks are at 0.007, 0.004, and 0.006 for the one-layer test case, and 0.016, 0.008, and 0.019 for the two-layer test case, for the 10^5, 10^7, and 10^9 particle realisations respectively. The final density profiles, excluding the boundaries, are within 2% of the desired, analytically–computed density for the one- and two-layer tests with 10^5 particles, and within 1% for the two higher resolutions.

2.4 The effects of a spinning Theia

In this section, we present a set of five canonical Moon-forming giant impacts where the impactor Theia is given a different spin in each simulation. The full parameter space for such a study includes the spin angular velocity vectors of both proto-Earth and Theia, but in this initial study we restrict ourselves to situations with the spin and orbital angular momenta either parallel or anti-parallel and the target not initially rotating. Collisions between rotating protoplanets have been considered previously, both for the Moon-forming collision (Canup, 2008; Ćuk & Stewart, 2012; Nakajima & Stevenson, 2015; Wyatt et al., 2018) and terrestrial planets more generally (Timpe et al., 2020), but not at particularly high numerical resolution. Recent studies (Hosono et al., 2017; Kegerreis et al., 2019) have shown that at least 10^7 particles can be required to converge on even large-scale quantities, like the rotation rate of the planet or the mass of the resulting debris disk. The combination of WoMa and SWIFT enable us to produce better resolved simulations to investigate how Theia’s spin can alter the outcome of the canonical Moon-forming collision.

We consider an impact between a target proto-Earth of mass 0.887 $M_\oplus$ and an impactor, Theia, of mass 0.133 $M_\oplus$. Both are differentiated into an iron core and

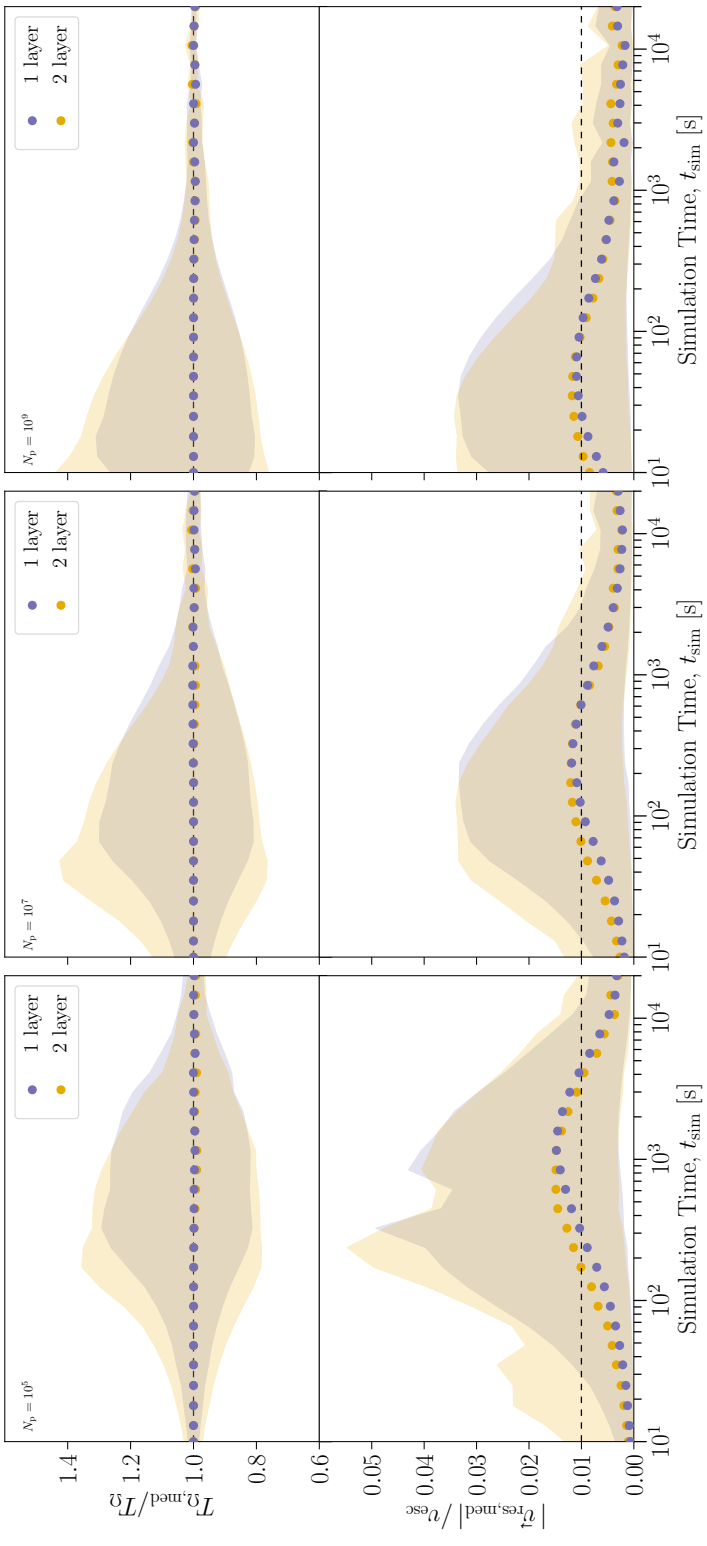

Figure 2.5: Evolution of the median normalised period $T_{\Omega,\mathrm{med}}/T_\Omega$ (upper row), and median normalised residual speed $|\vec{v}_{\mathrm{res,med}}|/v_{\mathrm{esc}}$ (lower row). Shaded regions represent the 1st and 99th percentiles of the distributions. The first, second, and third columns contain the simulations with 10^5, 10^7, and 10^9 particles respectively. A horizontal line shows where the residual velocity has a magnitude that is 1% of the escape speed, a criterion sometimes used to define when initial conditions are relaxed.

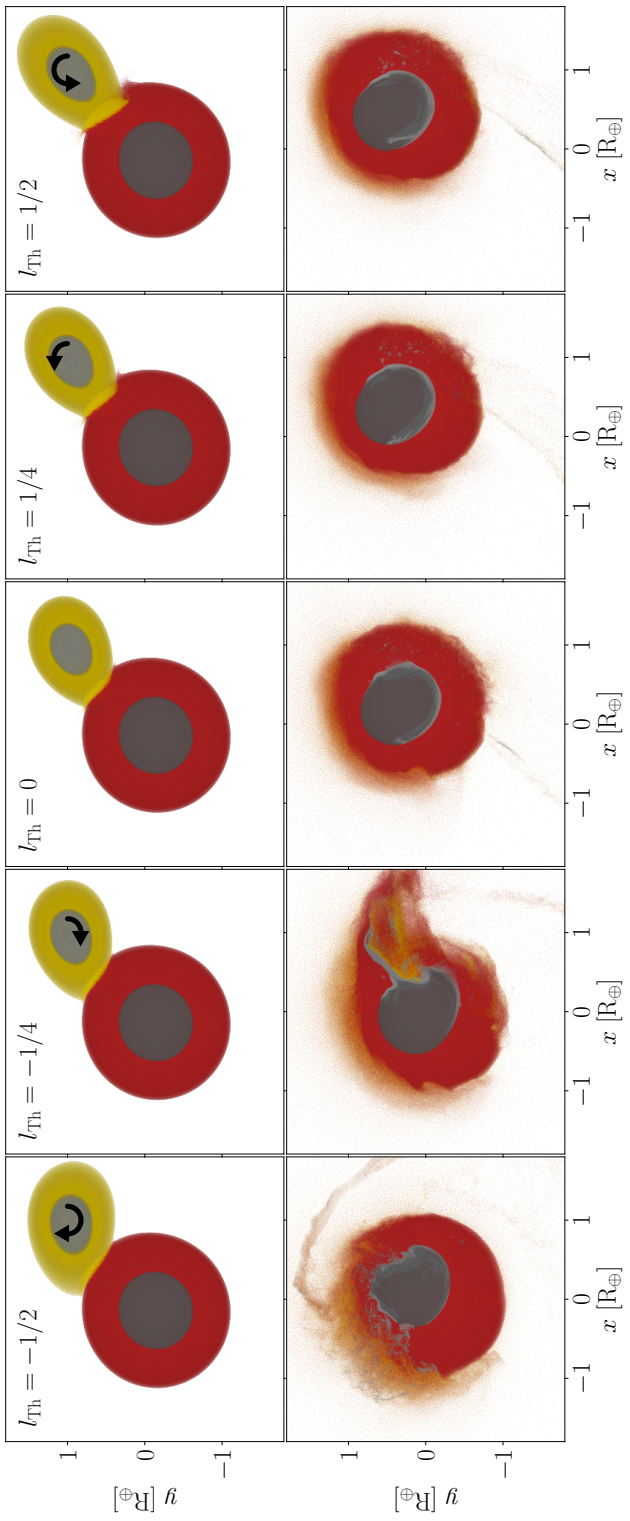

Figure 2.6: Snapshots in the early stages of the five giant impacts. Rows represent simulation times of 1 hour (top) and 5 hours (bottom). Columns represent different simulations with $l_{\rm Th} = -\frac{1}{2}$, $-\frac{1}{4}$, 0, $\frac{1}{4}$, and $\frac{1}{2}$. 50 slices of thickness $\Delta z = 0.12\ R_\oplus$ are plotted in order of increasing z from $z = -6\ R_\oplus$ to $z = 0$, which lies in the plane containing the centre of mass. The particle colours represent different materials: dark and light grey for Tillotson iron, and red and yellow are Tillotson granite, in the proto-Earth and Theia respectively. The origin of the coordinate system is taken to be the centre of mass of all the material in the simulation.

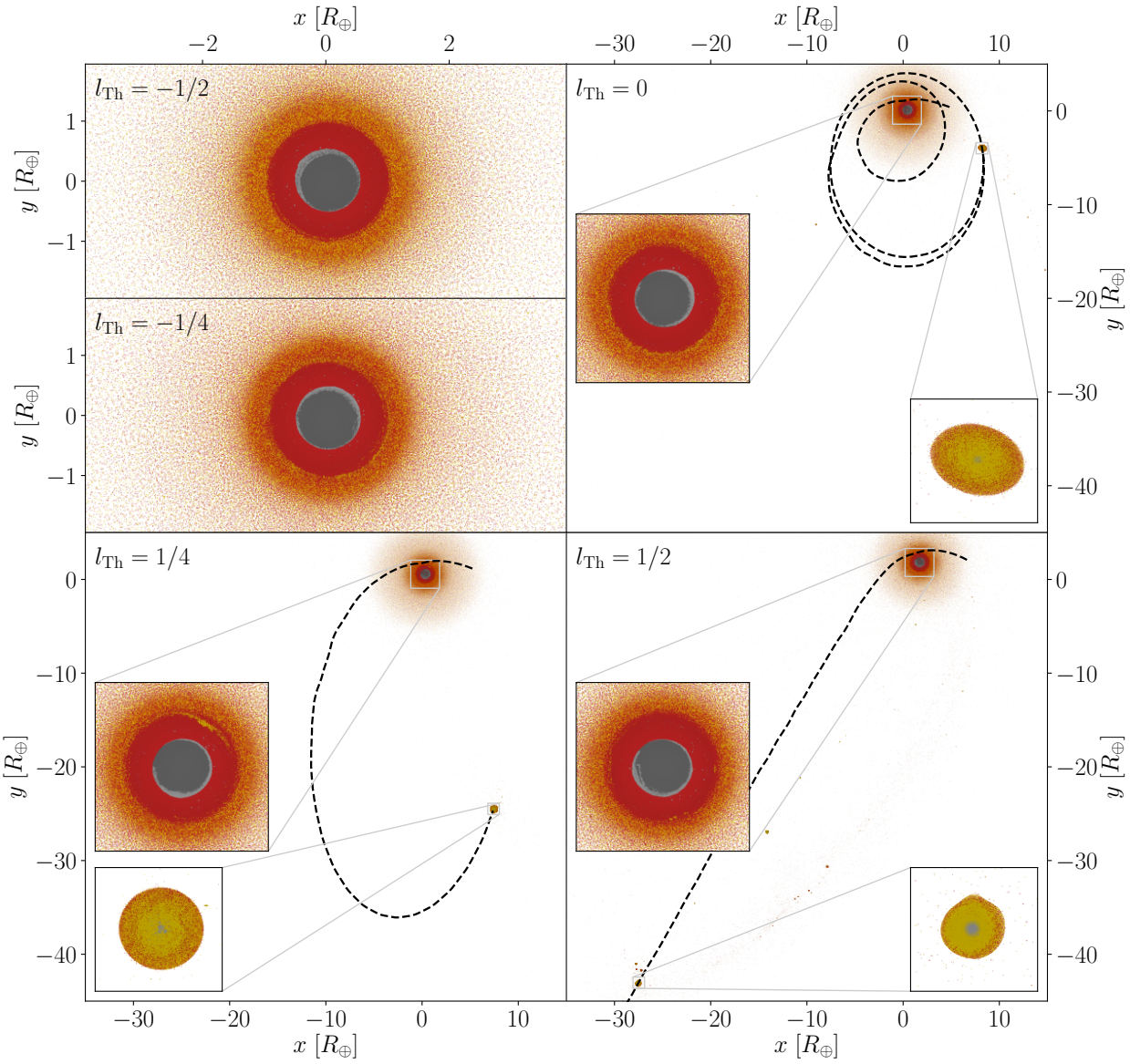

Figure 2.7: Snapshots at 100 hours of simulation time for simulations with $l_{\rm Th} = -\frac{1}{2}$, $-\frac{1}{4}$, 0, $\frac{1}{4}$, and 40 hours for the $l_{\rm Th} = \frac{1}{2}$ simulation. Blue lines represent the trajectories of the resulting clumps, and the particle colours are the same as in Figure 2.4. The inset boxes show regions of side length 3 $R_\oplus$ centred on the target and 1.2 $R_\oplus$ for the clump in each panel. An animation of the early evolution of these impacts is available at icc.dur.ac.uk/giant_impacts.

rocky mantle, constituting 30% and 70% of the total mass respectively modelled using the Tillotson (1962) iron and granite equations of state. The Tillotson EoS is widely used for SPH impact simulations due to its computationally convenient analytical form (Stewart et al., 2020). However it does not treat phase boundaries or mixed phases correctly. Since the focus of this chapter is the overall range of outcomes due to the spin of an impactor, the details of the EoS are not expected to have a significant effect on the main results. The velocity at impact is chosen to be the mutual escape speed, the angle of impact is set as 45°, and the simulation begins 1 hour prior to the time of contact between the two bodies in order to model the tidal distortion of the bodies just before impact. We give the iron and granite layers a temperature–density relation of $T \propto \rho^2$. With a 500 K surface temperature on both bodies, this yields a core temperature for the proto-Earth of ~ 5000 K, similar to the Earth today. All five simulations are evolved to 100 hours, and have a mass resolution of 10^7 particles per Earth mass.

The only difference between our simulations is the rotation rate of Theia. The minimum period available is 2.6 hours, which translates to a maximum spin angular momentum of $L_{\rm Th,max} = 0.15\ L_{\rm EM}$, where $L_{\rm EM} = 3.5 \times 10^{34}$ kg m^2 s^{-1} is the current angular momentum of the Earth–Moon system. We set the spin angular momentum of Theia, $L_{\rm Th}$, to be $l_{\rm Th} \equiv L_{\rm Th}/L_{\rm Th,max} = -\frac{1}{2}$, $-\frac{1}{4}$, 0, $\frac{1}{4}$, and $\frac{1}{2}$ for our five simulations. These correspond to rotation periods for the more and less rapidly spinning Theias of 3.2 and 5.1 hours. The orbital angular momentum of the colliding systems is $1.25\,L_{\rm EM}$, which is only $\sim 0.05\,L_{\rm EM}$ larger than the values of the successful canonical impacts found by (Canup & Asphaug, 2001).

Figure 2.6 shows cross sections of the moment of contact and a snapshot 4 hours later for each of the simulations. The most striking feature at the moment of impact is the difference in Theia's tidal distortion, which would have been absent had we started the simulation at the point of contact, as is often done in planetary giant impact studies (Canup, 2004). The tidal bulge of the more rapidly counter-rotating impactor ($l_{\rm Th} = -\frac{1}{2}$) has spun significantly ahead of the line joining the centres of the proto-Earth and Theia, stretching Theia along its direction of motion. For the rapidly co-rotating case ($l_{\rm Th} = \frac{1}{2}$), Theia's spin shifts the tidal distortion to point along the line connecting the centres of the bodies. Four hours after first contact, the counter-rotating impacts are near to completing their mergers, whereas the non-spinning and co-rotating largest remaining objects have drifted away from the origin of the coordinate system, chosen as the centre of mass of the simulation, reflecting the presence of significant unaccreted mass. The impactor core and mantle material that has already been deposited into the target is found towards the edges of the corresponding layers of the target, with more mixing between the two mantles.

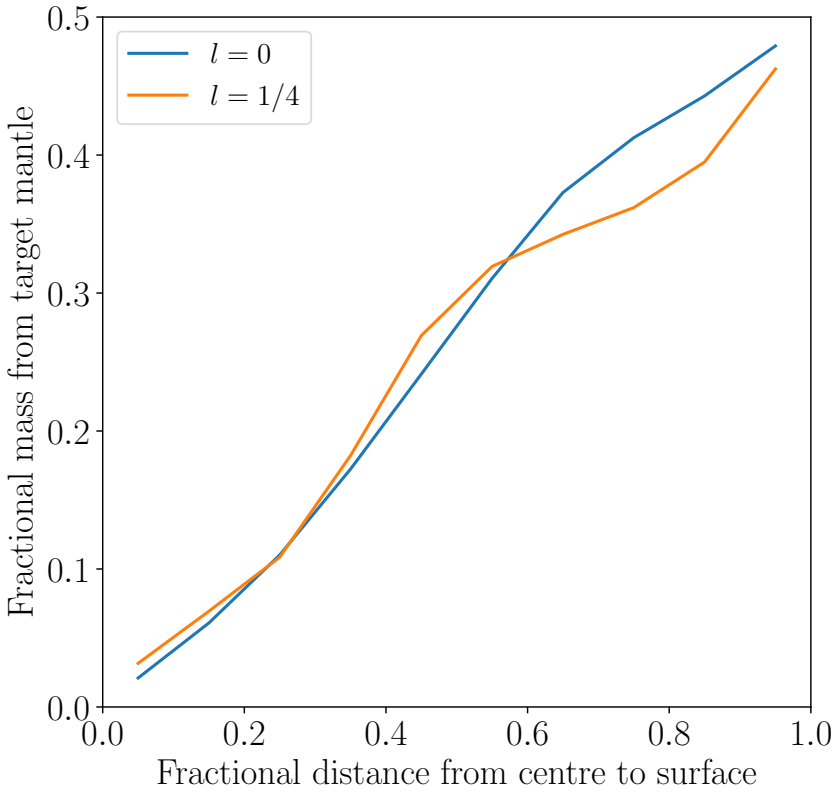

Figure 2.8: Radial variation of the mass fraction of target mantle present in the orbiting clumps after 100 hours, for the $l = 0$ (blue) and $l = \frac{1}{4}$ (orange) simulations.

Later snapshots of the five simulations are shown in Figure 2.7. Snapshots are shown at 100 hours of simulation time except for the $l_{\mathrm{Th}} = \frac{1}{2}$ case, which is at 40 hours to capture the highlighted clump before it flies out of frame. All $l_{\mathrm{Th}} < \frac{1}{2}$ simulations place the majority of the mass of Theia either into the Earth or within the Roche radius ($\sim 3\ R_{\oplus}$), with much of Theia's core blanketing that of the proto-Earth. The Roche radius is the distance from a celestial object, in our case the post-impact Earth, at which a second self-gravitating body with negligible bulk tensile strength in a circular orbit would break apart due to tidal forces. This quantity is computing by balancing the self-gravitational force of the second body at its point closest to the main body with the tidal force at that same point due to the first body:

$$R_{\mathrm{Roche}} = 2.44\, R_M \left(\frac{\rho_M}{\rho_m}\right)^{1/3}, \tag{2.4.1}$$

where R_M, ρ_M are the radius and density of the primary celestial body, and ρ_m is the density of the secondary celestial body (Roche, 1849).

The $l_{\mathrm{Th}} = 0$ and $\frac{1}{4}$ impacts lead to a large, self-gravitating clump within the debris disk that extends beyond the Roche radius. The formation of this clump is sensitive

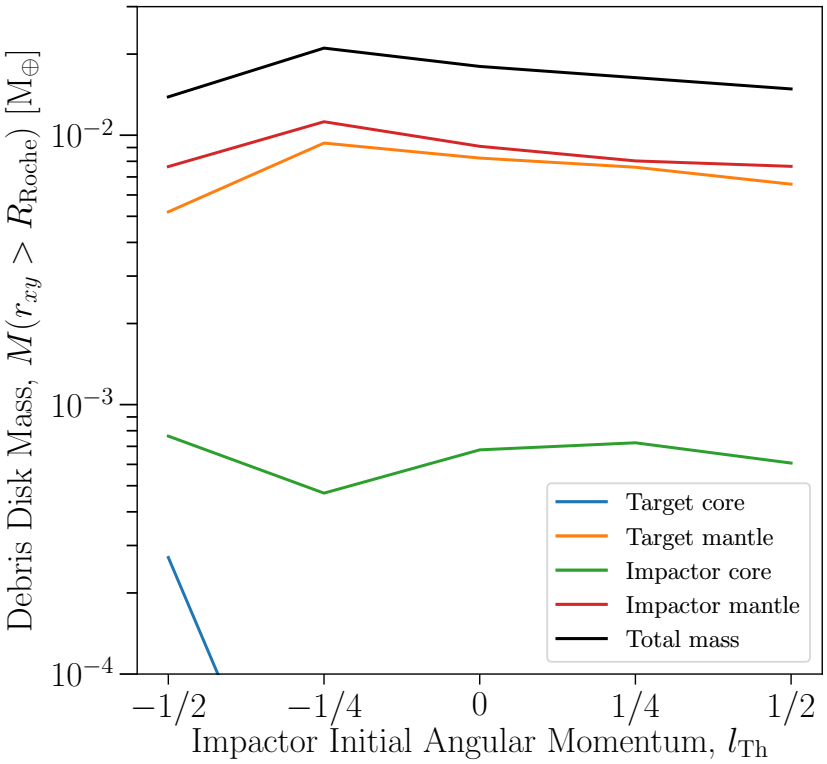

Figure 2.9: Total bound mass, excluding clumps, outside a cylinder with the Roche radius centred on the post-impact Earth, as a function of Theia's initial spin angular momentum. The different colours represent the different material components as described in the legend. All results are at a simulation time of 100 hours.

to the initial spin of Theia, because both counter-rotating impactor scenarios end in mergers and the rapidly corotating Theia produces a hit-and-run collision. In order of increasing $l_{\rm Th}$, the final gravitationally bound mass is 0.988, 0.987, 0.987, 0.985, and 0.955 $M_\oplus$ out of the total of 1.020 $M_\oplus$. The corresponding total angular momenta, in units of $L_{\rm EM}$, evolve as follows: $1.17 \rightarrow 1.17, 1.21 \rightarrow 1.19, 1.25 \rightarrow 1.21, 1.28 \rightarrow 1.23$ and $1.32 \rightarrow 0.78$. In the $l_{\rm Th} = \frac{1}{2}$ case, the largest of the many escaping clumps has a mass of 0.0076 $M_\oplus$, is taking away 0.047 $L_{\rm EM}$ of the angular momentum and is 53.5 $R_\oplus$ away from Earth at 40 hours, beyond the edge of the region shown in the lower right-hand panel of Figure 2.7.

The clumps left orbiting the Earth after impact in the simulations with $l_{\rm Th} = 0$ and $\frac{1}{4}$ have masses of 0.010 and 0.020 $M_\oplus$ respectively – 0.813 and 1.626 times the mass of the present-day Moon. Their orbits have periods of 40 and 120 hours, eccentricities of 0.6 and 0.8, periapses of ~ 4.6 $R_\oplus$ and 2.8 $R_\oplus$, and spin periods of 10 and 40 hours respectively. The periapse of the $l_{\rm Th} = 0$ clump is well outside the Roche radius, so this proto-Moon, while enduring tidal distortion as shown in Figure 2.7,

should survive. For the $l_{\rm Th} = \frac{1}{4}$ clump, the periapse lies just within the Roche radius of 3 $R_\oplus$, but if the orbit circularises in the same way as can be seen for the $l_{\rm Th} = 0$ proto-Moon, then this may enable a portion of it also to survive as a coherent proto-Moon.

The orbiting clump is resolved with over 10^5 particles in the $l_{\rm Th} = 0$ and $\frac{1}{4}$ simulations, allowing us to study in detail its composition. Both clumps have $\sim 29\%$ of their mass coming from the proto-Earth's mantle, $\sim 1\%$ from Theia's iron core, and the remaining $\sim 70\%$ from Theia's mantle. No iron was present in the long-lived clumps found in the study of Canup (2004). This may be the result of small differences in the impact scenarios or simulation details, but the similarity between our two different clump iron core mass fractions is striking, particularly given that the iron core of the Moon itself has been inferred to be 1–2% of the Moon's total mass (Viswanathan et al., 2019).

Figure 2.8 shows how the mass fraction of proto-Earth increases linearly towards the surface of the clump. The fractional distance from centre to surface is computed using an ellipsoidal surface defined by the inertia tensor to account for the tidal distortion of the $l_{\rm Th} = 0$ proto-Moon. Roughly equal amounts of Theia and proto-Earth are found at the surface of the clump; quite different from the overall 70/30 split. The results for the clumps in the $l_{\rm Th} = 0$ and $\frac{1}{4}$ simulations continue to be very similar. This distribution of material is primarily a result of the geometry of the impact and how the central part of the proto-Moon originates from a reasonably coherent chunk of Theia that remains self-bound throughout the impact. Any long-term evolution of this distribution over time, due to convection and other mixing mechanisms, is not considered here. However, if subsequent mixing between proto-Earth and Theia material were incomplete, then this radial variation could establish a relation between the isotopic difference between these two bodies, and that measured between the Earth and Moon. The challenge of interpreting oxygen isotope data means that there is an ongoing debate as to whether the isotopic compositions of lunar samples and the Earth are indistinguishable (Young et al., 2016) or not (Herwartz et al., 2014; Greenwood et al., 2018; Cano et al., 2020).

Outside the Roche radius, in addition to any large clumps there is a diffuse debris disk produced in each of our five simulations. The composition of these disks is shown in Figure 2.9, split by material and provenance. There is more mass in the debris disk than in resolved orbiting clumps in the two counter-rotating scenarios, with a more massive disk being formed by the impact with the less rapidly counter-rotating Theia. For the disks formed in the $l_{\rm Th} = 0$ and $\frac{1}{4}$ simulations, the overall bound mass exterior to the Roche radius grows with increasing $l_{\rm Th}$. However, the balance shifts from having a more massive disk to a more massive clump such that

the disk mass decreases with increasing $l_{\rm Th}$ in this regime. As the clump, or at least its centre, is rich in Theia, the debris disk becomes less dominated by Theia, with almost equal amounts of target and impactor mantle when $l_{\rm Th} = \frac{1}{4}$. Thus, the disk material that may subsequently be accreted by the orbiting clump has a composition that is very similar to that already present at the surface of the clump.

When performing the same simulations with 10^6 particles we find the outcomes to be significantly different to those presented here for the simulations containing 10^7 particles. For instance, the simulation with $l_{\rm Th} = 0$ does not yield an orbiting clump; instead it creates a merger similar to the $l_{\rm Th} = -\frac{1}{4}$ and $l_{\rm Th} = -\frac{1}{2}$ simulations. Also, while the composition of the mass in bound orbits exterior to the Roche radius is robust to this change in numerical resolution, the amount of this material is $\sim 45\%$ larger in the higher resolution case. A summary of the properties of the debris disks and the resulting orbiting satellites is shown in Table 2.2.

2.5 Conclusions

We have presented a method to compute the hydrostatic equilibrium state of a uniformly rotating compressible fluid object, described as a set of concentric oblate spheroids, each with constant density (§2.2.1). We then described an adaptation of the SEAGen algorithm of Kegerreis et al. (2019) that places particles to match precisely this equilibrium configuration (§2.2.2). The combination of these two tasks is performed by our new, open-source code WoMa, implemented in python and publicly available at `https://github.com/srbonilla/WoMa` and the python module `woma` can be installed directly with pip. We tested its capabilities using simulations containing up to just over 10^9 SPH particles that were evolved with the SWIFT code. Relative to previous studies that make particle-based models of rotating planets by incrementally adding rotation between repeated relaxation simulations, our method has the advantages of being fast and of allowing precise control over the structure of the rotating planet to be simulated.

We used this new technique to study the effect of different rotation rates of Theia in 10^7-particle simulations of a canonical Moon-forming impact. Counter-rotating Theia's produced quick mergers, whereas a rapidly corotating Theia led to a hit-and-run collision with numerous unbound clumps escaping from the Earth. In the zero spin and slowly corotating Theia cases, a large clump was left orbiting the Earth after 100 hours. The mass and composition of the resulting debris disk also varies systematically with the initial spin of Theia. Our findings confirm previous results, using lower resolution studies, that the outcomes of planetary giant impacts

Table 2.2: Properties of the resulting debris disk and orbiting satellite for our suite of simulations.

l	$-1/2$		$-1/4$		0		1/4		1/2	
$N_{\rm p}$	10^6	10^7	10^6	10^7	10^6	10^7	10^6	10^7	10^6	10^7
Debris disk total mass [$M_\oplus$]	0.010	0.014	0.013	0.021	0.011	0.018	0.005	0.016	0.005	0.015
Debris disk target core fraction	0.01	0.02	< 0.01	< 0.01	< 0.01	< 0.01	< 0.01	< 0.01	< 0.01	< 0.01
Debris disk target mantle fraction	0.40	0.37	0.43	0.44	0.46	0.45	0.47	0.46	0.42	0.44
Debris disk Theia core fraction	0.05	0.06	0.03	0.02	0.02	0.04	0.03	0.04	0.04	0.04
Debris disk Theia mantle fraction	0.53	0.55	0.54	0.53	0.51	0.51	0.49	0.49	0.54	0.52
Orbiting clump total mass [$M_\oplus$]	-	-	-	-	0.002	0.010	0.020	0.020	-	-

can depend strongly on the initial spins of the colliding bodies. Therefore, N-body simulations that aim to trace the formation of terrestrial planetary systems using models for the aftermath of giant impacts should track the spin of the forming planets.

The simulation with Theia not spinning initially yields an orbiting proto-Moon with a periapse at 4.5 $R_\oplus$, well outside the Roche radius of $\sim$ 3 $R_\oplus$. It has a mass of 0.01 $M_\oplus \simeq$ 0.81 $M_\leftmoon$, of which $\sim$1% is an iron core, and while its overall fraction of proto-Earth material is only 30%, a radial gradient in material provenance means that $\sim$50% of the surface material originates in the proto-Earth. This fraction is similar to that in the Roche-exterior debris disk surrounding the Earth. Compared with previous studies of the canonical impact, which typically found a proto-Earth fraction of only $\sim$30% in the potential Moon-forming material, our value is higher because some of Theia is already hidden deep within the proto-Moon. These shared characteristics suggest that this proto-Moon might be a plausible route for forming the Moon.

We also find that the results from our Moon-forming giant impact simulations can be sensitive to numerical resolution, with the collision outcome changing in one out of the five scenarios when increasing the particle number from 10^6 to 10^7. However, while the results presented here have not demonstrated numerical convergence, they do use more particles than has been typical in studies of the Moon-forming impact. Higher resolution simulations show clearer numerical convergence for the formation of similar clumps (Kegerreis et al., 2022, submitted).

There are also untested uncertainties associated with: the formulation of SPH being used, where small-scale artificial clumping could arise as a consequence of discontinuities in the density field and the level of material mixing will also be affected (which we will study in the next chapter); and the choice of EoS, which will influence the detailed structure of the debris disk and the depletion of volatile elements accreting onto the proto-Moon. (Kegerreis et al., 2022, submitted) investigated a larger volume of parameter space for the impact scenario to determine how common these orbiting proto-Moons are.

Chapter 3

Density discontinuities in planetary SPH

Density discontinuities cannot be precisely modelled in standard formulations of SPH because the density field is defined smoothly as a kernel-weighted sum of neighbouring particle masses. This is a problem when performing simulations of giant impacts between proto-planets, for example, because planets typically do have density discontinuities both at their surfaces and at any internal boundaries between different materials. The inappropriate densities in these regions create artificial forces that effectively suppress mixing between particles of different material and, as a consequence, this problem introduces a key unknown systematic error into studies that rely on SPH simulations. In this chapter we present a novel, computationally cheap method that deals simultaneously with both of these types of density discontinuity in SPH simulations. We perform standard hydrodynamical tests and several example giant impact simulations, and compare the results with standard SPH. In a simulated Moon-forming impact using 10^7 particles, the improved treatment at boundaries affects at least 30% of the particles at some point during the simulation.

3.1 Introduction

A key chapter in the solar system's history involves impacts between planet-sized objects. This giant impact phase of planet formation is responsible for many of the features we see today in our solar system. To name a few: the formation of our Moon (e.g. Hartmann et al., 1975; Cameron & Ward, 1976; Benz et al., 1987), the tilted spin axis of Uranus (e.g. Slattery et al., 1992; Kegerreis et al., 2018; Reinhardt et al., 2020), the formation of the Pluto-Charon system (e.g. McKinnon, 1984, 1989; Canup, 2005), the Mars hemispheric dichotomy (e.g. Wilhelms & Squyres, 1984), or the origin of Mercury's high core:mantle ratio (e.g. Benz et al., 1988; Chau et al., 2018).

An ideal tool for studying giant impacts is smoothed particle hydrodynamics (SPH). SPH is a particle-based method used in a wide range of astrophysical and engineering topics (Springel, 2010; Monaghan, 2012). It is the most commonly used option for studying giant impacts because of the complexity and anisotropy of these highly non-linear interactions. Compared with grid-based hydrodynamical codes, SPH has the advantages of naturally following the provenance of material and being readily combined with efficient gravity solvers.

Despite its many positive points, the hydrodynamical part of SPH can still have difficulties treating the mixing of particles that represent different materials. In the standard density-energy formulation of SPH, density discontinuities cannot be accurately represented because of the smoothing inherent in the definition of the density field. However, density profiles of differentiated planets do have discontinuities, typically both between different material layers (e.g. core to mantle boundary) and the outer surface. The standard SPH formulation creates artificial forces that act like an effective surface tension at these discontinuities, repelling one material from the other and suppressing mixing between different materials. While the cause of this numerical artefact is clear, the consequences for the mixing of materials during giant impact simulations are rarely considered (e.g. Deng et al., 2019a,b, who compared SPH with another Lagrangian method). As such, this represents a significant and unquantified systematic uncertainty for standard simulations. This numerical issue could be crucial in the modelling of many giant impact problems, with examples being how much mixing would have been provoked in the core of Jupiter by a giant impact (Liu et al., 2019), and what the distribution of iron is in the debris of the hypothesised Moon-forming impact (Canup & Asphaug, 2001; Ruiz-Bonilla et al., 2021).

Previous studies that have addressed the smoothing of density discontinuities in a planetary context by modifying the SPH formulation have dealt either with those arising from contact between two different materials at the same pressure (Woolfson, 2007; Reinhardt et al., 2020) or with that found at the surface of a planet (Reinhardt & Stadel, 2017). In this chapter we propose a novel, computationally cheap method to suppress the spurious numerical effects associated with density discontinuities, regardless of their context.

In §3.2, we describe the basics of SPH (§3.2.1), the details of the density discontinuity problem we aim to solve and previous attempts (§3.2.2), and finally our own method (§3.2.3). In §3.3, we perform some standard hydrodynamical tests (§3.3.1, §3.3.2), as well as testing a settling simulation of a planet (§3.3.3), and a variety of giant impacts between a proto-Earth and Theia with and without our method (§3.3.4) to search for differences. Finally, conclusions are presented in §3.4.

3.2 Methods

3.2.1 Background theory

The fundamental idea of SPH is to reconstruct a density field from a set of discrete particles with masses m_i. As mentioned in §1.2.1, the density ρ at any point in space $\vec{r}$ is computed as a weighted sum of the masses of the neighbouring particles (Monaghan, 1992) via

$$\rho(\vec{r}) = \sum_{j=1}^{N_{\text{ngb}}} m_j W(\vec{r} - \vec{r}_j, h), \tag{3.2.1}$$

where W is the kernel function, which is a function of position, and h is the smoothing length. We will be referring to the density of particle i as $\rho_i \equiv \rho(\vec{r}_i)$, where $\vec{r}_i$ is the position of particle i.

Once the densities are computed, we can use the intrinsic specific internal energy u_i of a particle (or any other thermodynamic variable), and the equation of state assigned to it (EoS, i) to compute the pressure at the location of each particle via $P_i \equiv P_{\text{EoS},i}(\rho_i, u_i)$.

At this point we can compute the hydrodynamical forces using

$$F = \frac{\nabla P}{\rho} = \nabla\left(\frac{P}{\rho}\right) + \frac{P}{\rho^2}\nabla\rho. \tag{3.2.2}$$

Then, we can discretize the acceleration of each particle

$$\vec{a}_i = -\sum_{j=1}^{N_{\text{ngb}}} m_j \left(\frac{P_j}{\rho_j^2} + \frac{P_i}{\rho_i^2}\right) \nabla_i W_{ij}, \tag{3.2.3}$$

where $W_{ij} \equiv W(\vec{r}_i - \vec{r}_j, h_i)$. This formula was first derived using a discrete form of the action principle for an adiabatic fluid. The rate of change in internal energy for particle i can be expressed as

$$\frac{du_i}{dt} = \frac{1}{2}\sum_{j=1}^{N_{\text{ngb}}} m_j \left(\frac{P_j}{\rho_j^2} + \frac{P_i}{\rho_i^2}\right) \vec{v}_{ij} \cdot \nabla_i W_{ij}, \tag{3.2.4}$$

where $\vec{v}_{ij} = \vec{v}_i - \vec{v}_j$. We will be referring to these two formulae above as the standard SPH equations of motion.

This is not the only choice of discretization that can be used. We will now briefly summarize the geometric density average force (GDF) method (Wadsley et al., 2017), ignoring artificial viscosity terms:

$$\vec{a}_i = -\sum_{j=1}^{N_{\text{ngb}}} m_j \left(\frac{P_i + P_j}{\rho_i \rho_j}\right) \nabla_i \bar{W}_{ij}, \tag{3.2.5}$$

$$\frac{du_i}{dt} = \sum_{j=1}^{N_{\rm ngb}} m_j \left(\frac{P_i}{\rho_i \rho_j}\right) \vec{v}_{ij} \cdot \nabla_i \bar{W}_{ij}. \tag{3.2.6}$$

It is worth noting that these equations come from a general form of Equation 3.2.2 presented already by Monaghan (1992),

$$\frac{\nabla P}{\rho} = \frac{P}{\rho^\sigma} \nabla \left(\frac{1}{\rho^{1-\sigma}}\right) + \frac{1}{\rho^{2-\sigma}} \nabla \left(\frac{P}{\rho^{\sigma-1}}\right), \tag{3.2.7}$$

with $\sigma = 1$. This choice was made in order to minimize errors in the vicinity of strong density gradients. In addition to this choice, the GDF method also requires a symmetric gradient of the kernel, in order to have symmetrized force terms, namely

$$\nabla_i \bar{W}_{ij} = \frac{1}{2} f_i \nabla_i W(\vec{r}_{ij}, h_j) + \frac{1}{2} f_j \nabla_j W(\vec{r}_{ij}, h_j), \tag{3.2.8}$$

where

$$f_i = \sum_{j=1}^{N_{\rm ngb}} \frac{m_j}{\rho_i} r_{ij}^2 W'\left(\frac{r_{ij}}{h_i}\right) \Bigg/ \sum_{j=1}^{N_{\rm ngb}} \frac{m_j}{\rho_j} r_{ij}^2 W'\left(\frac{r_{ij}}{h_i}\right), \tag{3.2.9}$$

and $r_{ij} = |\vec{r}_i - \vec{r}_j|$, $W(\vec{r}_i - \vec{r}_j, h_i) = \frac{1}{h_i^3} W\left(\frac{r_{ij}}{h_i}\right)$, $W'(q) = \frac{1}{q}\frac{dW}{dq}$.
This formulation of SPH minimizes surface tension effects in multiphase flows, which can be a desirable feature for planetary SPH simulations where the mixing between materials is key to some problems.

Wadsley et al. (2017) chose to use Wendland (1995) kernels over the traditional cubic spline kernel (Monaghan, 1992) because they do not suffer from the pairing instability (Dehnen & Aly, 2012), which can lead to particles forming close pairs reducing the effective neighbour number. However the GDF method itself does not require a specific kernel. Hence we will use the traditional cubic spline kernel in this work when comparing different flavours of SPH, for simplicity.

An important characteristic of planetary SPH simulations is the choice of materials, or in other words, equations of state (EoS). Each particle is labeled as being a particular material and, whenever needed, its equation of state is applied to compute its pressure. One well known and widely used option is the Tillotson (1962) EoS. This analytical EoS was originally developed to model hypervelocity impacts, partly motivated by nuclear weapons research. Each material (e.g. iron, granite, etc.) is described by ten parameters and three common analytical expressions describing a compressed or cold state, a hot and expanded state, and a hybrid state. As mentioned, this option is widely used for its simplicity but it has significant limitations. Materials described by the Tillotson EoS lack phase transitions, as well as not being suitable for giant impact simulations where vaporization plays an important role (Stewart

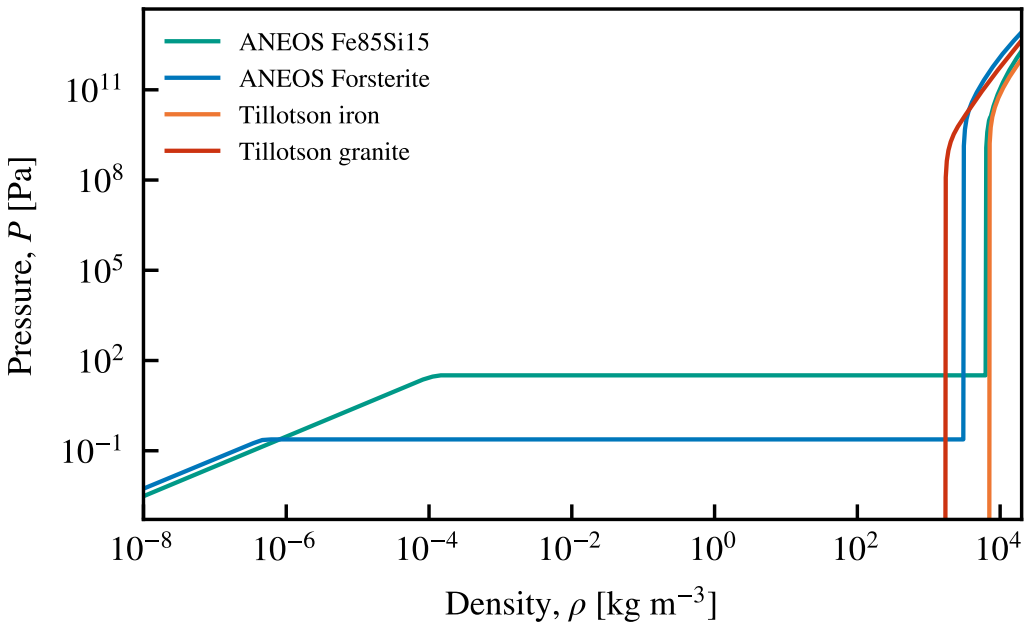

Figure 3.1: Pressure as a function of density at a fixed temperature, $T = 2000$ K, for different materials commonly used in planetary SPH simulations. Horizontal segments represent the phase transitions between liquid and gas that are present only for more sophisticated equations of state like ANEOS.

et al., 2020). One example of a more modern approach is to use the ANEOS EoS (Thompson, 1970; Melosh, 2007; Stewart et al., 2020). This EoS model is described by the Helmholtz free energies for solid, liquid, vapor, plasma and mixed phases. It is capable of covering a large range of pressures, densities, and temperatures, which is important for simulating giant impacts between proto-planets. ANEOS EoS have over 40 input parameters, and multiple phase transitions are present for any material. The presence or absence of phase transitions in the EoS used for the simulations, as shown in Figure 3.1, will have a key role when designing a method to solve our density discontinuity problem, as described in §3.2.2.1.

In this work we will use the open-source hydrodynamics and gravity code SWIFT (SPH With Inter-dependent Fine-grained Tasking; www.swiftsim.com, Schaller et al., 2016; Kegerreis et al., 2019). SWIFT has been designed from scratch to run large simulations and scale well on shared/distributed-memory architectures. SWIFT runs over 30 times faster than Gadget-2 on representative cosmological problems (Borrow et al., 2018), and has enabled planetary impact simulations with 100-1000 times more particles than was previously typical. This speed is partly a result of SWIFT's task-based approach to parallelism and domain decomposition for the gravity and SPH calculations (Gonnet, 2015).

3.2.2 Problems in Planetary SPH

Given the definition of the density field in SPH (eq. (1.2.1)), a direct consequence is that the density varies smoothly in space, which makes density discontinuities difficult to represent. However, differentiated planets in hydrostatic equilibrium can and should contain density discontinuities both where there is a change of material (e.g. the core to mantle boundary) and at the surface of the planet.

When trying to represent a planet in SPH simulations, the smoothing of SPH particle densities across these discontinuities gives rise to well known problems (Woolfson, 2007), with poorly quantified consequences. The incorrect pressures induced by the smoothed densities in these regions effectively create an artificial force that repels different material layers from each other. In the case of the free surface, particles in the outermost regions of the planet will have their densities underestimated. This will subsequently lead to underestimated pressures that will accelerate the system away from the desired equilibrium configuration. We illustrate the initial problems using a Theia-like body, with mass $M = 0.133$ $\mathrm{M}_{\oplus}$, in Figure 3.2. The analytical profile and particle placement for this, and all examples in this chapter, have been produced by the open-source code WoMa (Ruiz-Bonilla et al., 2021), which uses the SEAGen method (Kegerreis et al., 2019) to make particle realisations of planets. Note that the artificial effective surface tension is equally present for both the standard and GDF flavours of SPH, because it arises from the definition of the density field, which is common to both methods.

3.2.2.1 Density discontinuities between different material layers

Previous studies have attempted to address the issue of density discontinuities between different materials by changing the formulation of SPH (Price, 2008; Hosono et al., 2016). Woolfson (2007) and later Reinhardt et al. (2020) proposed solutions based on computing correction factors, f_{ij}, for the SPH density, which was corrected via

$$\begin{aligned} \rho_i &= \sum_{j=1}^{N_{\mathrm{ngb}}} f_{ij} m_j W_{ij}, \\ f_{ij} &= \frac{\rho_{\mathrm{EoS},i}(P,T)}{\rho_{\mathrm{EoS},j}(P,T)}. \end{aligned} \tag{3.2.10}$$

The density of particle i is calculated with the inclusion of the correction factor, which varies for each neighbouring particle j. The correction factors represent the ratio of densities that particle i would have at pressure P and temperature T if it were made from material i versus material j. Thus, if neighbour j is the same

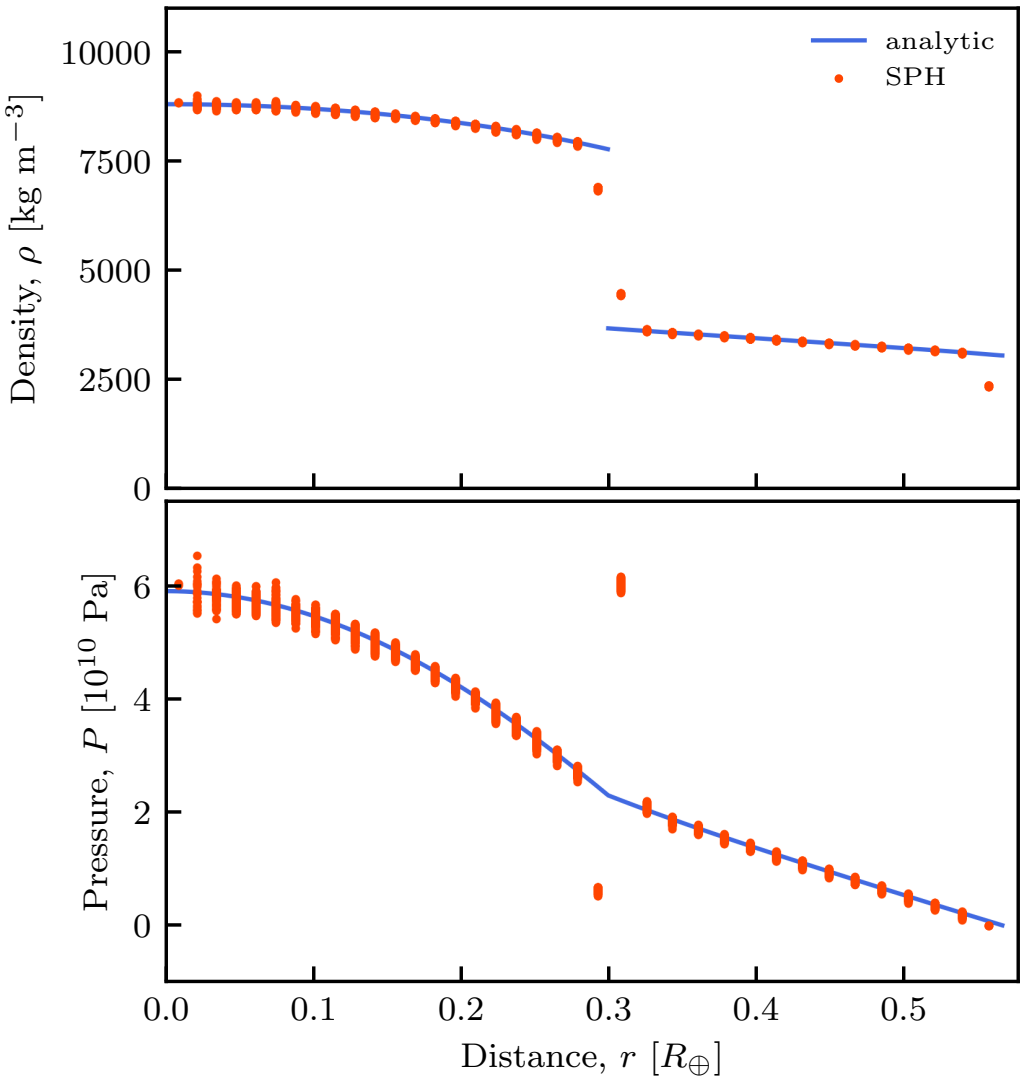

Figure 3.2: Initial density (upper panel) and pressure (lower panel) profiles of a spherical Theia-like planet, $M = 0.133$ $M_\oplus$, using standard SPH density calculations. The core:mantle mass ratio is 30:70, and the temperature at the surface of the planet is 2000 K with an adiabatic entropy profile. A total of 10^5 particles are used to represent the planetary body. The smoothing in the density field introduces spurious pressures at the material boundary and, to a lesser extent, the edge of the planet.

material as particle i, then $f_{ij} = f_{ji} = 1$. Woolfson (2007) applied this modification to equilibrium models of planets, where the temperature and pressure vary smoothly with radius. Reinhardt et al. (2020) suggested using the kernel-averaged temperature and pressure as better estimates to account for dynamical evolution of the system during a giant impact simulation.

This approach can reduce the problem, especially for stationary planets, but has a couple of inconvenient drawbacks. The first is that, computationally, it requires three loops over all particles to compute the density, compared with the single loop used in the standard density definition: the first loop is used to compute the standard SPH density, the second one to compute the kernel averages of temperature and pressure, and the third one to recompute the density using Equation 3.2.10. In addition to these, there is a final fourth loop to compute the hydrodynamical forces using Equation 3.2.3, Equation 3.2.4 for standard SPH or Equation 3.2.5, Equation 3.2.6 for GDF. The second and more serious downside appears when using more sophisticated equations of state like ANEOS. As shown in Figure 3.1, for the same temperature and pressure, two materials could have different densities by many orders of magnitude. For example, at 10 Pa and 2000 K, the density ratio between Tillotson iron and granite is 0.2, but between ANEOS $Fe_{85}Si_{15}$ and forsterite is 9.5×10^7. This occurs because one material (in this case $Fe_{85}Si_{15}$) has undergone vaporization whereas the other (forsterite) has not. When computing the final density using Equation 3.2.10, the f_{ij} factors could produce hugely unrealistic densities if particle i has a significant number of neighbours j of a different material. This issue would not only affect the density estimation of a few particles and hence the evolution of the system, but the high densities will also yield high pressures and hence forces that will dramatically decrease the value of the time step needed to continue evolving the simulation. Reinhardt et al. (2020) do not perform any correction if a particle has a density below an empirically determined threshold, in order to avoid this problem (private communication).

3.2.2.2 The free surface problem

Reinhardt & Stadel (2017) also proposed a solution, distinct from those described above, to the problem of the density discontinuity present at the surface of any planet. Their approach consisted of defining a statistic

$$f_i = \frac{\left| \sum_{j=1}^{N_{\text{ngb}}} (\vec{r}_j - \vec{r}_i)\, m_j W_{ij} \right|}{2h_i \sum_{j=1}^{N_{\text{ngb}}} m_j W_{ij}} \tag{3.2.11}$$

that is computed for every particle. The density of each particle is corrected by a factor that depends upon the value of this statistic, f_i, with the correction factor derived by assuming that the particle configuration involves a plane boundary between mass and vacuum in the kernel. This assumption may be appropriate to explain non-zero f_i values during a simulation of a planet in hydrostatic equilibrium. However, there could be different scenarios where this is not the case during a planetary impact SPH simulation, for instance a satellite being tidally disrupted into some distorted geometry. Thus a more general approach to correcting densities near the boundary with a vacuum is desirable.

3.2.3 Density corrections

Here we present our method to address both the material boundary and free surface problems at once. In addition, this method is relatively computationally cheap since it only uses one extra loop over all particles compared with the standard SPH density computation. We define a statistic that measures how afflicted a particle is by being close to a density discontinuity. The densities of these particles are then corrected in a smooth way using that same statistic.

The method can be summarized as two steps: first we identify problematic particles, then we fix their densities. Our first goal is to identify particles close to a material boundary or free surface. Our proposal, which is similar to that of Reinhardt & Stadel (2017), is

$$I_i = \alpha \frac{\left| \sum_{j=1}^{N_{\mathrm{ngb}}} \kappa_{ij} \left(\vec{r}_j - \vec{r}_i \right) m_j W_{ij} \right|}{h_i \sum_{j=1}^{N_{\mathrm{ngb}}} m_j W_{ij}}, \qquad \kappa_{ij} = \begin{cases} 1 & \text{if } i \text{ and } j \text{ are the same material,} \\ -1 & \text{if } i \text{ and } j \text{ are different material.} \end{cases} \tag{3.2.12}$$

where α is a dimensionless parameter whose value we discuss later. We will refer to I_i as the 'imbalance statistic' for particle i.

Particles sitting in the middle of a perfectly regular grid of the same material particles will have an imbalance statistic equal to zero, and this will be approximately the case for most of the particles in our initial planet in hydrostatic equilibrium. Particles sitting at the surface of a planet will have about half of their kernel filled with particles of the same material and the other half empty. Their imbalance statistics should be somewhat greater than zero and, for the choice of α we describe in due course, they will be of order unity. Similarly, for particles placed at the boundaries

between two materials, one half of their kernel is full of particles of the same material whereas the other hemisphere is full of particles of a different material; hence the inclusion of the minus sign in κ_{ij} to account for the contributions from particles of the other material and produce a comparable unity-order value for I_i.

Now that we have defined the imbalance statistic that locates the problematic particles, we need to correct their densities. First, we compute the standard SPH density using Equation 3.2.1, and the pressure, P_i, and temperature, T_i, for every particle using their corresponding equation of state with their density, ρ_i, and specific internal energy, u_i, which is used in the hydrodynamical simulation rather than the temperature. Then, assuming that pressure and temperature vary smoothly on the scale of the smoothing length everywhere within the simulation, we compute, for every particle, estimated values for their temperature and pressure via

$$\bar{T}_i = \frac{\sum_{j=1}^{N_{\text{ngb}}} T_j \mathrm{e}^{-I_j^2} W_{ij}}{\sum_{j=1}^{N_{\text{ngb}}} \mathrm{e}^{-I_j^2} W_{ij}}, \quad \bar{P}_i = \frac{\sum_{j=1}^{N_{\text{ngb}}} P_j \mathrm{e}^{-I_j^2} W_{ij}}{\sum_{j=1}^{N_{\text{ngb}}} \mathrm{e}^{-I_j^2} W_{ij}}. \tag{3.2.13}$$

These estimates represent pressures and temperatures averaged over neighbouring particles, weighted to favour nearby neighbours with low imbalance statistics. Recall that low imbalance statistic particles typically have neighbours sitting in regular grids, so those particles should be away from sharp density discontinuities and thus in regions where pressures and temperatures are computed accurately. In addition, we would like to have a smooth transition between the standard SPH computation and our modified one, such that the modification is only used when needed and without any sudden transitions. Hence we can define a pressure, $\widetilde{P}_i$, and temperature, $\widetilde{T}_i$, for every particle as

$$\begin{aligned} \widetilde{P}_i &= \mathrm{e}^{-I_i^2} P_i + (1 - \mathrm{e}^{-I_i^2}) \bar{P}_i, \\ \widetilde{T}_i &= \mathrm{e}^{-I_i^2} T_i + (1 - \mathrm{e}^{-I_i^2}) \bar{T}_i, \end{aligned} \tag{3.2.14}$$

such that the more problematic a particle is (the higher the imbalance statistic) the greater the contribution from the modified estimate. Now that we have estimated a corrected pressure and temperature for every particle, we use the corresponding equation of state to infer a corrected density for every particle via

$$\widetilde{\rho}_i = \rho_{\text{EoS},i}(\widetilde{T}_i, \widetilde{P}_i). \tag{3.2.15}$$

Finally, we compute a particle pressure based upon this corrected density and the unaffected specific internal energy, using $P_i = P_{\text{EoS},i}(\widetilde{\rho}_i, u_i)$. $\widetilde{\rho}_i$ and P_i are the values that are used in the equations of motion.

We determine the value of α with the following condition: a particle with a kernel that is half full of particles of the same material organized in a regular grid, and with the other half empty must have imbalance statistic equal to 1.5. We have chosen this value empirically, since an imbalance statistic of 1 has very little effect on the densities of particles one shell away from a different material, and a value of 2 significantly affects particles two shells away from a different material. This ensures particles at the surface of the planet and the material boundaries will have big enough imbalance statistics for the method to have a significant impact, without overcorrecting. This parameter may need to be adjusted if the kernel and/or the resolution parameter η (i.e. the number of neighbours within the kernel) is changed. Figure 3.3 shows the reduced imbalance statistic, I/α, for different kernels and numbers of neighbours. The minimum number of particles used to compute I/α is 6 ($(0,0,0)$, $(\pm1,0,0)$, $(0,\pm1,0)$, and $(0,0,-1)$). By making that grid finer we can compute it with 23, 76, 153, 298, and 519 particles. Finally we interpolate linearly to obtain the value of α that yields $I = 3/2$, depending on the desired number of neighbours.

This method only uses two loops over the neighbours of all particles. The first loop is used to compute the standard SPH density, pressure, and temperature, as well as the imbalance statistic for every particle; the second loop is used to evaluate Equation 3.2.13, which leads to the corrected density, $\widetilde{\rho}_i$, and final pressure. To illustrate how our method works, Figure 3.4 shows the imbalance statistic, the intermediate estimate of the pressure, and the final corrected density, for the same Theia-like planet that was shown in Figure 3.2. The imbalance statistic targets the right particles and the weighted and smoothed pressure estimate erases the pressure jump that is present for standard SPH. Finally, using the equation of state, we compute corrected densities that have values close to the analytical solution.

Figure 3.5 demonstrates the different calculations of density produced for one (identical) snapshot of a simulation by the three methods: standard SPH (Equation 3.2.1), the Reinhardt & Stadel (2017) method described in §3.2.2.1, and our method described above. The exact same particle configuration is used in all cases, a mid-collision snapshot of a giant impact between a proto-Earth and Theia, using ANEOS materials. The different densities produced by the three methods would lead to different subsequent evolution of these cases, if they were evolved forward from this common starting point using the different methods. The distinction between core and mantle material in the proto-Earth is quite diffuse in the standard SPH computation compared with the other two methods. The Reinhardt & Stadel (2017) method yields particles with densities over 10^5 kg m^{-3}, highlighted in red on the figure. This is due to the problem described in §3.2.2 when using equations of state

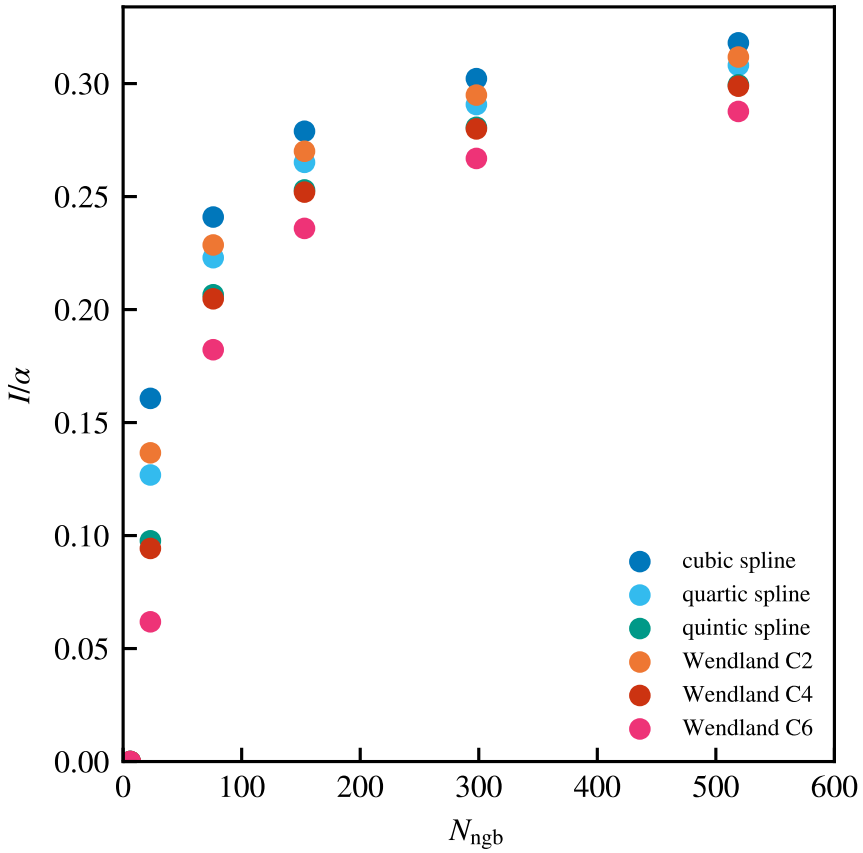

Figure 3.3: The scaled imbalance statistic, I/α (Equation 3.2.12), calculated at the centre of a sphere, only half of which is filled by particles in a regular cubic grid, as a function of the numbers of neighbours. This value is computed to normalize the value of the imbalance statistic so that it effects the first shell of particles at a density discontinuity, but not the rest. Different colours represent a variety of kernels, as detailed in the legend.

with phase boundaries like ANEOS. Finally, the iron particles scattered within the mantle of the proto-Earth are assigned significantly higher densities using the Reinhardt & Stadel (2017) method or our method than for standard SPH, and thus are more clearly visible in the figure. This is because their method acts whenever a particle has a neighbour of a different material, whereas in our method having a regular grid of particles of random materials will yield a density identical to the standard SPH one, up to the noise in the particle distribution for each material. Hence our method produces high densities for iron particles in the mantle when they have other iron particles as neighbours, but not when they are just surrounded by granite particles.

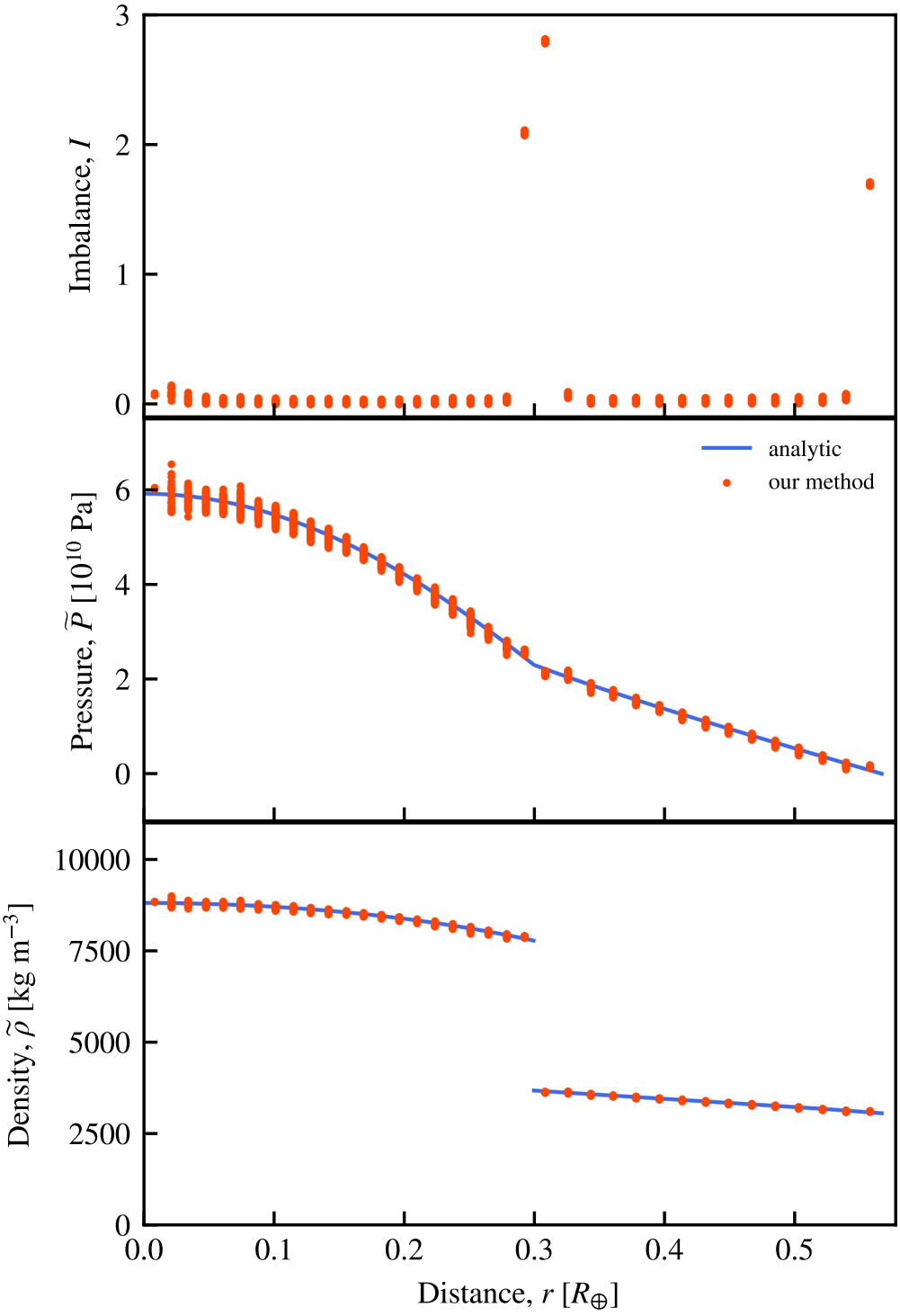

Figure 3.4: Imbalance statistic, I, estimated pressure from Equation 3.2.14, $\widetilde{P}$, and corrected density, $\widetilde{\rho}$, for the same spherical Theia-like planet, $M = 0.133$ M$_\oplus$, used in Figure 3.2.

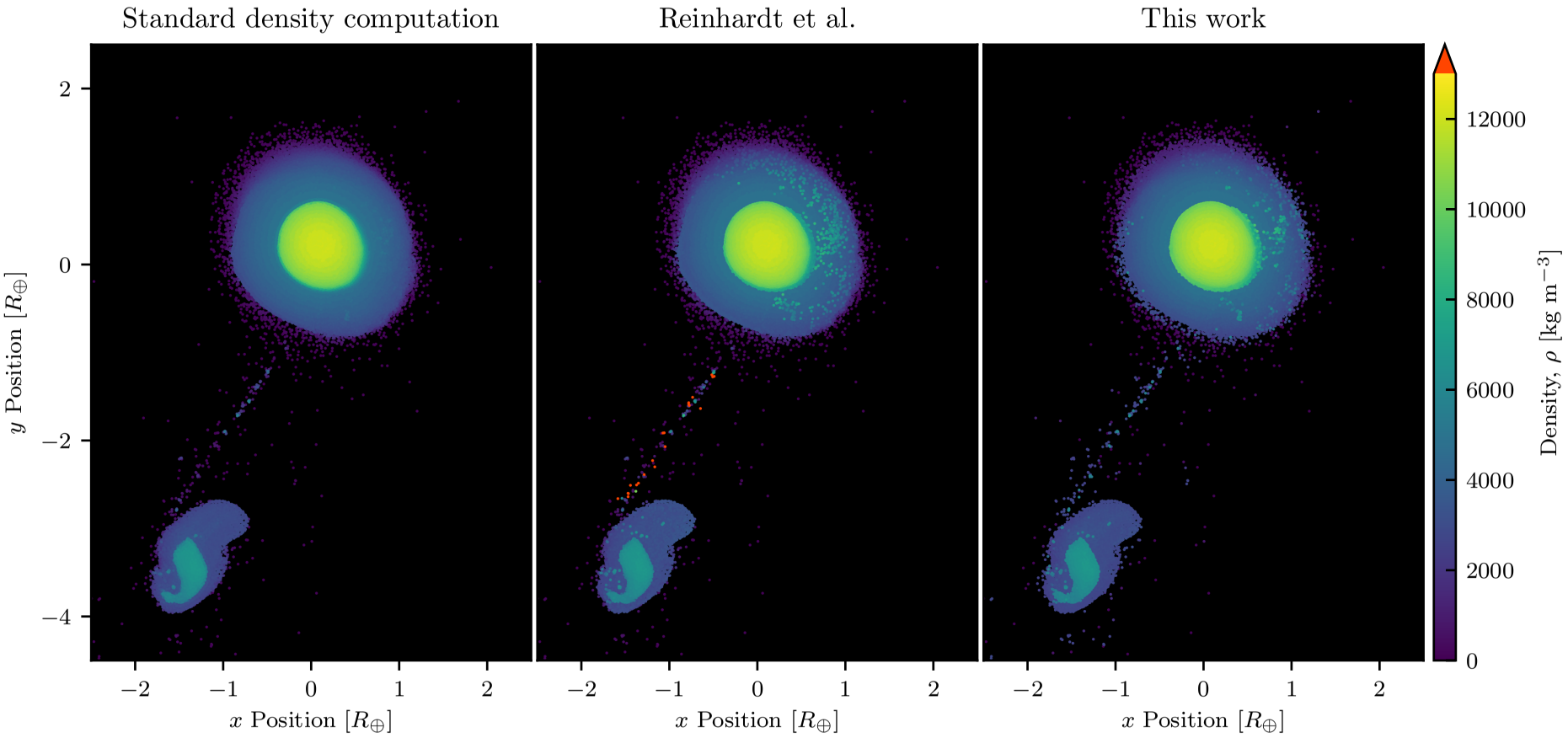

Figure 3.5: Different methods for computing the density for the exact same particle configuration, a mid-collision snapshot of a canonical impact using ANEOS materials. Higher density particles are plotted on top of lower density ones. Red particles are at least one order of magnitude higher in density than the maximum shown by the colour bar.

3.3 Tests and examples

Up to this point we have been using static distributions of particles to compare different ways to compute the density field in SPH simulations. Now we will perform some dynamic tests and example simulations combining these density estimators with the two different equations of motion that were presented in §3.2.1, standard SPH and GDF SPH (Wadsley et al., 2017).

3.3.1 2D Square Test

One of the most common tests of contact discontinuities is the square test (Saitoh & Makino, 2013; Deng et al., 2019a; Reinhardt et al., 2020). A 2D box of a certain material and density is surrounded by a medium of the same or different material at a different density in pressure equilibrium. If the code does not capture the density discontinuity correctly, then the pressure at the material interface becomes discontinuous. This creates an artificial tension, similar to that shown in Figure 3.2, which effectively acts to round the corners of the box.

For this test we use Tillotson (1962) materials, which are often used in planetary SPH simulations. The choice of EoS for this test should not be a sensitive one since all particles will have almost constant density throughout the whole test. The central square contains iron whereas the surroundings are composed of granite. The side length of the simulation box is $l_x = l_y = 0.5$ $R_\oplus$, and the depth of the box is $l_z = 0.001$ $R_\oplus$. This small thickness, together with periodic boundary conditions, allows densities to be computed in 3D despite particles being confined to 2D. The setup is designed such that the pressure everywhere is 10^{10} Pa and the temperature is 1000 K. These constraints dictate the mass (i.e. density) and internal energy of each particle, and result in a density jump from $\rho_{\text{granite}} = 3251$ kg m^{-3} to $\rho_{\text{iron}} = 7980$ kg m^{-3}. Iron particles, located in the inner square of side length $l_x/2$, are given a larger mass than granite ones such that the 2^{14} total particles in our simulations can be placed onto a regular square grid. Each simulation is evolved until 100 ks, which corresponds to roughly 300 sound crossing times of the central iron square.

We tested four different flavours of SPH: standard SPH; standard SPH with our method for improving densities; GDF (geometric density average force) SPH (Wadsley et al., 2017); and GDF SPH with our method. Adding our method on top of the standard SPH equations of motion has little effect on the overall evolution, so we will not discuss this combination for any of the tests in this chapter. Figure 3.6 shows the initial conditions and the result for the remaining three flavours of SPH following 100 ks of evolution. Relative to standard SPH, GDF SPH better maintains

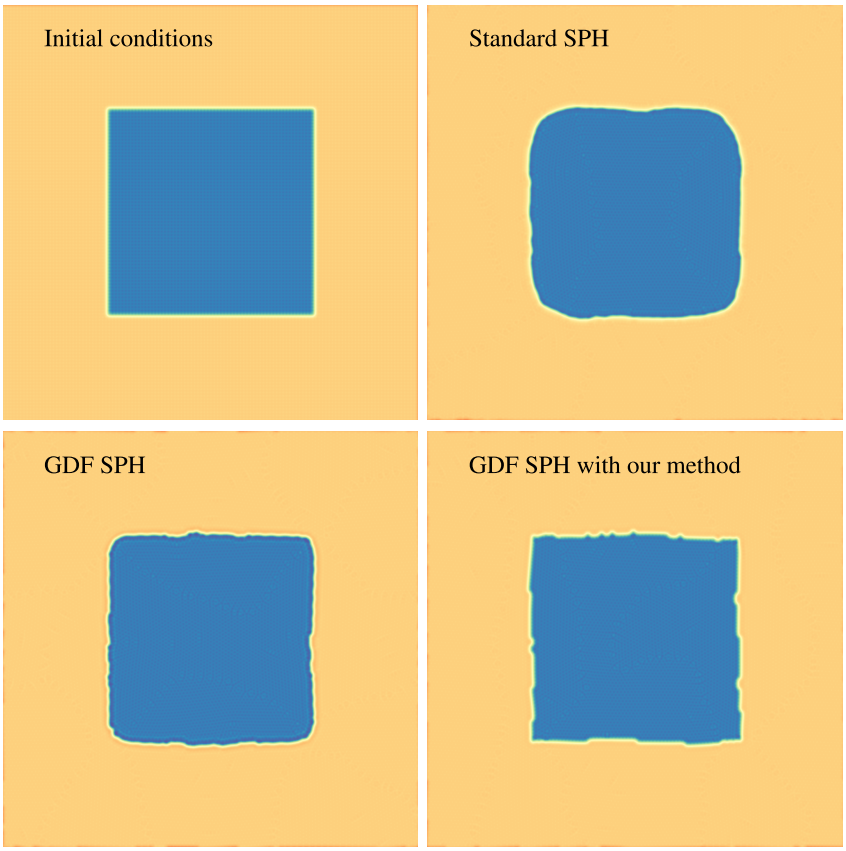

Figure 3.6: 2D Square test for 3 different flavours of SPH: standard SPH, GDF SPH, and GDF SPH with our method. Blue and orange represent higher and lower density values respectively. All panels, except for the initial conditions, show the result of the test after 100 ks, which corresponds to ∼300 sound crossing times of the central iron square.

the shape of the central square, and our method further improves the sharpness of the corners.

3.3.2 2D Kelvin-Helmholtz Test

The Kelvin-Helmholtz test is a common way to determine how well methods capture the instability that arises between adjacent fluids moving with different velocities. This is particularly relevant for giant impact simulations where velocity shear between different materials is common. This test does not have a known analytical solution, so we compare with different hydrodynamic codes, how our method handles the Kelvin–Helmholtz instability.

For this experiment we used the same box dimensions and materials as in the square test (§3.3.1). The pressure and temperature throughout the box were set to 10^{10} Pa

and 1000 K, and the number of particles on the x-axis for the low density material was $N = 256$. We chose all particles to have the same mass, so the denser layer contained $\sim$2.5 times more particles. The central strip of iron particles were given an initial x velocity of $v_x = 1000$ m s^{-1}, whereas the granite particles had $v_x = -1000$ m s^{-1}. An initial perturbation in the y velocity, $v_y = 20 \sin(4\pi x/R_\oplus)$ m s^{-1}, was introduced in order to seed the instability.

We observe that all three flavours of SPH create roll-like structures after 2500 s, as shown in Figure 3.7. At that time a particle travelling at the original x velocity will have traversed just over three quarters of the box length. We can see clear qualitative differences between all three flavours of simulation and, relative to the other two cases, GDF SPH with our method shows enhanced mixing between different material particles at the end of the swirls.

We tested the numerical convergence for a range of resolutions up to $N = 2048$ and calculated the time evolution of the maximum y-direction kinetic energy density and the amplitude of the y-velocity mode of the instability. All three flavours of simulation produced very similar shapes to the SPH code results shown by McNally et al. (2012). Using the smoothed y velocity field values, rather than the individual SPH particle values, made the maximum y-direction kinetic energy density grow slightly slower, but in neither case was the evolution in this statistic comparable with that found for grid codes (McNally et al., 2012). We conclude that our method does not converge significantly faster or slower than previous formulations of SPH for this particular test.

3.3.3 Planetary profiles after settling simulations

Prior to running a planetary giant impact simulation, a settling simulation is typically undertaken for every proto-planet. This is done in order to reduce any noise from the initial positions of the particles, as well as to obtain an object that is in hydrostatic equilibrium. Ideally the SPH densities, which are computed using the positions and masses of the particles, should match those obtained from solving the hydrostatic equilibrium equation. However, particle placement algorithms always introduce some perturbations and, as is the focus of this study, density discontinuities are not well captured with the traditional SPH density computation.

We consider a proto-Earth like planet, $M = 0.887\ M_\oplus$, made of an ANEOS $Fe_{85}Si_{15}$ core and forsterite mantle (Stewart et al., 2020) with a surface temperature of $T = 2000$ K and adiabatic temperature profile. The core:mantle mass ratio is 30:70. We use approximately 10^6 particles and let the simulation run for 20 ks, which is many times the sound crossing time of the planet.

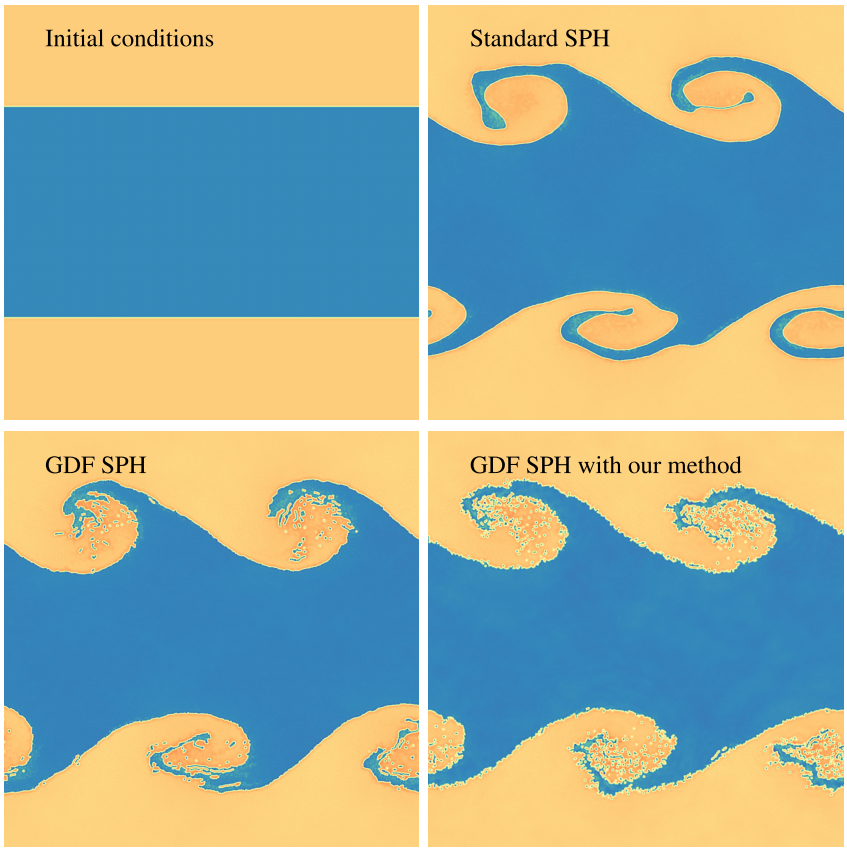

Figure 3.7: 2D Kelvin-Helmholtz test for 3 different flavours of SPH: standard SPH, GDF SPH, and GDF SPH with our method. Blue and orange represent Tillotson iron and granite respectively. All panels except that for the initial conditions show the result of the test after 2500 s.

Figure 3.8 shows the results for standard SPH, GDF SPH, and GDF SPH with our method. For standard SPH we see the evolved versions of the same issues that were highlighted for the initial particle arrangement in Figure 3.2. The density discontinuity in the material boundary is smoothed over, leading to a spurious jump in pressure across the boundary. Also, the underestimated density, and hence pressure, in the outermost shell of particles of the planet has decreased the radially outwards hydrodynamical force (see Equation 3.2.3). Consequently, the planet has contracted to find its numerical equilibrium, leaving it slightly smaller than desired.

For GDF SPH with the standard density computation, the situation is even worse because it does not even reach an equilibrium state. The density discontinuity is somewhat smoothed, although not quite as badly as in the standard SPH case. However, there is an additional problem whereby particles at the edge of the planet continually leak away; note the expanded horizontal scale for these panels. The reason for this is the factor f_i described in Equation 3.2.9. Consider the particles sitting at the edge of the main planet. Their neighbours are predominantly interior

with higher densities. These outermost particles will have underestimated densities because of the exterior vacuum increasing their smoothing lengths. However, this problem will not affect the interior particles, which will have densities that more accurately reflect the input profile. As a consequence, f_i will be inappropriately large for the outermost particles, producing an outward hydrodynamical acceleration (Equation 3.2.5) that exceeds the inward pull of gravity. Within two hours of simulation time, particles are already flying outwards. f_i can reach values of the order of 100, where the typical value should be around 1, and this effect gradually peels off more layers from the outer edge of the planet.

GDF SPH with our method solves the problems mentioned above, as illustrated in Figure 3.8. Not only is the density discontinuity well represented, which means that there is no jump in the pressure profile between the core and mantle, but the outer boundary also closely matches the analytical profile, meaning that the planet has the intended radius.

3.3.4 Giant impacts

In this section we compare features that occur during giant impacts between planets for different flavours of SPH. In §3.3.3 we saw that GDF SPH needs to be accompanied by our method in order to have stable planets, therefore we will just consider standard SPH, and GDF SPH with our method.

We use the proto-Earth and Theia described in §3.3.3 and §3.2.2, respectively, increase the number of particles by a factor of 10, and collide them with a range of impact angles and velocities. The total number of particles in our simulations is approximately 10^7, with all particles having the same mass.

We run three different impact scenarios, varying the angle of impact β and the impact velocity at contact v_c: a 'canonical' impact ($\beta = 45°$, $v_c = 1\ v_{esc}$), a faster low-angle impact ($\beta = 15°$, $v_c = 2\ v_{esc}$), and a hit-and-run grazing impact ($\beta = 65°$, $v_c = 1.5\ v_{esc}$). The mutual escape velocity of the system, assuming the two bodies are in contact and undeformed, is $v_{esc} = 9026$ m s^{-1}. Each impact is run four times using different random reorientations of the particle realizations of the planets. This provides an estimate of the stochastic noise and allows us more confidently to ascribe any observed differences to the different flavour of SPH being used. Depending upon just how chaotic the impact and its aftermath are, this can be an important consideration (Kegerreis et al., 2022, submitted).

We have now resolved the density discontinuity issues we previously had, and can thus be confident that these are not causing big unknown errors. Beyond the broad

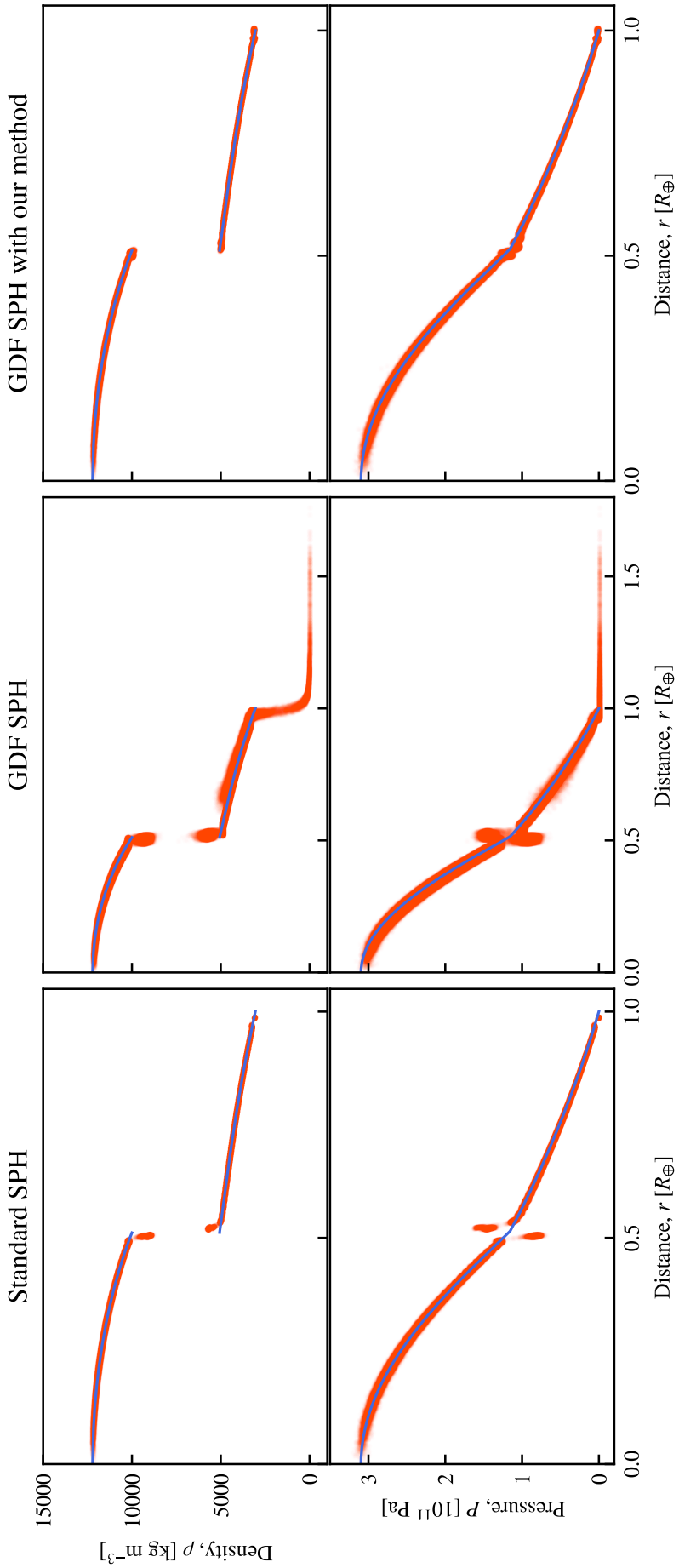

Figure 3.8: Density (top row) and pressure (bottom row) profiles after 20 ks of a settling simulation of a proto-Earth in hydrostatic equilibrium, for different flavours of SPH (different columns). The blue line represents the analytical profile, and red dots represent particles in the simulation. The central column, showing the GDF SPH results, has an expanded radial scale to show the extent to which particles are leaking away.

similarities, we observe some key differences between both flavours of SPH. These are common to all of the randomly reoriented resimulations and so appear to be robust differences between the standard SPH case and that with GDF SPH plus our method.

Changing between the two SPH flavours leads to significant differences in the distribution of post-impact iron in our low-angle collisions. The mass-fraction of iron in the debris beyond $3\,R_\oplus$ is $\sim 8\%$ using our flavour of SPH. This is about three times higher than the corresponding value for standard SPH. Within the final planet, the transition region between core and mantle, defined as the region where the relative iron content as a function of distance drops from 99% to 10%, is 0.12 $R_\oplus$ for standard SPH and 0.41 $R_\oplus$ for GDF SPH with our method. This demonstrates how mixing of materials can increase if the spurious boundary pressure gradients associated with standard SPH are suppressed using GDF SPH and our method. For both the canonical-like and hit-and-run impacts, the core of the target is barely disrupted by the impactor and the distribution of post-impact iron is insensitive to the flavour of SPH used.

In the initial conditions for our iron and rock bodies, the fraction of particles that have their densities badly mis-estimated by standard SPH as a result of their proximity either to a material boundary or the edge of the planet is $\sim 14\%$ for a 10^5-particle realisation. This drops to a still large $\sim 7\%$ with 10^6 particles, and $\sim 3\%$ for 10^7 particles. The fraction of particles that at some point during an impact simulation have $I > 1.5$, the value at the surface of a planet, is much larger. For 10^7-particle simulations, this fraction is 10%, 30%, and 70% for hit-and-run, 'canonical', and low-angle impacts respectively. The spurious density is often sufficiently wrong that the particle will be translated across a phase boundary in its EoS. In addition to producing spurious pressure, this will complicate efforts to track the thermal evolution of the material, both during the impact simulation and when providing inputs for subsequent long-timescale thermal evolution codes. This is relevant for material in the target and the resulting debris, be it a diffuse disk or in coherent clumps (Ruiz-Bonilla et al., 2021). The combination of GDF SPH with the method we have described here practically eliminates these problems that are present in standard SPH approaches, opening up the opportunity to use SPH planetary giant impact simulations for such studies reliably.

3.4 Conclusions

We have presented a novel method to compute the density field in smoothed particle hydrodynamics (SPH) simulations with particular reference to scenarios of planetary

giant impacts. It solves problems that arise in SPH for systems with sharp density discontinuities between different materials and between any material and a vacuum, with low computational cost. We combine this method with the geometric density average force (GDF) SPH (Wadsley et al., 2017) equations of motion because of their treatment that minimizes spurious numerical surface tension effects in multiphase flows. An implementation of our method is publicly available as an option in the open-source code SWIFT (Schaller et al., 2016).

This new method produces improved performance in the 2D square test with a better maintained square shape, and enhanced mixing between different material particles in the 2D Kelvin-Helmholtz test. Simulations of impacts between a proto-Earth and Theia, where the core of the Earth has been highly disrupted by the impactor, reveal a partially diffused iron core and a higher mass of iron in the debris disk. This method also prevents smoothed densities from placing particles into inappropriate places in their material phase diagram. As a consequence, the thermodynamic evolution of material can be tracked more realistically throughout an impact and its aftermath.

Chapter 4

Primordial misalignment of the proto-lunar disk

Long-term evolution models for the orbit of the Moon suggest the angle between the Earth's spin and the normal of the lunar orbital plane was $\sim 10^{\circ}$ at the time the Moon was formed (Goldreich, 1966; Touma & Wisdom, 1994). This prediction is inconsistent with models for the formation of the Moon that suggest a giant impact produced a debris disk in the equatorial plane of the Earth, and later the Moon was accreted at the Roche radius. Hence a different mechanism is needed in order to explain that primordial misalignment. In this chapter we show that giant impact simulations of the canonical Moon-forming impact with a sufficiently rapidly spinning proto-Earth can produce an inclined debris disk with respect to the post-impact Earth's spin. Furthermore, this angle is constant through timescales of days and, depending on the long-term tidal evolution, potentially could accrete a Moon with the desired primordial misalignment angle.

4.1 Introduction

In our solar system most planets orbit the Sun with close to circular orbits, and satellites orbit their host planets with various eccentricities and inclinations. This system can be considered low mass and the motion of these objects can be described using Newton's gravitational law, which depends on the mass distribution and position of the different bodies. This seemingly simple problem can turn quite difficult to solve accurately very rapidly. A planet is usually spinning, meaning its shape is not spherical and its gravitational potential will not be the simple formula for the spherical case. Moreover, its spinning rate can vary over time and consequently so can its shape and gravitational potential. If a planet has an ocean (water, magma, or anything that behaves like it) tides will also play a highly important role in its orbital evolution, generating gravitational resonances and interesting behaviours

(Touma & Wisdom, 1994), and even for solid bodies, gravitational tidal forces can be high enough that planets are not rigid. In addition, integrating such models for long timescales such as millions of years is a computational challenge. With all this complexity, it is not a surprise that orbital evolution is still an active field of research today.

The Earth–Moon system is quite unique in the Solar System. Earth is the only planet to have just one satellite, and the relative mass and angular momentum of the Moon are quite large when comparing with other planets and their satellites. In addition, the Earth and Moon seem to have a common origin when considering the low eccentricity of the Moon or by looking at the isotopic composition for some elements like oxygen (Wiechert et al., 2001; Young et al., 2016) in their respective mantles. That common origin is thought to be a giant impact between the proto-Earth and Theia 4.5 billion years ago (Cameron & Ward, 1976; Hartmann et al., 1975), and it would be the starting point of the orbital evolution of the Earth–Moon system. At that point in time we would expect to have a rapidly spinning Earth, a post-impact debris disk, and maybe a stable orbiting clump as shown in chapter 2.

In the canonical scenario for the formation of the Moon, the proto-Earth and Theia collide at around the mutual contact escape velocity with an impact angle of $\sim 45°$ (e.g. Cameron & Ward, 1976; Benz et al., 1987). The Moon subsequently accretes at the Roche radius, on a timescale of months (Kokubo et al., 2000) to hundreds of years (Salmon & Canup, 2012), from the debris disk that is formed surrounding the Earth following this impact. Some models for how the lunar inclination evolves with time trace it backwards from its present-day inclination to yield an inclination with respect to Earth's equator of $\sim 10°$ when the Moon accreted from the debris disk (Goldreich, 1966; Touma & Wisdom, 1994). When considering a Moon formed from a high angular momentum impact, this angle goes up to $\sim 50°$ (Ćuk et al., 2016) or even higher (Tian & Wisdom, 2020). However, traditional giant impact models suggest that the resulting debris disk should be near the equatorial plane of the Earth (Canup & Esposito, 1996; Ida et al., 1997; Ćuk & Stewart, 2012; Canup & Asphaug, 2001; Canup, 2012).

This has prompted attempts to explain the mutual inclination with mechanisms involving a gravitational resonance between the Moon and accretion-disk material (Ward & Canup, 2000). In this scenario, moonlets could not form within the Roche radius and it is the interaction between this inner disk and the proto-Moon accreted outside the Roche limit that could increase the inclination of the Moon up to 15°. This process would take place over timescales of 10^2 years. A second explanation for the origin of the inclination of the Moon's orbit is a pair of gravitational resonances between the Earth, the Moon, and the Sun called evection and eviction (Touma

& Wisdom, 1998; Rufu & Canup, 2020). At a semi-major axis of $a = 4.6R_\oplus$, the evection resonance increases the eccentricity of the orbit up to 0.5. This is a resonance between the rate of precession of the pericenter of the Moon and the mean motion of the Sun. After leaving the evection resonance the system encounters the eviction resonance at $a \simeq 6R_\oplus$. This is a resonance between the argument of the evection and the motion of the ascending node of the lunar orbit (the point where the lunar orbit intersects the ecliptic and the Moon moves into the northern ecliptic hemisphere) on the equator of the Earth. As a result, the mutual inclination is excited by 3°. Another explanation for the origin of the inclination of the Moon is the gravitational interactions of the Earth–Moon system with Earth-crossing planetesimals that were not yet accreted at the time of the Moon-forming event (Pahlevan & Morbidelli, 2015). A small quantity of mass between 0.0075 and 0.015 $M_\oplus$ carried by a few bodies, that later would be accreted to the Earth, could explain the current lunar orbit.

In this chapter we investigate whether a canonical-like giant impact scenario with a spinning proto-Earth can directly produce a misaligned debris disk with respect to the post-impact Earth's spin. We also briefly speculate whether that misalignment angle might persist long enough for a Moon to be accreted from the protolunar disk.

4.2 Methods

For this work we run high-resolution simulations with 10^6, $10^{6.5}$, and 10^7 particles using the smoothed particle hydrodynamics (SPH) code SWIFT with the improvements described in chapter 3 (www.swiftsim.com, Schaller et al., 2016) for a total simulation time of 100 ks (27.8 hours). For each simulation we fix: the mass of the proto-Earth, $M_{\rm pE} = 0.887\ M_\oplus$; the mass of Theia, $M_{\rm Th} = 0.133\ M_\oplus$; the velocity of impact, $v_{\rm imp} = v_{\rm esc}$; the angle of impact, $\beta = 45°$; the materials used, ANEOS Fe85Si15 for the cores and ANEOS forsterite (Stewart et al., 2020) for the mantles of both proto-planets; and finally the mass fraction of core:mantle, 30 : 70 again for both proto-planets. The surface temperature of both bodies is 2000 K following an adiabatic profile. All profiles and initial conditions have been done using the methods of chapter 2.

The orbital angular momentum of Theia is oriented in the $+\hat{z}$ direction, and we set the proto-Earth's spin rate to 5 different values in units of the angular momentum of the Earth–Moon system today: 0, 0.25, 0.50, 0.75, and 1.00 $L_{\rm EM}$. The non-zero values translate to periods of 14.2, 7.2, 5.1, and 4.0 hours respectively. We also choose the direction of the spin angular momentum to be orthogonal to the orbital

angular momentum of Theia in order to maximize any post-impact misalignment angle: $L_{\rm pE} \propto \hat{x}$ and $L_{\rm pE} \propto \hat{y}$, making a total of 9 simulations. Note that, for instance, $L_{\rm pE} \propto -\hat{x}$ has a mirror symmetry with respect to $L_{\rm pE} \propto \hat{x}$, for that reason we do not consider the $-\hat{x}$ and $-\hat{y}$ directions for the spin of the proto-Earth.

All simulations use cubic spline kernels and the resolution parameter η is set to 1.2348, which corresponds to approximately 48 neighbour particles for this kernel. The maximum smoothing length is chosen to balance computational speed of the code and a minimum-density cutoff used for tracking low density particles. A value of 0.1 $R_\oplus$ for our problem ensures only a small number of particles end up hitting the maximum smoothing length. The Courant number is 0.2, which translates to a timestep of order of 1 s for all resolutions considered in this study, and the gravitational softening length depends on the number of particles and is set to the minimum distance between particles in the initial conditions, which is the distance between particles at the centre of the proto-Earth where the density is the highest. These values are 0.01, 0.008, and 0.005 $R_\oplus$ for the 10^6, $10^{6.5}$, and 10^7 particles simulations respectively.

Once the simulations are finished and no major impacts are still in progress we need to determine the mass and angular momentum direction of both the main post-impact planet and the protolunar disk. The angle between these two vectors is what we define as the misalignment.

4.2.1 Determination of the main planet

In order to determine the mass of the main planet we follow a similar approach to Asphaug et al. (2021). We define a reference density, $\rho = 3053.2$ kg m^{-3}, corresponding to the density of ANEOS forsterite at a temperature of $T = 2000$ K and zero pressure, and determine all particles in the centre of the simulation box with a higher density. These particles determine the main planet and the sum of their masses is the total mass of the object.

We also modified the reference density to 3/4 of its previous value to determine how sensitive our results are to this definition (Asphaug et al., 2021). We found no significant differences in the results between the two reference densities, as we later describe in §4.3. In this study we limit ourselves to examining the direction of the angular momentum vectors. For that reason we consider every particle as a free particle rotating around the centre of mass of the planet and compute the angular momentum vector of the planet as the sum of all particles angular momenta.

4.2.2 Determination of the protolunar disk

The particles not in the post-impact planet can be classified in three groups: particles that escape the system, particles that will fall into the Earth, and particles that will orbit the Earth. This last group of particles forms the protolunar disk that will eventually create the Moon through accretion, and potentially also includes material on wider orbits far outside the disk that will not be relevant for satellite formation.

Having the velocity of the orbiting particles and the mass of the main object (§4.2.1), we compute the total energy and find particles belonging to the first group. This group should include a small subset of bound particles that will eventually leave the Hill sphere, but we will not make this distinction. For the second and third groups we use Reufer et al. (2012)'s approach. We compute the periapsis of each particle via the vis-viva equation,

$$v^2 = GM\left(\frac{2}{r} - \frac{1}{a}\right), \tag{4.2.1}$$

and the orbital eccentricity,

$$e = \sqrt{1 + \frac{2\epsilon h^2}{\mu^2}}, \tag{4.2.2}$$

where ϵ is the specific orbital energy (total energy divided by the reduced mass), h is the specific relative angular momentum (angular momentum divided by the reduced mass), and $\mu \approx GM$ is the standard gravitational parameter. Using the formulae above we can compute the periapsis, $r_p = a(1-e)$, and determine whether a particle will eventually intersect the surface of the Earth or not, using the 99^{th} percentile of all particles' radii from the main planet from the definition in §4.2.1. Particles with a sufficiently high periapsis will be labeled as protolunar disk particles and the total mass and angular momentum is simply computed as the sum of those same values for all particles.

4.3 Results

The rotational configuration of the main planet is complex. If we divide a planet in spherical shells at different radii, we say it is in a coherently rotating state if each shell is spinning around the same axis, which is the axis of the total angular momentum of the planet. Changes in the rotational angle as a function of distance are present as shown in Figure 4.1 for the two fast spinning simulations. In this figure a coherently rotating state would look like a horizontal line at an angle equal to zero, whereas a non-coherently rotating state would look like a curve that has

some non-zero value at the center of the planet and typically slowly approaches zero at the surface. This occurs since most of the mass of the planet is in the outer shells, hence they mostly define the total angular momentum vector of the planet. We can observe the main planets reach a coherently rotational state by the end of their simulations, which use a resolution parameter of $\eta = 1.2348$ and cubic spline kernel (equivalent to 48 neighbour particles). However this evolution is a numerical artifact. For simulations with $\eta = 2.2$, and the Wendland (1995) C6 kernel (equivalent to 655 neighbour particles), the planet does not reach a coherently rotating state, as shown in Figure 4.2. In this case, the planet's rotation state stays very similar throughout both simulations from 25 to 100 ks. We conclude that the timescale necessary for obtaining a coherently rotating planet depends on numerical issues in the simulation and cannot be determined analytically. We expect to reach a coherent rotation state eventually, at least in the real world, due to viscosity.

The evolution of the total angular momentum of the planet is not affected by these different interior behaviours. We observe similar values for the total angular momentum of the planet for both types of simulations, and their value over time is almost constant. A small increase of the order of a few percent is observed due to the addition of surrounding material into the main planet as the simulation evolves from 25 to 100 ks. This result suggests that the angle between the total angular momentum of the main planet and the protolunar disk is a numerically reliable quantity.

We find that it is possible to create a debris disk that is significantly misaligned with the spin of the post-impact Earth, as shown in Figure 4.3 for the $L_{\rm pE} \propto \hat{x}$ simulations and in Figure 4.4 for the $L_{\rm pE} \propto \hat{y}$ simulations. Simulations with $L_{\rm pE} \propto \hat{y}$ tend to be more chaotic than $L_{\rm pE} \propto \hat{x}$ simulations. We find non-aligned clumps with respect to the protolunar disk in these simulations as shown in Figure 4.4, a feature not present in $L_{\rm pE} \propto \hat{x}$ simulations. The misaligned angle of the protolunar disk with respect to the spin of the post-impact Earth is slightly higher by an extra $\sim 5^\circ$ if the spin angular momentum of the pre-impact Earth is proportional to $\pm\hat{y}$, rather than $\pm\hat{x}$. We speculate this is because if Theia ejects mainly low-velocity material near the Earth's pole (as in the $\hat{y}$ case), the change in angular momentum of the Earth would be smaller than the $\hat{x}$ spin case, where Theia would eject a large amount of high velocity material such that the Earth preserves less of its pre-impact rotation.

The angular momenta found for the protolunar disks are roughly one order of magnitude smaller than the angular momentum of the post-impact Earth. Moreover, the protolunar disk's angular momentum is roughly in the same direction as the initial orbital angular momentum of Theia (i.e. $\propto \hat{z}$). In addition, due to the small

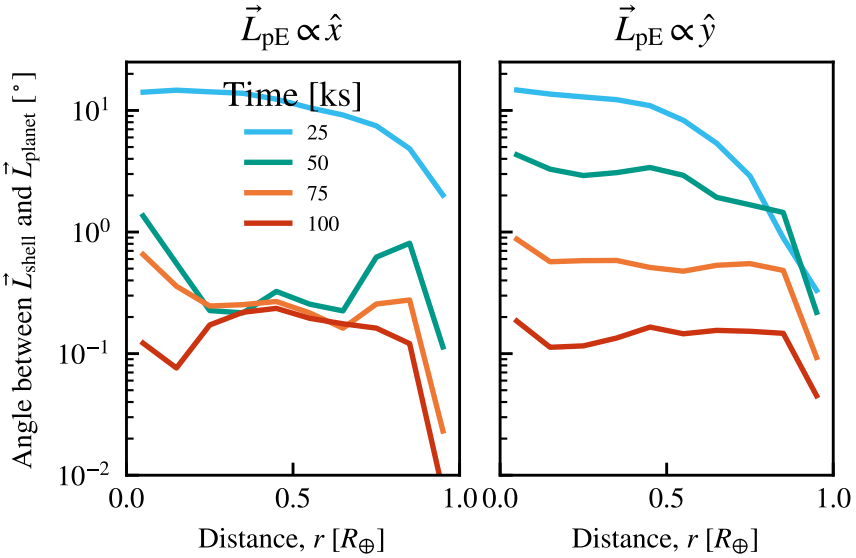

Figure 4.1: Angle between the total angular momentum of the planet and particles grouped by spherical shells at different simulation times for the high spinning proto-Earth scenarios ($L_{\rm pE} = L_{\rm EM}$). Artificial viscosity turns the irregularly rotating planet into an almost differential or solid rotating object, where the rotational angle as a function of distance is constant.

impact velocity considered, only a small number of particles escape the simulation box. A simple model for the resulting misalignment can be made by assuming that the angular momentum of the protolunar disk is very small compared with the spin angular momentum of the planet, and its direction is equal to the direction of the orbital angular momentum of Theia. This is shown graphically in Figure 4.5, where these assumptions are seen to be generally quite good. The largest exception is $L_{\rm pE} = 0.5\ L_{\rm EM}\ \hat{y}$ (second row, second column), where the protolunar disk has an angular momentum that is almost half that of the final planet's in magnitude.

Let $\vec{L}_{\rm orbit}$ be the orbital angular momentum of Theia (1.25 $L_{\rm EM}$ in magnitude in our simulations) and $\vec{L}_{\rm pE}$ the spin angular momentum of the proto-Earth. Assuming these two vectors are orthogonal and the angular momentum of the protolunar disk is 0, the misalignment angle, α, would be similar to

$$\alpha \sim \frac{\pi}{2} - \arctan \frac{L_{\rm orbit}}{L_{\rm pE}}. \tag{4.3.1}$$

This is of course a first order approximation because the angular momentum of the protolunar disk is never equal to zero and is not necessarily in the same direction as the orbital angular momentum of Theia, as shown in Figure 4.5. This analytical prediction, compared with the simulation values, is shown in Figure 4.6.

The misalignment angles found are roughly independent ($< 1°$ on average) of the

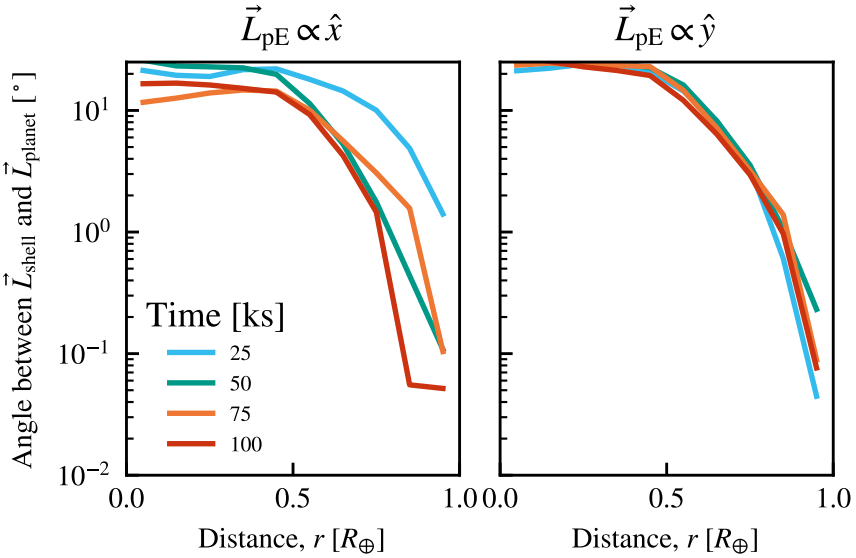

Figure 4.2: Angle between the total angular momentum of the planet and particles grouped by spherical shells at different simulation times for the high spinning proto-Earth scenarios ($L_{\rm pE} = L_{\rm EM}$). This figure is equivalent to Figure 4.1 but for simulations using the Wendland (1995) C6 kernel instead of cubic spline. In this case very little evolution is present in the rotational configuration of the main planet after the impact.

two definitions of reference density described in §4.2.1, as shown in Figure 4.6. Moreover, we run the same simulations with 10^6, $10^{6.5}$, and 10^7 particles to study the convergence of these results. We found that simulations with $L_{\rm pE} \propto \hat{x}$ have a slightly better convergence rate than $L_{\rm pE} \propto \hat{y}$, as seen in Figure 4.7. The more chaotic nature of the $L_{\rm pE} \propto \hat{y}$ simulations together with the misaligned clumps could explain this result, as previously mentioned.

In addition to focusing on the inclination of the post-impact disk, we also investigate the disk's total mass as shown in Figure 4.8. We observe orbiting clumps in stable orbits, as in chapter 2, for most of our simulations with a wide range of different masses, the highest one being the case without pre-impact spin. The total mass of the debris disk is overall higher for the non-spinning case and the $L_{\rm pE} \propto \hat{x}$ simulations, with values between 2.25% and 2.75% $M_\oplus$. For the $L_{\rm pE} \propto \hat{y}$ simulations we get a more dispersed range of values between 1.2% and 2.5% $M_\oplus$. Ida et al. (1997) and Salmon & Canup (2012) showed that producing an object the size of the Moon requires a protolunar disk containing at least 2 Moon masses (or 2%$M_\oplus$), however the presence of clumps in the disk could lower this number significantly.

Large decreases in the mass of the protolunar disk, as seen in the left panel of Figure 4.8, and some simulations in the right panel, are caused by a clump coming inside the Roche radius and being tidally disrupted by the main planet. During

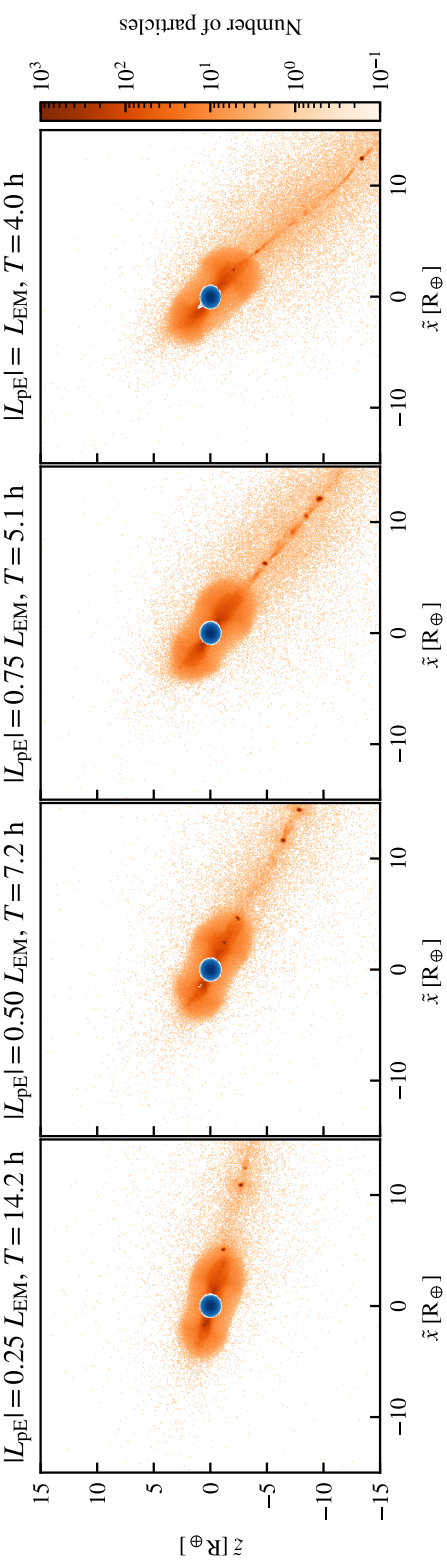

Figure 4.3: Misalignment angle between the post-impact Earth's spin and the protolunar disk for the $L_{pE} \propto \hat{x}$ simulations. This new set of coordinates is defined such that Earth's spin is proportional to $\tilde{z}$, and the $\tilde{y}$ component of the protolunar disk angular momentum is 0, effectively looking at the protolunar disk from its side. Blue represents the post-impact Earth.

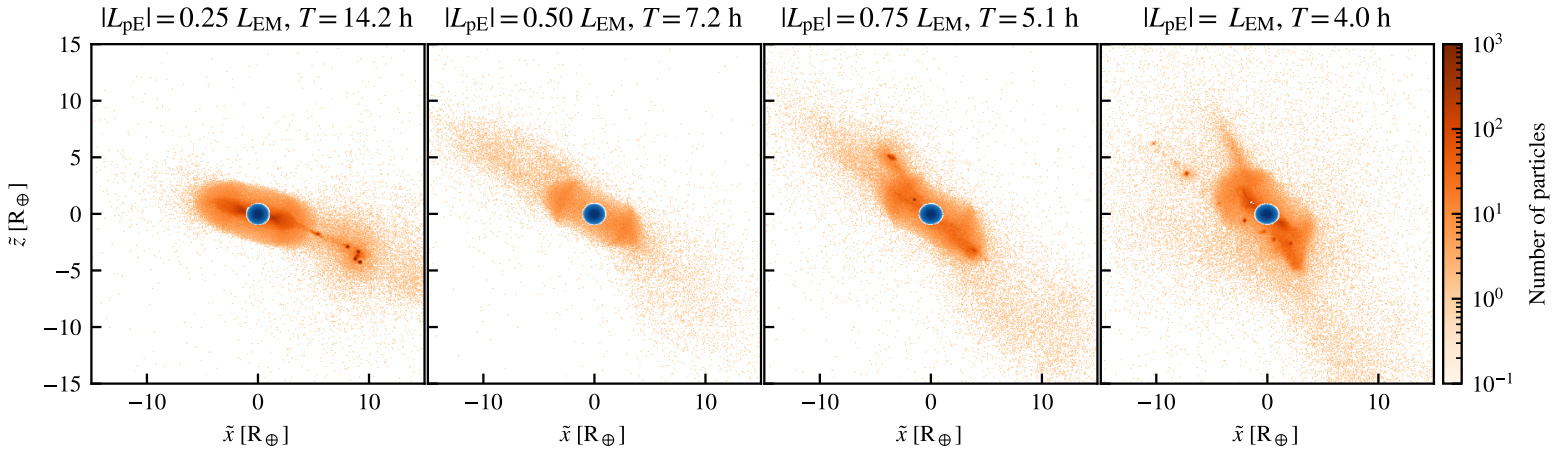

Figure 4.4: Misalignment angle between the post-impact Earth's spin and the protolunar disk for the $L_{pE} \propto \hat{y}$ simulations. Coordinates are defined as in Figure 4.3.

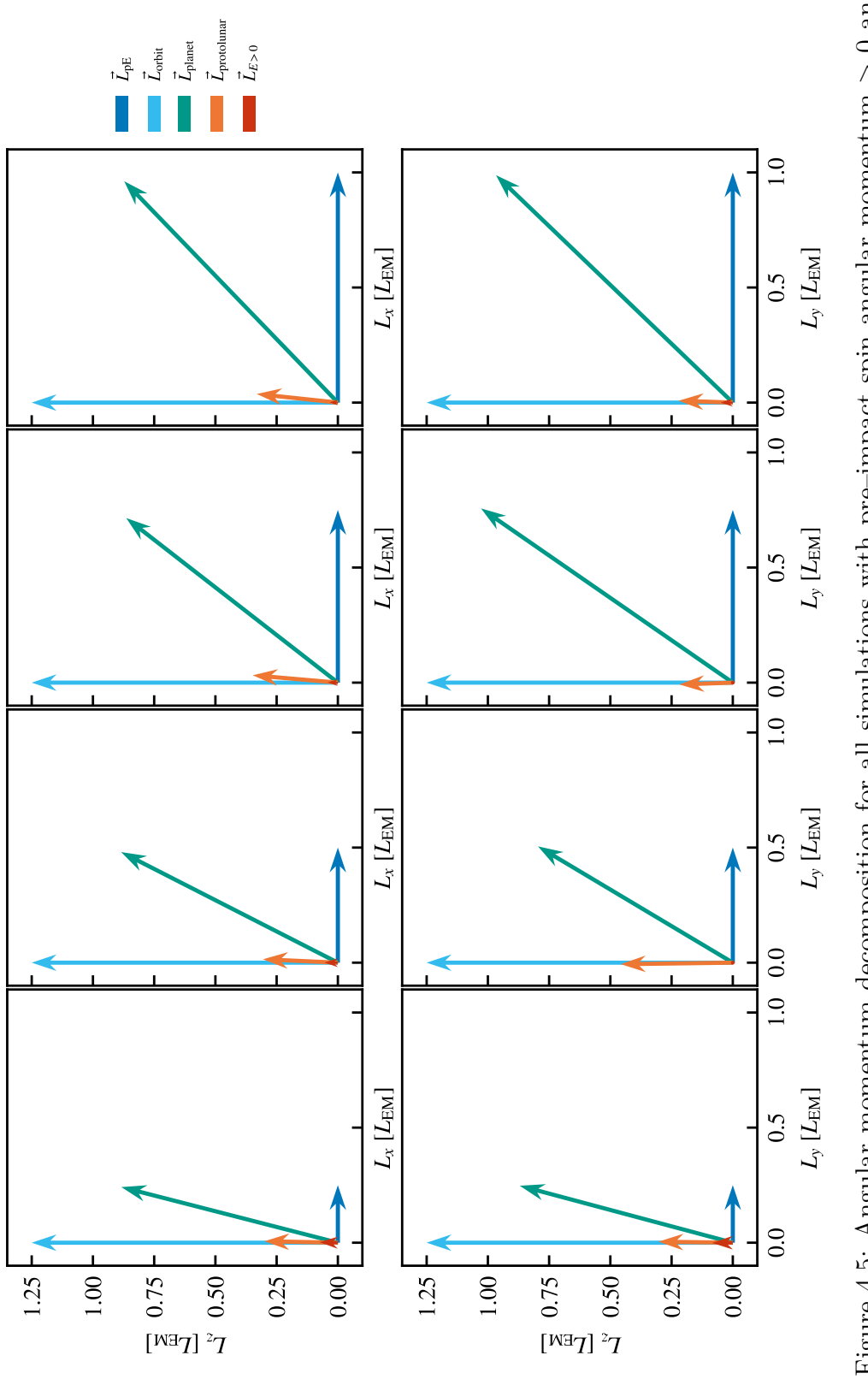

Figure 4.5: Angular momentum decomposition for all simulations with pre–impact spin angular momentum > 0 and 10^7 particles. Top and bottom rows represent simulations with $L_{\rm pE} \propto \hat{x}$ and $L_{\rm pE} \propto \hat{y}$ respectively. Columns represent different pre–impact spinning rates, from low to high, and colours represent different angular momentum vectors. $\vec{L}_{pE}$ and $\vec{L}_{\rm orbit}$ represent the angular momentum vectors present before impact, and $L_{\rm planet}$, $L_{\rm protolunar}$, and $L_{E>0}$ represent the planet's, protolunar disk's, and escaping particles' angular momenta by the end of the simulations. Note $L_{E>0}$ is usually too small to be seen at this scale.

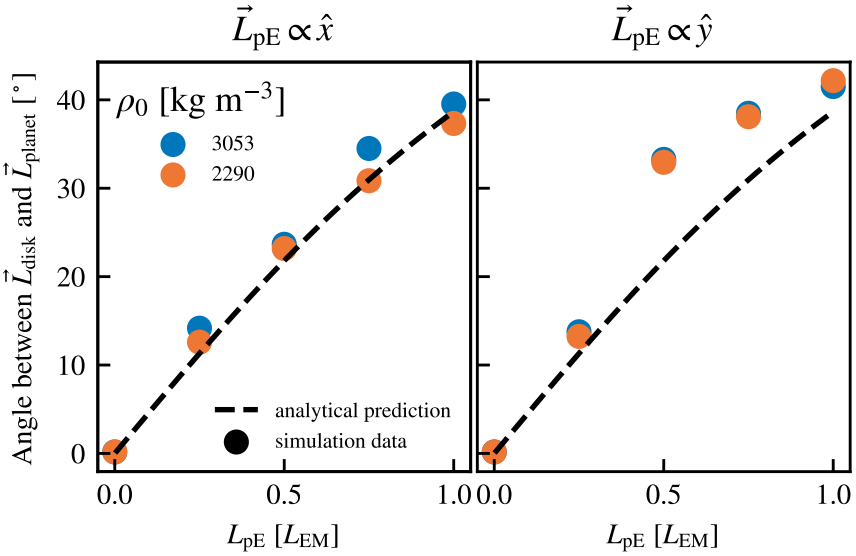

Figure 4.6: Angle between the total angular momentum of the planet and the protolunar disk, as a function of the initial spin angular momentum of the proto-Earth. These are the results for the highest resolution considered, 10^7 particles. The colours represent reference densities used to compute the different angular momenta of the planet and protolunar disk, as described in §4.2.1. The second value is 3/4 of the first one, as done by Asphaug et al. (2021). The dashed line represents the analytical prediction by Equation 4.3.1.

this event some particles initially labeled as protolunar particles are relabeled as unbound particles due to their increase in velocity, diminishing the total mass of the protolunar disk.

Ensuring the misalignment angle is somewhat preserved during a timescale of months is crucial to form an inclined Moon through accretion, although having a clump as a result of the giant impact could effectively hasten the process. We observed the misalignment angle is almost constant throughout the later times in our simulations (from 50 ks up to 100 ks, $\sim$ 1/2 day), as shown in Figure 4.9. This suggests that the misalignment will persist over timescales of at least days.

4.4 Discussion

Our next step would be performing simulations of the protolunar disk to accrete a Moon and determine elements of its early orbit that are actually observable, or at least comparable with long-term evolution studies of the orbit of the Moon.

Tides on the Earth will have an important role determining if the misalignment

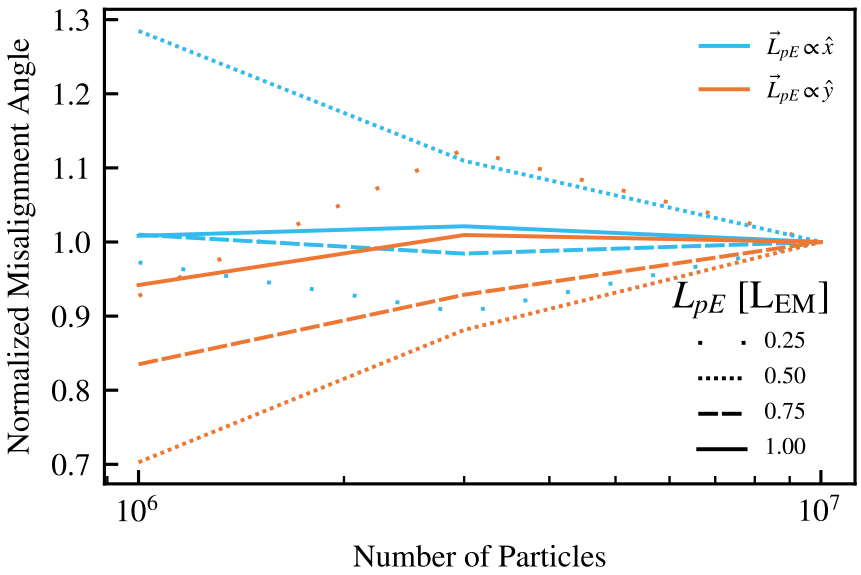

Figure 4.7: Misalignment angle between the post-impact Earth's spin and the protolunar disk at the latest snapshot, for different resolutions (i.e. number of particles). Values are normalized to the 10^7 simulation results.

would survive or not during the accretion of the Moon, especially considering the presence of clumps right at the start of the process and the short distance between the Earth and the early Moon. Neither clumps, nor a misaligned protolunar disk have been considered so far in models for the Moon's accretion (Kokubo et al., 2000; Salmon & Canup, 2012). Misaligned protolunar disks have been considered only with equally tilted planets, however this project opens up the possibility of a tilted Earth with respect to the ecliptic and an inclined Moon with respect to the spin of the Earth. Moreover, tides within the early hot Moon could have a significant role damping the lunar inclination (Ćuk et al., 2016).

Another issue is the total angular momentum. In this study we have restricted ourselves to canonical-like impacts with a spinning proto-Earth, orthogonal to the orbital angular momentum of Theia. The quadratic sum of those two values can easily exceed the present-day value of the angular momentum of the Earth–Moon system. To solve this we need either a mechanism to remove angular momentum, or an impact with a lower initial angular momentum. Since the velocity of impact in this case has been the mutual escape velocity, the natural solution would be to decrease the angle of impact. However, a lower angle impact could potentially yield a lower misalignment angle, since turbulent mixing between the proto-Earth and Theia would be enhanced. On the bright side, low angle impacts yield more proto-Earth material onto the protolunar disk, helping alleviate the isotopic crisis (Reufer et al., 2012).

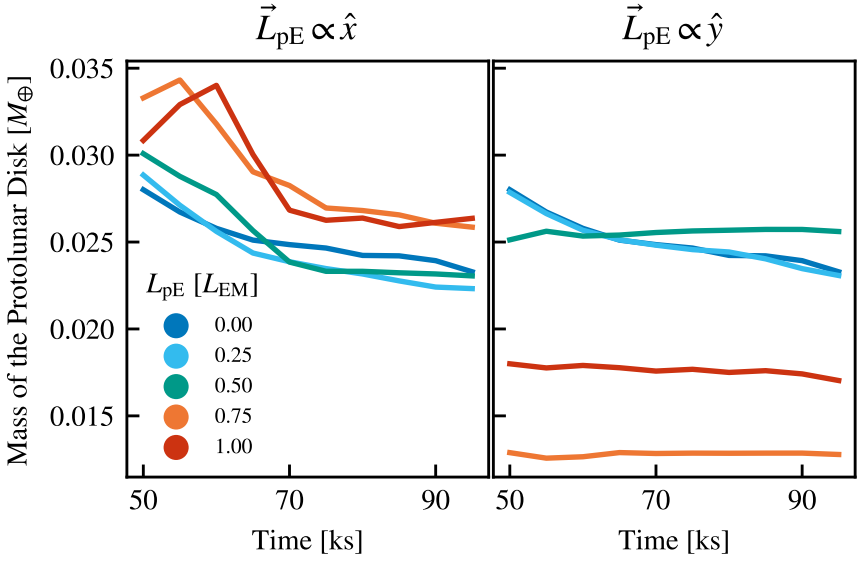

Figure 4.8: Mass of the protolunar disk for the 10^7 particle simulations as a function of time. The masses have been computed using §4.2.2.

Finally, the parameter space considered in this study is relatively small but completely new in the literature. We have limited ourselves to one type of giant impact model, and two values of the direction of the proto-Earth's spin angular momentum with respect to the orbital angular momentum of Theia. The addition of spin in giant impact simulations counts for 6 new parameters if both proto-planets are spinning, or at least 3 like in this study.

4.5 Conclusions

We explore how a post-impact misalignment between the Earth's spin and the protolunar disk can be formed in giant impacts. We found having a misalignment angle is possible even when the proto-Earth has a relatively slow initial spin, with a period of 14 hours, that is orthogonal to Theia's orbital angular momentum. Moreover, the misalignment angle is proportional to the initial spinning rate and it is slightly higher when Theia comes from the equatorial plane of the proto-Earth and ejects mainly North/South pole material, rather than Theia coming from the North/South pole direction and ejecting spinning material near the equator. The highest value found, for a proto-Earth spinning with the angular momentum of the Earth–Moon system today, is 41°. We observe the misalignment being persistent during the later times in our simulations ($\sim 1/2$ day), being a first step to accrete a Moon from an inclined debris disk. The mass of the protolunar disk is sufficient to accrete a Moon, and the results are converging for most of our simulations. Future

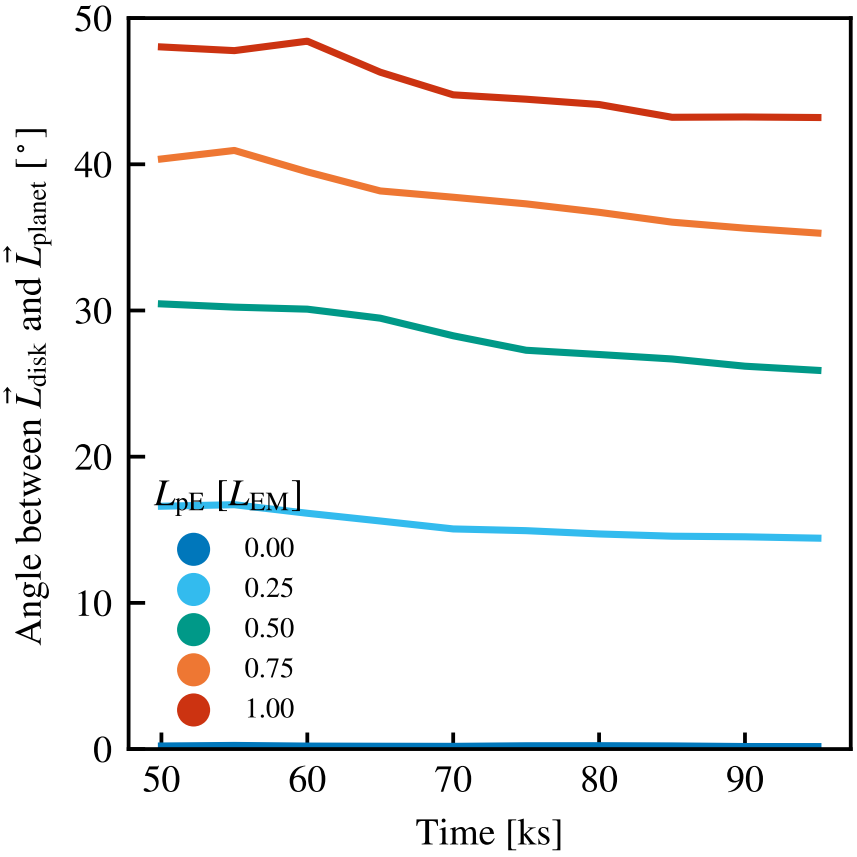

Figure 4.9: Misalignment angle between the post-impact Earth's spin and the protolunar disk as a function of time for the $L_{\rm pE} \propto \hat{x}$ simulations. Similar results are found for $L_{\rm pE} \propto \hat{y}$ simulations.

studies of a wider parameter space could establish how the misalignment angle depends on the impact velocity, angle of impact, and the magnitude and direction of the initial spin of the proto-Earth.

Chapter 5

Conclusions

The solar system used to be a much more violent place. Giant impacts between proto-planets were a common feature during the latest stages of planet formation. Their importance has been appreciated for several years since they dictate many of the features we still see today in our neighbouring planets and in our own.

In this thesis, I have tackled both some questions about the formation of the Moon, and improvements in the methodologies used for giant impact studies. The former focused on the canonical model for the formation of the Moon and on the importance of pre-impact spin in giant impact outcomes, a topic little explored in the literature. The latter addressed a problem in smoothed particle hydrodynamics (SPH) simulations for giant impacts: the absence or impossibility of having density discontinuities in the simulation. Since planets should have density discontinuities, this creates a systematic error in the simulations that has been barely tackled in the past.

After an introduction in Chapter 1, Chapter 2 first focused on developing a method to solve the hydrostatic equilibrium equation for a spinning planet, given an arbitrary equation of state, and later placing particles such that a spinning planet could be represented in a SPH simulation. These methods have been implemented and made open-source in python under the name WoMa (World Maker), publicly available at `https://github.com/srbonilla/WoMa`. With this new tool under our belt, making initial conditions for giant impact studies with pre-impact spinning planets was effortless.

The second goal of Chapter 2 was to study the potential importance of pre-impact spin in giant impact simulations. For that purpose, I set up canonical-like simulations where the impactor, Theia, had different spin rates. These differences in the pre-impact Theia's spin represent changes (up or down) of only $\sim 10\%$ in the total angular momentum of the system. We found different kinds of impact outcomes depending on these small changes: counter-rotating Theia produced quick mergers, whereas a rapidly corotating Theia led to a hit-and-run collision with numerous

unbound clumps escaping from the Earth. In the zero spin and slowly corotating Theia cases, a large clump was left orbiting the Earth after 100 hours.

These clumps have a mass similar to the Moon, with an iron content $\sim 1\%$ in mass, and periapsis higher than the Roche limit. To determine whether these clumps have stable orbits, i.e. orbits whose periapsis is larger than the Roche radius, we also need to consider the interaction with the Sun, with the debris disk, and tidal evolution. While its overall fraction of proto-Earth material is 30%, similar to what has been found in previous studies, a radial gradient in material provenance means that $\sim 50\%$ of the surface material originates in the proto-Earth.

The gradient in composition could slightly alleviate the isotopic crisis for the formation of the Moon, assuming that there was only partial mixing of the Moon's mantle in later evolution. It also agrees with recent data hinting that the isotopic composition of the Moon varies with depth, and more Theia-like material is present deeper in the mantle. However, a provenance of $\sim 50\%$ from the proto-Earth at the surface is still not sufficient to solve the isotopic crisis if Theia had a similar isotopic composition to Mars. Overall, we found new structure in the post-impact debris disk of some giant impacts that should be considered in models for the accretion of the Moon and its subsequent evolution.

In Chapter 3 I switched my attention to the method used for simulations of giant impacts, smoothed particle hydrodynamics. The very fundamental idea behind this widely used method is how to reconstruct a density field from a discrete set of particles. This density is by definition smooth, which raises issues for giant impact simulations.

When representing a planet using SPH it is desirable to have density discontinuities at the interface between materials (e.g. core–mantle or mantle–atmosphere boundaries), and at the surface of the planet. These density discontinuities achieve pressure continuity between different material layers in the planets, and their absence provokes a discontinuity in the pressure profile of the planet. This effectively creates an artificial force that repels particles from different materials in the different layers, suppresses mixing between particles, and introduces an unknown systematic error in the simulations. Previous to this work, Woolfson (2007) and Reinhardt et al. (2020) had proposed a fix to this problem, which failed for sophisticated equations of state like ANEOS.

We addressed this problem by defining a simple statistic, which measures how far or close a particle is from a density discontinuity, by looking at the distribution of the neighbouring particles. Then, using this same statistic, and the kernel average pressure, we compute the corrected density. This method improves performance in

the 2D square test with a better maintained shape, and enhanced mixing between different material particles in the 2D Kelvin–Helmholtz test. Giant impact simulations, where the core of the target has been highly disrupted by the impactor, reveal a partially diffused iron core and a higher mass of iron in the debris disk. These two features are not present in standard SPH for this type of impact. Future studies could explore whether there are other scenarios that may yield different results with or without a solution to the density discontinuity problem.

Finally, in Chapter 4, I put my focus back on canonical-like impacts with pre-impact spin. However, on this occasion for a different reason: to explore a mechanism to explain the present-day value of the lunar inclination.

Long-term evolution models for the orbit of the Moon suggest the angle between the Earth's spin and the normal of the lunar orbital plane was $\sim 10^{\circ}$ at the time the Moon accreted. This value cannot be explained using traditional giant impact models that produce a debris disk in the equatorial plane of the Earth without an extra mechanism like a gravitational resonance between the post-impact Earth and the debris disk.

In this chapter we explored how a misalignment between the Earth's spin and the protolunar disk can be formed in giant impacts. For that purpose we perform canonical-like simulations with a spinning proto-Earth. We found having a misalignment angle is possible even when the proto-Earth has a slow initial spin, with a period of 14 hours, that is orthogonal to Theia's orbital angular momentum. The misalignment is proportional to the spinning angular momentum of the proto-Earth. Moreover, this misalignment is persistent over timescales of days, and could be a first step towards accreting a Moon from an inclined protolunar disk.

The origin of the lunar inclination is unclear and many authors have proposed solutions, which all rely on a dynamical process after the accretion of the Moon from an equatorial debris disk. In this work we found a new possibility, the presence of pre-impact spin can yield an inclined protolunar disk from which the Moon could be accreted. Subsequent models need to be performed to determine to what extent the inclination could persist over the timescales necessary for the accretion of the Moon. During this subsequent evolution, the role of tides within the hot Moon and proto-Earth will probably have an important role in partially or totally damping the inclination.

With all the tools developed in this thesis, exploring a wider and richer parameter space of giant impacts or protolunar disks is now possible. These methods could help answer many questions about the formation of the Moon and many others about our solar system.

Bibliography

ALMA Partnership et al., 2015, Astrophys. J. Lett., 808, L3

Adachi I., Hayashi C., Nakazawa K., 1976, Progress of Theoretical Physics, 56, 1756

Agnor C. B., Canup R. M., Levison H. F., 1999, Icarus, 142, 219

Andrews-Hanna J. C., Zuber M. T., Banerdt W. B., 2008, Nature, 453, 1212

Asphaug E., 2014, Annual Review of Earth and Planetary Sciences, 42, 551

Asphaug E., Emsenhuber A., Cambioni S., Gabriel T. S. J., Schwartz S. R., 2021, , 2, 200

Balsara D. S., 1995, Journal of Computational Physics, 121, 357

Barnes J. J., Tartèse R., Anand M., McCubbin F. M., Neal C. R., Franchi I. A., 2016, Earth and Planetary Science Letters, 447, 84

Barr A. C., 2016, Nature, 540, 42

Benz W., Slattery W. L., Cameron A. G. W., 1986, Icarus, 66, 515

Benz W., Slattery W. L., Cameron A. G. W., 1987, Icarus, 71, 30

Benz W., Slattery W. L., Cameron A. G. W., 1988, Icarus, 74, 516

Binney J., Tremaine S., 1987, Galactic dynamics

Borrow J., Bower R. G., Draper P. W., Gonnet P., Schaller M., 2018, CoRR, abs/1807.01341

Boss A. P., Morfill G. E., Tscharnuter W. M., 1989, in Atreya S. K., Pollack J. B., Matthews M. S., eds, , Origin and Evolution of Planetary and Satellite Atmospheres. pp 35–77

Bottke W. F., Walker R. J., Day J. M. D., Nesvorny D., Elkins-Tanton L., 2010, Science, 330, 1527

Cameron A. G. W., 1997, Icarus, 126, 126

Cameron A. G. W., Ward W. R., 1976, in Lunar and Planetary Science Conference. p. 120

Cano E. J., Sharp Z. D., Shearer C. K., 2020, Nature Geoscience, 13, 270

Canup R. M., 2004, Icarus, 168, 433

Canup R. M., 2005, Science, 307, 546

Canup R., 2008, Icarus, 196, 518

Canup R. M., 2012, Science, 338, 1052

Canup R. M., Asphaug E., 2001, Nature, 412, 708

Canup R. M., Esposito L. W., 1996, Icarus, 119, 427

Canup R., Barr A. C., Crawford D. A., 2013, Icarus, 222, 200

Canup R. M., Visscher C., Salmon J., Fegley Bruce J., 2015, Nature Geoscience, 8, 918

Canup R. M., et al., 2021, arXiv e-prints, p. arXiv:2103.02045

Chambers J. E., 2001, Icarus, 152, 205

Chambers J. E., Wetherill G. W., 1998, Icarus, 136, 304

Chau A., Reinhardt C., Helled R., Stadel J., 2018, Astrophys. J., 865, 35

Chen Y., Zhang Y., Liu Y., Guan Y., Eiler J., Stolper E. M., 2015, Earth and Planetary Science Letters, 427, 37

Citron R. I., Genda H., Ida S., 2015, Icarus, 252, 334

Clayton R. N., Mayeda T. K., 1975, Lunar and Planetary Science Conference Proceedings, 2, 1761

Clement M. S., Kaib N. A., Raymond S. N., Chambers J. E., Walsh K. J., 2019, Icarus, 321, 778

Courant R., Friedrichs K., Lewy H., 1967, IBM Journal of Research and Development, 11, 215

Craddock R. A., 2011, Icarus, 211, 1150

Ćuk M., Stewart S. T., 2012, Science, 338, 1047

Ćuk M., Hamilton D. P., J. L. S., T. S. S., 2016, Nature, 539, 402

Cullen L., Dehnen W., 2010, Mon. Not. R. Astron. Soc., 408, 669

Dauphas N., 2017, Nature, 541, 521

Dauphas N., Schauble E. A., 2016, Annual Review of Earth and Planetary Sciences, 44, 709

Dauphas N., Chen J. H., Papanastassiou D. A., 2015, in 46th Annual Lunar and Planetary Science Conference. Lunar and Planetary Science Conference. p. 2436

Day J., Moynier F., 2014, PTRSA, 372, 20130259

Dehnen W., Aly H., 2012, Mon. Not. R. Astron. Soc., 425, 1068

Deng H., Reinhardt C., Benitez F., Mayer L., Stadel J., Barr A. C., 2019a, Astrophys. J., 870, 127

Deng H., Ballmer M. D., Reinhardt C., Meier M. M. M., Mayer L., Stadel J., Benitez F., 2019b, Astrophys. J., 887, 211

Desch S. J., Taylor G. J., 2011, in 42nd Annual Lunar and Planetary Science Conference. Lunar and Planetary Science Conference. p. 2005

Dhaliwal J. K., Day J. M. D., Moynier F., 2018, Icarus, 300, 249

Elkins-Tanton L. T., Grove T. L., 2011, Earth and Planetary Science Letters, 307, 173

Franchi I. A., Wright I. P., Sexton A. S., Pillinger C. T., 1999, , 34, 657

Gabriel T. S. J., Jackson A. P., Asphaug E., Reufer A., Jutzi M., Benz W., 2020, Astrophys. J., 892, 40

Genda H., Abe Y., 2003, Icarus, 164, 149

Genda H., Fujita T., Kobayashi H., Tanaka H., Abe Y., 2015, Icarus, 262, 58

Gingold R. A., Monaghan J. J., 1977, Mon. Not. R. Astron. Soc., 181, 375

Goldreich P., 1966, Reviews of Geophysics and Space Physics, 4, 411

Goldreich P., Ward W. R., 1973, Astrophys. J., 183, 1051

Gonnet P., 2015, SIAM J Sci. Comput., 37, C95

Greenberg R. R., Zoller W. H., Gordon G. E., 1978, Environmental Science and Technology, 12, 566

Greenwood J. P., Itoh S., Sakamoto N., Warren P., Taylor L., Yurimoto H., 2011, Nature Geoscience, 4, 79

Greenwood R. C., Barrat J.-A., Miller M. F., Anand M., Dauphas N., Franchi I. A., Sillard P., Starkey N. A., 2018, Science Advances, 4

Grossman J. N., Rubin A. E., MacPherson G. J., 1988, Earth and Planetary Science Letters, 91, 33

Guillot T., et al., 2018, Nature, 555, 227

Hallis L. J., Anand M., Greenwood R. C., Miller M. F., Franchi I. A., Russell S. S., 2010, Geochem. Cosmo. Acta, 74, 6885

Harlow F. H., Welch J. E., 1965, Physics of Fluids, 8, 2182

Hartmann W. K., Davis D. R., Chapman C. R., Soter S., Greenberg R., 1975, Icarus, 25, 588

Hauri E. H., Weinreich T., Saal A. E., Rutherford M. C., Van Orman J. A., 2011, Science, 333, 213

Hauri E., Saal A. E., Rutherford M. J., Van Orman J. A., 2015, EPSL, 409, 252

Hayashi C., Nakazawa K., Adachi I., 1977, , 29, 163

Herwartz D., Pack A., Friedrichs B., Bischoff A., 2014, Science, 344, 1146

Hockney R. W., Eastwood J. W., 1981, Computer Simulation Using Particles

Hornung P., Pellat R., Barge P., 1985, Icarus, 64, 295

Hosono N., Saitoh T. R., Makino J., 2016, Astrophys. J. Supp., 224, 32

Hosono N., Iwasawa M., Tanikawa A., Nitadori K., Muranushi T., Makino J., 2017, Publ. Astron. Soc. Jpn., 69, 26

Hosono N., Karato S.-i., Makino J., Saitoh T. R., 2019, Nature Geoscience, 12, 418

Hubbard W. B., 2012, Astrophys. J. Lett., 756, L15

Hubbard W. B., 2013, Astrophys. J., 768, 43

Ida S., Makino J., 1993, Icarus, 106, 210

Ida S., Canup R. M., Stewart G. R., 1997, Nature, 389, 353

Iess L., et al., 2018, Nature, 555, 220

Iess L., et al., 2019, Science, 364, aat2965

Imaeda Y., Inutsuka S.-i., 2002, Astrophys. J., 569, 501

Kaula W. M., Yoder C. F., 1976, in Lunar and Planetary Science Conference. p. 440

Kegerreis J. A., et al., 2018, Astrophys. J., 861, 52

Kegerreis J. A., Eke V. R., Gonnet P., Korycansky D. G., Massey R. J., Schaller M.,

Teodoro L. F. A., 2019, Mon. Not. R. Astron. Soc., 487, 5029

Kegerreis J. A., Eke V. R., Massey R. J., Teodoro L. F. A., 2020, arXiv e-prints, p. arXiv:2002.02977

Kegerreis J. A., Ruiz-Bonilla S., Eke V. R., Massey R. J., Sandnes T. D., Teodoro L. F. A., 2022, submitted

Kellogg O. D., 1929, Foundations of Potential Theory. Springer-Verlag Berlin Heidelberg

Kokubo E., Genda H., 2010, Astrophys. J. Lett., 714, L21

Kokubo E., Ida S., 1998, Icarus, 131, 171

Kokubo E., Ida S., 2007, Astrophys. J., 671, 2082

Kokubo E., Ida S., Makino J., 2000, Icarus, 148, 419

Kong D., Zhang K., Schubert G., 2013, Astrophys. J., 764, 67

Lambrechts M., Johansen A., 2012, Astron. Astrophys., 544, A32

Li J., Lai D., Anderson K. R., Pu B., 2020, arXiv e-prints, p. arXiv:2006.10067

Lissauer J. J., 1993, Annu. Rev. Astron. Astrophys., 31, 129

Liu S.-F., Hori Y., Müller S., Zheng X., Helled R., Lin D., Isella A., 2019, Nature, 572, 355

Lock S. J., Stewart S. T., 2017, Journal of Geophysical Research (Planets), 122, 950

Lock S. J., Stewart S. T., Petaev M. I., Leinhardt Z., Mace M. T., Jacobsen S. B., Cuk M., 2018, Journal of Geophysical Research (Planets), 123, 910

Lock S. J., Bermingham K. R., Parai R., Boyet M., 2020, Space Sci. Rev., 216, 109

Lucy L. B., 1977, Astrophys. J., 82, 1013

Lyon S. P., Johnson J. D., 1992, SESAME: The Los Alamos National Laboratory Equation of State Database

Lyubetskaya T., Korenaga J., 2007, Journal of Geophysical Research (Solid Earth), 112, B03211

Mastrobuono-Battisti A., Perets H. B., 2017, preprint, (arXiv:1704.05082)

McCubbin F. M., et al., 2015, American Mineralogist, 100, 1668

McGlaun M., 1991, in Presented at the 2nd International Symposium on Intense Dynamic Loading and its Effects. pp 9–12

McKinnon W. B., 1984, Nature, 311, 355

McKinnon W. B., 1989, Astrophys. J. Lett., 344, L41

McNally C. P., Lyra W., Passy J.-C., 2012, Astrophys. J. Supp., 201, 18

Melosh H. J., 1989, Impact cratering: A geologic process. Oxford monographs on geology and geophysics, Oxford University Press, New York

Melosh H. J., 2007, Meteoritics and Planetary Science, 42, 2079

Melosh H. J., 2014, Philosophical Transactions of the Royal Society of London Series A, 372, 20130168

Miguel Y., Brunini A., 2010, Mon. Not. R. Astron. Soc., 406, 1935

Militzer B., Wahl S., Hubbard W. B., 2019, Astrophys. J., 879, 78

Monaghan J. J., 1992, Annu. Rev. Astron. Astrophys., 30, 543

Monaghan J. J., 2012, Annual Review of Fluid Mechanics, 44, 323

Monaghan J. J., Lattanzio J. C., 1985, Astron. Astrophys., 149, 135

Mougel B., Moynier F., Göpel C., 2018, Earth and Planetary Science Letters, 481, 1

Mukhopadhyay S., 2012, Nature, 486, 101

Nakagawa Y., Nakazawa K., Hayashi C., 1981, Icarus, 45, 517

Nakajima M., Stevenson D. J., 2015, in AGU Fall Meeting Abstracts. pp P13C–02

Newsom H. E., Taylor S. R., 1989, Nature, 338, 29

Ormel C. W., Klahr H. H., 2010, Astron. Astrophys., 520, A43

Pahlevan K., Morbidelli A., 2015, Nature, 527, 492

Pahlevan K., Stevenson D. J., 2007, Earth and Planetary Science Letters, 262, 438

Pahlevan K., Karato S.-i., Fegley B., 2016, Earth and Planetary Science Letters, 445, 104

Price D., 2005, PhD thesis, -

Price D. J., 2008, Journal of Computational Physics, 227, 10040

Price D. J., 2012, Journal of Computational Physics, 231, 759

Raskin C., Owen J. M., 2016, Astrophys. J., 820, 102

Reinhardt C., Stadel J., 2017, Mon. Not. R. Astron. Soc., 467, 4252

Reinhardt C., Chau A., Stadel J., Helled R., 2020, Mon. Not. R. Astron. Soc., 492, 5336

Reufer A., Meier M. M. M., Benz W., Wieler R., 2012, Icarus, 221, 296

Ringwood A. E., 1989, Earth and Planetary Science Letters, 95, 208

Roche E., 1849, Académie des Sciences de Montpellier: Mémoires de la Section des Sciences, 1, 243

Rufu R., Canup R. M., 2020, Journal of Geophysical Research (Planets), 125, e06312

Rufu R., Aharonson O., Perets H. B., 2017, Nature Geoscience, 10, 89

Ruiz-Bonilla S., Eke V. R., Kegerreis J. A., Massey R. J., Teodoro L. F. A., 2021, Mon. Not. R. Astron. Soc., 500, 2861

Ruiz-Bonilla S., Borrow J., Eke V. R., Kegerreis J. A., Massey R. J., Sandnes T. D., Teodoro L. F. A., 2022, Mon. Not. R. Astron. Soc., 512, 4660

Saff E. B., Kuijlaars A. B. J., 1997, The Math. Int., 19, 5

Safronov V. S., 1960, Annales d'Astrophysique, 23, 979

Safronov V. S., Zvjagina E. V., 1969, Icarus, 10, 109

Saitoh T. R., Makino J., 2013, Astrophys. J., 768, 44

Salmon J., Canup R. M., 2012, Astrophys. J., 760, 83

Schaller M., Gonnet P., Chalk A. B. G., Draper P. W., 2016, Proc. of PASC'16, pp 2:1–2:10

Schiller M., Bizzarro M., Fernandes V. A., 2018, Nature, 555, 507

Shoenberg D., Wilson A. J. C., 1946, Nature, 157, 548

Slattery W. L., Benz W., Cameron A. G. W., 1992, Icarus, 99, 167

Spicuzza M. J., Day J. M. D., Taylor L. A., Valley J. W., 2007, Earth and Planetary Science Letters, 253, 254

Springel V., 2005, Mon. Not. R. Astron. Soc., 364, 1105

Springel V., 2010, Annual Review of Astronomy and Astrophysics, 48, 391

Stephens I. W., et al., 2014, Nature, 514, 597

Stewart S., et al., 2020, in American Institute of Physics Conference Series. p. 080003 (arXiv:1910.04687), doi:10.1063/12.0000946

Swope W. C., Andersen H. C., Berens P. H., Wilson K. R., 1982, J. Chem. Phys., 76, 637

Tassoul J.-L., 1978, Theory of rotating stars

Thompson S. L., 1970, doi:10.2172/4125539

Tian Z., Wisdom J., 2020, Proceedings of the National Academy of Science, 117, 15460

Tian Z., Wisdom J., Elkins-Tanton L., 2017, Icarus, 281, 90

Tillotson J. H., 1962, General Atomic Report GA-3216

Timpe M., Veiga M. H., Knabenhans M., Stadel J., Marelli S., 2020, arXiv e-prints, p. arXiv:2001.09542

Touboul M., Puchtel I. S., Walker R. J., 2012, Science, 335, 1065

Touma J., Wisdom J., 1994, Astrophys. J., 108, 1943

Touma J., Wisdom J., 1998, Astrophys. J., 115, 1653

Verlet L., 1967, Physical Review, 159, 98

Viswanathan V., Rambaux N., Fienga A., Laskar J., Gastineau M., 2019, Geophys. Res. Lett., 46, 7295

Wadsley J. W., Keller B. W., Quinn T. R., 2017, Mon. Not. R. Astron. Soc., 471, 2357

Ward W. R., Canup R. M., 2000, Nature, 403, 741

Warren P. H., 1985, Annual Review of Earth and Planetary Sciences, 13, 201

Weidenschilling S. J., 1977, Mon. Not. R. Astron. Soc., 180, 57

Weidenschilling S. J., Cuzzi J. N., 1993, in Levy E. H., Lunine J. I., eds, Protostars and Planets III. p. 1031

Wendland H., 1995, Advances in Computational Mathematics, 4

Wetherill G. W., Stewart G. R., 1989, Icarus, 77, 330

Wiechert U., Halliday A. N., Lee D.-C., Snyder G. A., Taylor L. A., Rumble D., 2001, Science, 294, 345

Wieczorek M. A., 2006, Reviews in Mineralogy and Geochemistry, 60, 221

Wilhelms D. E., Squyres S. W., 1984, Nature, 309, 138

Williams J. P., Cieza L. A., 2011, Annu. Rev. Astron. Astrophys., 49, 67

Wisdom J., Hubbard W. B., 2016, Icarus, 267, 315

Wisdom J., Tian Z., 2015, Icarus, 256, 138

Wissing R., Hobbs D., 2020, Astron. Astrophys., 643, A40

Wood J. A., 1986, in Hartmann W. K., Phillips R. J., Taylor G. J., eds, Origin of the Moon. pp 17–55

Woolfson M. M., 2007, Mon. Not. R. Astron. Soc., 376, 1173

Wyatt B. M., et al., 2018, Journal of Astrophysics and Astronomy, 39, 26

Young E. D., Kohl I. E., Warren P. H., Rubie D. C., Jacobson S. A., Morbidelli A., 2016, Science, 351, 493

Zhang J., Dauphas N., Davis A. M., Leya I., Fedkin A., 2012, Nature Geoscience, 5, 251